DEVELOPMENT OF A RAINFALL-RUNOFF-INUNDATION MODEL AND FLOOD MONITORING SYSTEM BASED ON SATELLITE IMAGERY FOR KALU GANGA BASIN, SRI LANKA

Tina Sultana

208363F

Degree of Master of Science

Department of Civil Engineering

University of Moratuwa
Sri Lanka

February 2022

DEVELOPMENT OF A RAINFALL-RUNOFF-INUNDATION MODEL AND FLOOD MONITORING SYSTEM BASED ON SATELLITE IMAGERY FOR KALU GANGA BASIN, SRI LANKA

Tina Sultana

208363F

Supervised by

Prof. R. L. H. L. Rajapakse

Thesis submitted in partial fulfillment of the requirements for the degree
Master of Science in Civil Engineering

UNESCO Madanjeet Singh Centre for
South Asia Water Management (UMCSAWM)
Department of Civil Engineering

University of Moratuwa
Sri Lanka

February 2022

DECLARATION OF THE CANDIDATE AND SUPERVISOR

"I declare that this is my own work and this thesis does not incorporate without acknowledgment any material previously submitted for a Degree or Diploma in any other University or institute of higher learning and to the best of my knowledge and belief it does not contain any material previously published or written by another person except where the acknowledgment is made in the text".

Also, I hereby grant to the University of Moratuwa the non-exclusive right to reproduce and distribute my thesis, in whole or in part in print, electronic or other media. I retain the right to use this content in whole or part in future works (such as articles or books).

UOM Verified Signature

2022-02-03

------- ----------------------------

Tina Sultana

Date

The above candidate has carried out research for the Masters Dissertation under my supervision.

UOM Verified Signature

2022-02-03

- - ----------------------------

Prof. R. L. H. L. Rajapakse

Date

ABSTRACT

Development of a Rainfall-Runoff-Inundation Model and Flood Monitoring System based on Satellite Imagery for Kalu Ganga Basin, Sri Lanka

Floods are getting severe due to climate change and anthropogenic activities which need immediate response to lower the risk and decrease the human and financial losses. Flood inundation mapping for flood risk preparedness using satellite data has been widely used in many recent studies. However, satellite imageries may contain some uncertainties. Therefore, flood inundation maps from satellite data need to be verified with flood inundation maps generated by hydrological models from observed data for accurate estimation of flood risk. Although satellite-generated flood maps are widely used to determine the inundation extent, there are certain challenges to their use such as inaccessibility of imagery due to satellite orbit or cloud cover, which hampers accurate measurement of inundation risk.

In this study, the rainfall-runoff inundation (RRI) model for the Kalu Ganga basin was developed, and its applicability to evaluate the discharge and flood inundation areas was discussed. The RRI model could estimate discharge, water levels, and inundation areas simultaneously based on two-dimensional diffusion wave equations. The results and statistical analysis indicate that the RRI model could efficiently estimate extreme flood events. For model calibration, the R^2 value ranges from 0.72-0.80 and for model validation, the R^2 value ranges from 0.75-0.90, which shows good performance of the model.

The simulated inundation extents were verified and compared with Sentinel 1A SAR (Synthetic Aperture Radar) satellite imagery data for 2016 and 2017 flood events. Sentinel 1A, GRD-IW (Ground Range Detected - Interferometric Wide swath) mode of VV co-polarization, with a spatial resolution of 20 m was acquired and pre-processed using the Sentinel Application Platform (SNAP) software toolbox. The pre-processed images were corrected, and maximum likelihood supervised classification was performed to produce the flood inundation maps of the study area. The actual flooded area from RRI is found to be 291.97 km^2 and that from satellite image is found to be 201.7 km^2 for the 2016 flood event. For the 2017 flood event, the actual flooded area from RRI is found to be 371.14 km^2 and that from satellite image is found to be 297.42 km^2. Hence, the flooded area difference was found to be 35.54 % for 2016 and 22.13 % for 2017 flood events from the total area selected from the model. Most of the floodplains from the RRI model and satellite images were along the main river in the basin, including the city of Ratnapura (upstream), the city of Kalutara (downstream), and the areas in between. These results with an accuracy level of ~25 % - 30 % are deemed to be within an acceptable range for emergency evacuation and rapid flood damage assessment purposes. Future studies should further investigate and validate the flood inundation mapping ability of Sentinel 1A SAR using ground-based reference flood maps or other satellite data. This study reveals that satellite imagery can be one of the most cost-effective ways to capture the flood disaster footprints, identify flood-prone areas, and understand the flooding problem in a better way. This methodology can be effectively used for disaster risk management, where the time factor is very critical.

Keywords: Catchment hydrology, Extreme events, River discharge, SAR, Sentinel 1A

DEDICATION

I would like to dedicate this work to my parents and my brother who always supported me, encouraged, and guided me throughout my life.

ACKNOWLEDGEMENT

I would like to sincerely thank my supervisor, Prof. Lalith Rajapakse, for his help and guidance during the duration of this project. His help and advice were major factors that contributed to the completion of the project.

I would also like to thank Prof. Sohan Wijesekera for imparting his knowledge and his expert guidance during his classes which helped me in planning and execution of my project.

I will be eternally grateful to the late Sri Madanjeet Singh, SAF India chapter, and the UMCSAWM Centre for funding my Masters' level studies. Without their support, I would not have been able to support my MSc thesis.

My special thanks to my mentor, Mr. Wajira Kumarasinghe, and the staff of the Department of Civil Engineering and the University of Moratuwa for all their help during this program, especially during the lockdown due to the Covid pandemic. I would also thank the Irrigation Department and Meteorological Department of Sri Lanka for supplying me with the necessary data for the project and my colleagues for their constant help and support for the execution of the project.

Finally, I would thank my parents and my brother for all their support throughout my life and for their encouragement to pursue higher studies in this field of Water Resource Engineering.

TABLE OF CONTENTS

LIST OF FIGURES

LIST OF TABLES

LIST OF ABBREVIATIONS

AMSR	Advanced Microwave Scanning Radiometer
ALOS	Advanced Land Observing Satellite
APHRODITE	Asian Precipitation Highly Resolved Observational Data Integration Towards Evaluation
ASAR	Advanced Synthetic Aperture Radar
ASTER	Advanced Space-borne Thermal Emission and Reflection
AVHRR	Advanced Very High Resolution Radiometer
AVNIR	Advanced Visible and Near Infrared Radiometer
DEM	Digital Elevation Model
ENVISAT	Environmental Satellite
ESA	European Space Agency
ESRI	Environmental Systems Research Institute
EW	Extra Wide Swath
FBD	Fine Beam Dual
GIS	Geographic Information System
GPCC	Global Precipitation Climatology Centre
GSMaP (RNL)	Global Satellite Mapping of Precipitation Reanalysis Product
GRD	Ground Range Detected
IR	Infra-red Wave

IW	Interferometric Wide Swath
MERIS	Medium Resolution Imaging Spectrometer
MLSWI	Modified Land Surface Water Index
MODIS	Moderate Resolution Imaging Spectro-Radiometer
MSE	Mean Square Error
MSI	Multi Spectral Imaging Mission
NIR	Near Infra-red Wave
NDVI	Normalized Differential Vegetation Index
NDWI	Normalized Differential Water Index
NOAA	National Oceanic and Atmospheric Administration
NSE	Nash Sutcliffe Efficiency
LSWI	Land Surface Water Index
LULC	Land-Use Land Cover
PALSAR	Phased Array Type L-Band Synthetic Aperture Radar
PERSIANN-CDR	Precipitation Estimation from Remotely Sensed Information using Artificial Neural Networks- Climate Data Record
RADARSAT	Radar Satellite
RGB	Red Green Blue
RMSE	Root Mean Square Error
RRI	Rainfall-runoff-inundation
SAR	Synthetic Aperture Radar

SM	Strip-map Mode
SNAP	Sentinel Application Platform
SLC	Single Look Complex
SRTM	Shuttle Radar Topography Mission
SWIR	Short Wave Infra-red
TRMM	Tropical Rainfall Measuring Mission
VH	Vertical Transmit- Horizontal Receive
VV	Vertical Transmit- Vertical Receive
WV	Wave Mode

CHAPTER 1

1 INTRODUCTION

1.1 General:

Floods are worldwide natural disasters due to the linked immense loss of lives and property. The importance of discharge in the hydrological cycle is generally known, and its assessment is fundamental for hydrological applications identified with water resources and flood hazard prevention. The lack of streamflow data along the channels makes it extremely difficult to locate changes in surface water structures. To calculate the flood risk in the affected areas, it is important to evaluate the flooded areas immediately after the disaster (Hanasaki et al., 2014). Hydrological models can accomplish this, but modeling is difficult in countries where data are limited (Anusha & Bharathi, 2019; Jeklin, 2016). The lack of data coupled with the geometry of a deltaic river basin complicates the development of the flood models and the simulation of floodplains in very low terrain areas.

The devastating effects are much worse in developing nations in the regions like Asia and Africa, particularly in their deltaic areas, as active countermeasures are not sufficient. Moreover, due to the fertility of floodplains and temperate climate that prevails near the riverine areas, it is subjected to increasing human population invasions which make the population more vulnerable to frequent floods. Thus, flood-hazard evaluations in those areas are critical.

1.2 Background:

Various mathematical hydrological models, like LISFLOOD-FP, HEC-HMS/ HEC-RAS, and the RRI model, were developed and used to estimate and identify the flood inundation areas. Of these, the Rainfall-Runoff-Inundation (RRI) model has the following advantages: being able to instantaneously estimate flood and river runoff in areas including downstream floodplains and upstream mountainous areas; ability to perform calculations for multiple river basins when the downstream floodplain is likely to be affected by multiple rivers; and free availability, making it more accessible to developing countries (Yoshimoto, 2017).

Active and passive remote sensing data have been used for flood mapping in various studies (Ezzine et al., 2018). The water surfaces may be obtained immediately and reliably with the assistance of water indices like Normalized Differential Water Index (NDWI) from optical remote sensing data. However, optical observations are restricted with the presence of clouds and uncertain weather conditions. Microwave remote sensing turns out to be even more important because, unlike passive systems, it can observe day and night in all weather conditions. Since it can detect the flooded region on a massive scale and is independent of borders without being tormented by illumination and different climate conditions, Satellite Synthetic Aperture Radar (SAR) is considered very effective and useful for flood mapping (Senel, 2020).

Sentinel 1 SAR satellite is operated by the Copernicus Program of the European Space Agency (ESA) which consists of two satellite sensors (Sentinel-1A/B). Each Sentinel-1 satellite has a C-Band SAR sensor operating with 5.405 GHz. They have four operational modes with different extents, polarization, incidence angles, and resolutions: Strip-map (SM), Interferometric Wide Area (IW), Extra Wide (EW), and Wave Mode (WV). For this study, Sentinel 1A data, acquired in the Ground Range Detected- Interferometric Wide (GRD-IW) mode with a spatial resolution of 20 m, will be used. Various methods have been developed to extract water surfaces from SAR images when temporal and spatial resolution data are available. One such approach is backscatter histogram thresholding. This is widely favoured in flood mapping studies due to its short computational time (Liang, 2019).

Kalu Ganga River is the third-longest river in Sri Lanka. Frequent floods occur in the basin due to heavy rainfall, topographical features, and demographic conditions. Except for drinking water supply and small irrigation systems, the Kalu Ganga basin has not major development of water resources. The one distinguished development is in the Kukule River, a tributary, which has an 80 MW hydroelectric power plant is operating (Nandalal, 2009). The area along the Kalu Ganga river has frequent floods due to the high annual rainfall in the Ratnapura region. The riverbed height of Ratnapura is 11.7 m Mean Sea Level and 76.5 km length from Ratnapura to Kalutara. Therefore, the slope of the riverbed is only 0.15 m/km (1/6,700), which is adequate to create higher velocities to discharge floods. Moreover, the bottleneck is present in Ellagawa, from 30 km downstream of Ratnapura town and 47 km upstream from Kalutara town. This narrow gap suppresses water in the Ratnapura area for several days before discharging it into the Kalutara area (Nandalal, 2009).

Therefore, in this study, estimation of the flood events for developing a flood monitoring system and comparative study for the evaluation of inundation area through satellite data and RRI model on the Kalu Ganga basin.

1.3 Problem Identification

From the literature review, it is found that flood is the major disaster occurring in the Kalu Ganga Basin. The highest rainfall recorded between the time period 1883 to 2017 was approximately 3,000 mm, which had caused major floods and landslides in the Ratnapura area (Edirisooriya, 2018). According to Samarasinghe (2010), for the 100-year return period, flood risk analysis was performed and found that high-risk area was about 11 km^2, while 65 km^2 and 33 km^2 were in the moderate and low-risk categories, respectively. Out of the total population, 27 % was affected by floods and landslides and claimed the lives of 72 people between 1978 and 2017, causing damage to 3,023 homes and affecting 216,046 families. During the 2017 flood event, 87 schools were damaged which resulted in 17 student deaths. More than 77 people died during this flood event (Edirisooriya, 2018). Hence, to understand the hydrological response of the catchment to the extreme rainfalls, identification of the inundated areas is necessary. Thus, it is essential to develop a hydrological model in the study area to perform the flood analysis. RRI model is selected for this study as it is freely available, user-friendly for watershed modeling, and can generate river discharges and flooding-inundation depths simultaneously. The model will provide a comprehensive understanding of the watershed behaviour to analyse floods, and take mitigation measures to minimize the risk. On the other hand, flood recovery requires emergency, and rapid response to minimize the damages. Identification of inundated areas by the RRI model, and comparing with the remote sensing data for accurate estimation of flood risk will provide a rapid and economic disaster risk response in the area. Therefore, this study will develop a hydrological model and assess the usage and reliability of satellite data for flood inundation mapping.

1.4 Problem Statement

Floods are among the major disasters occurring in the Kalu Ganga basin, and it mostly affects Ratnapura and Kalutara areas which impose certain environmental and economic impacts. To minimize these adverse impacts, it is important to understand the hydrological response of the watershed to extreme rainfall events. Although satellite imagery gives the possibility of rapid inundation mapping a comparative study of satellite inundation mapping with rainfall-runoff-inundation model is not widely practiced in Sri Lanka. Therefore, this study will address the existing gap by developing a rainfall-runoff-inundation model and comparing the outcomes with satellite imagery in the Kalu Ganga basin.

1.5 Objectives

1.5.1 Main Objective

The main objective of this study is to critically analyze the hydrological response of the watershed to extreme rainfall events and assessment of satellite image reliability for flood inundation mapping for the Kalu Ganga Basin in Sri Lanka.

1.5.2 Specific Objective

The specific objectives of this study are listed below:

i. To investigate the existing flood patterns and understand the site-specific conditions of the study area.

ii. To develop a suitable rainfall-runoff-inundation model and proper identification of the inundation areas in the study area.

iii. To carry out sensitivity analysis and understand the sensitive parameters in the process of flood generation and evaluation of the model.

iv. To compare and verify the inundated areas generated from the model with the satellite-based flood event maps.

v. To assess the reliability of satellite images and to recommend possible improvements for flood inundation mapping in the Kalu Ganga Basin.

1.6 Significance of Research

The following points listed below show the significance of the research:

- Determining the extent of floodplain areas using remote sensing data is feasible and may be useful for river locations where data are scarce.
- Estimation of flood events and flood risk inundated areas is important for proper planning of managing watersheds.
- The flood monitoring system will serve as an early evacuation and preparation for the flood events and will help in managing such disasters.
- The use of remote sensing data will help in rapid response for disaster risk mitigation and help in developing early warning systems and evacuation plans.

CHAPTER 2

2 LITERATURE REVIEW

2.1 General

Since Sri Lanka is in the Indian Ocean between the Bay of Bengal and the Gulf of Mannar, pressure fluctuations in the Bay of Bengal with strong winds lead to unexpected heavy rains. Additionally, Sri Lanka experiences two monsoon and two inter-monsoon rainy periods per year. Due to these factors, lower reaches of the Kalu Ganga are exposed to frequent flooding. The Ministry of Disaster Management and Human Rights (M/DM&HR) of Sri Lanka was founded in February 2006 and it acts according to its purview with the Disaster Management Centre (DMC) as the coordinating body for Disaster Release Management (DRM) in Sri Lanka (Samarasinghe, 2010). Since floods are the most common natural disaster, DMC is focusing on mapping flood hazards as one of its priority tasks.

2.2 Flooding in South Asia and Growing Concerns due to Climate Impacts

Flooding in Sri Lanka and other South Asian countries has always been a grave concern in the region. In 2021 itself, flooding due to heavy rains has killed 10 people and displaced 245,000 others in the country. Although flooding has been an annual event in these areas, in recent years, the intensity of floods has increased tremendously due to climate change. Climate change increases the intensity of extreme rainfall events. This, compounded by anthropogenic activities, has increased the runoff during extreme events, increasing the intensity of flash floods in the country (Ampitiyawatta & Guo, 2010). A recent study has predicted a 10 % increase in high rainfall events due to climate change and a 9 % increase in damage due to the increase in extreme rainfall events (Yoshimoto & Amarnath, 2017).

Additionally, climate change increases the flood risk by increasing the intensity of cyclones. In May 2021, Sri Lanka experienced extreme rainfall and flash floods due to

Cyclone Yaas, which killed four people and affected 42,000 more in the country. According to European Civil Protection and Humanitarian Aid Operation study (ECHO), it was observed that there was an increase in the cyclone intensity from 1960-2000 in the Bay of Bengal, from where cyclone Yaas was originated. An increase in cyclone intensities heightens the intensity of rainfall and the runoff volume, inundating larger areas of the land.

2.3 Flood Monitoring Systems

Frappart et al. (2017) used ENVISAT ASAR Global Monitoring SAR generated images at a 1 km spatial resolution to monitor the spatial and temporal dynamics of floods in the Guayas Basin, South America, between 2005 and 2008. This was achieved through a change detection method which had three steps. The images were first classified to identify open water pixels in the basin. Then, image data from four dry seasons from 2005 to 2008 was used to determine the ability to separate the radar signature of the water bodies from signatures of other classes. Finally, the same irregularities of the backscattering coefficient were calculated during the four monsoon seasons in the study, and differences in the coefficient between wet and dry seasons were detected. External data from the Dartmouth Flood Observatory was used to test different thresholds to identify the flooded areas in the watershed. -2.30 ± 0.05 was appropriate to accurately evaluate the number of inundated pixels and reduce the percentage of false recognition to below 10 %. This threshold was used to estimate maps of monthly inundation during December to May (wet season) from 2004 to 2008.

Matgen et al. (2011) studied the flooding that occurred in July 2007 of the Severn River in the UK and the flooding in February 1997 of the Red River (US) using images generated from ENVISAT ASAR Wide Swath, which had a 75 m resolution for flood monitoring system analysis. The numerical distribution of backscatter values for ‘water’ from the synthetic aperture radar (SAR) flood image was estimated and the radiometric thresholding of the image was performed for extraction of the water bodies’ core; identify all water bodies. Change detection for a non-flood image was applied wherever available to eliminate areas with no major change between the flood and non-flood areas.

Schlaffer et al. (2017) used the change detection approach for mapping floods from the SAR time series. Using ENVISAT ASAR Wide Swath (WS) time series which contained more than 600 images and by using a reliable map of permanent water bodies, the conditional probability density functions (PDFs) for land and open water surfaces were evaluated. Since backscatter which is caused by soil moisture and vegetation dynamics depends on seasons, a pixel-wise harmonic model was used to check for this. The method was implemented for a larger flooding event that occurred along the Severn river in the UK.

Yulianto et al. (2015) studied the flooding event in Karawang in Indonesia during March 2010. A flood inundation map was generated for rapid response to help in disaster mitigation efforts and to environmental damage assessment. ALOS PALSAR (Advanced Land Observing Satellite, Phased Array Type L-band Synthetic Aperture Radar) satellite remote sensing data with two images for pre-flood (March 09, 2010) and post-flood (March 26, 2010) events were used for generating flood inundation events. Flood inundation map and land-use data were employed to identify and assess the environmental damage were assessed by using the flood inundation map and the land-use data, performed using ArcGIS software (developed and maintained by ESRI).

A study by Zielinska et al. (2014) monitored wetlands ecosystems using remote sensing techniques. The study was performed from 2002 to 2010 in the Biebrza Wetlands, Poland. The backscattering coefficients were calculated from ALOS PALSAR FBD images which were considered at a cross-polarization HV on 12 May 2008. The coefficients, along with ground truth studies and the visual analysis method, were used to categorize the major wetland areas. Therefore, the backscattering values were distributed among the six wetlands' vegetation classes, and the areas of each category were differentiated and evaluated. Moreover, the variation in the biophysical variable as Leaf Area Index (LAI) was illustrated applying the PALSAR data.

Table 2-1 represents the literature review summary about the flood monitoring systems conducted by various satellite products all over the world.

Table 2-1 Literature review summary for flood monitoring systems

Sl No.	**Name of Paper**	**Authors Name & Journal Published**	**River/ Place Name**	**Catchment Area**	**River Size**	**Satellite Data used**
1	Monitoring Wetland Ecosystems using ALOS PALSAR (L-Band, HV) Supplemented by Optical Data: A Case Study of Biebrza Wetlands in Northeast Poland	Zielinska et al., (2014), Remote Sensing 2014, 6, 1605-1633	Biebrza River	7,051 km^2	155 km long	1. ALOS PALSAR FBD, HV polarization, 12.5 m resolution; 2. ENVISAT MERIS (full resolution, visible and near-infrared) 300 m at nadir; 3. NOAA AVHRR (thermal infrared) 1,100 m at nadir
2	Detecting areas affected by flood using multi-temporal ALOS PALSAR remotely sensed data in Karawang, West Java, Indonesia	Yulianto et al., (2015), Natural Hazards, Remote Sensing Application Centre, Indonesian National Institute of Aeronautics and Space, Jl. Kalisari No. 8, Pekayon, Pasar Rebo, Jakarta 13710, Indonesia	Karawang Regency (Cibeet and Citaram River)	1,753 m^2	-	ALOS PALSAR remotely sensed data with HH polarization, 30 m resolution
3	Towards an automated SAR-based flood monitoring system: Lessons learned from two case studies	Matgen et al., (2011), Physics and Chemistry of the Earth 36 (2011) 241–252	Severn River	11,420 km^2	354 km long	ENVISAT ASAR Wide Swath image, 75 m resolution
			Red River	116,500 km^2	890 km long	Two RADARSAT-1 SAR, HH-polarized scenes, 12.5 m resolution
4	Monitoring of the Spatio-Temporal Dynamics of the Floods in the Guayas Watershed (Ecuadorian Pacific Coast) Using Global Monitoring ENVISAT ASAR	Frappart et al., (2017), Water ISSN 2073-4441; CODEN: WATEGH	Guayas River	32,300 km^2	60 km long	ENVISAT ASAR Global Monitoring SAR images, 1 km spatial resolution

Sl No.	Name of Paper	Authors Name & Journal Published	River/ Place Name	Catchment Area	River Size	Satellite Data used
	Images and Rainfall Data					
5	Probabilistic mapping of flood-induced backscatter changes in SAR time series	Schlaffer et al. (2017), International Journal of Applied Earth Observation and Geoformation	Severn River	11,420 km^2	354 km long	ENVISAT ASAR, 677 ASAR scenes for the years 2005–2012 Wide Swath (WS) mode and VV polarisation at a spatial resolution of 150 m.

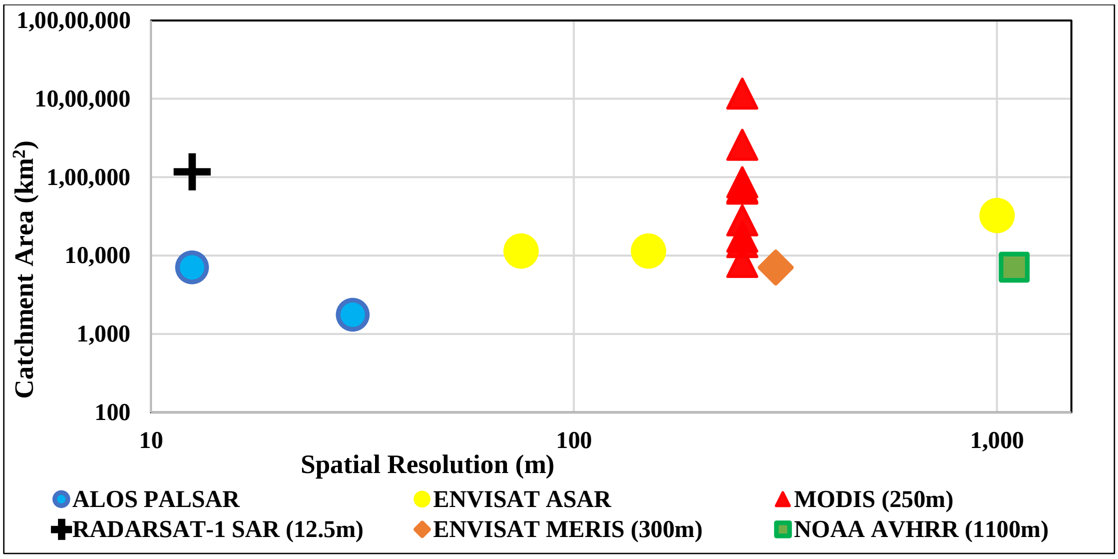

Figure 2-1 Catchment area along with other satellite data spatial resolution

Figure 2-1 represents the basin area along with the spatial resolution of various satellite data which is applied for detecting and in flood monitoring systems. In this graph, most of the basin sizes are above 5,000 km^2 and lower resolution of satellite data can identify the floodplain areas in these basins. For rivers like Kalu Ganga, moderate in size and with an area of 2,839 km^2, satellite data like ALOS PALSAR 12.5 m, 30 m, and RADARSAT-1 SAR of 12.5 m spatial resolution will be appropriate for analysis of floodplain areas in the basin.

2.4 MODIS/ Other Satellite data

Arvind et al. (2016) calculated the flood areas in Krishna and Tungabhadra Rivers in India, using MODIS (MOD09Q1) Terra Surface Reflectance 8-Day L3 Global 250 m resolution for March, September, and November. The method applies was the mean shift algorithm with comparison to artificial neural network methods like self-arranging maps for automated water pixel classification and derivation. The classification of flood and non-flood areas was performed to estimate the algorithmic operation, root mean square error, and receiver operational characteristics were used as performance assessment indices. The results showed valuable information for the analysis of multiple and temporal satellite images, which can be used for present and future investigation in disaster mitigation studies.

Brakenridge (2006) carried out flood detection and characterization in Wabash River, Little Wabash River, and White River, US with the help of MODIS band 2, 250 m resolution surface reflectance satellite data, and ASTER data band 2, 15 m resolution data. The MODIS data was applied in this study for inland flooding along streams and rivers in the Wabash basin. The applications included flood identification and warning, rapid response for mapping of inundation areas, and flood hazard evaluation (by map compilation, over time, of MODIS-observed inundation).

Brakenridge et al. (2007) used Advanced Microwave Scanning Radiometer (AMSR-E) band at 36.5 GHz for the calculation of discharge in the Siret River in Ukraine. The in-situ gauging stations were used for estimating the sensitivity and accuracy of the orbital measurements. Further assessments demonstrated that to detect seasonal variations in rivers, AMSR-E can provide suitable global measurements of daily streamflow data even if only incomplete monthly mean streamflow data are accessible for calibration.

Kwak et al. (2014) detected flood areas in the Indus River, Pakistan using an improved version of MODIS data and indices to generate maps for the spatial and temporal dynamics of floods in near-real-time. The data used are MODIS L3 8-day surface reflectance product (MYD09A1), 500 m resolution, ALOS PALSAAR, PALSAR level 1.5 is a 16-bit unsigned integer and spatial resolution of 12.5 m with 70 km swath (HH polarization) and DEM HydroSHEDS 15 arc-sec resolution. The indices evaluated were NDVI, NDWI, LSWI, and MLSWI. The MLSWI index value was found to be the most efficient at 0.5 for identifying water bodies, such as clear water, murky water, turbid water, or mixed water that occurred due to floods.

Tarpanelli et al. (2013) estimated the river discharge variations in Po River, Italy using MODIS data, 250 m resolution, (MOD02QKM and MYD02QKM) data, channel 1 (0.620–0.670 µm -Red) and channel 2 (0.841–0.876 µm –Near Infrared) data sets, obtained by the Aqua sensor board satellite. The change in variation of land and water from the Near Infrared (NIR) segment of the electromagnetic spectrum is subjugated by calculating the ratio (C/M) of the MODIS Channel 2 reflectance values between two pixels situated within (M) and outside (C), but nearby the river. With the presence of water, the values of C/M increase, and, hence, discharge as well increases. Moreover, an exponential smoothing filter was applied to decrease the noise effects due to atmospheric contribution, thus obtaining C/M∗, whereas M∗ was obtained after applying the filter to enhance the water pixels present in the image. The sensitivity of the results showed a satisfactory (r ~ 0.6) value during the selection of the C and M pixels which was examined by arbitrarily varying their location and the arrangement with in-situ observations of velocity.

Tarpanelli et al. (2017) estimated the river discharge through MODIS data to generate flood inundation maps and flow dynamics in the Upper Tiber River, Italy. For this, the data used was the ratio of the MODIS Channel 2 reflectance values between two pixels situated inside and outside the river. Temporal daily streamflow data between 2006 and 2010 determined at two gauging stations situated along the Upper Tiber River basin were applied to observe the technique. The results showed good agreement with a correlation coefficient value of 0.8 between MODIS data and graphical representation for streamflow with respect to time.

Table 2-2 represents the description of MODIS/ other satellite data used in various studies.

Table 2-2: Literature review summary for MODIS/other satellite data

Sl No.	Authors Name & Journal Published	River Name	Basin Area	River Size	MODIS and other Satellite Data used
1	Arvinda C. S et.al. (2016), Procedia Computer Science 89	Krishna river	258,948 km^2	1,400 km long	MODIS (MOD09Q1) Terra Surface Reflectance 8-Day L3 Global 250 m resolution
		Tungabhadra river	71,417 km^2	531 km long	
2	Brakenridge R. et.al. (2003), Water Resources Research, VOL. 43	Siret River	28,116 km^2	647 km long	Advanced Microwave Scanning Radiometer (AMSR-E) band at 36.5 GHz, descending orbit, HH polarization
3	Brakenridge R. et.al. (2007), Transboundary Floods: Reducing Risks Through Flood Management, Netherlands	Wabash River	86,000 km^2	810 km long	1. MODIS band 2, 250 m resolution Surface reflectance, 2. ASTER band 2, 15 m resolution
		Little Wabash River	8,287 km^2	389 km long	
		White River	14,880 km^2	583 km long	
4	Tarpanelli A. et.al. (2013), Remote Sensing for	Po river	74,000 km^2	652 km long	MODIS 250 m resolution, channel

Sl No.	Authors Name & Journal Published	River Name	Basin Area	River Size	MODIS and other Satellite Data used
	Agriculture, Ecosystems and Hydrology XIII				1 (0.620–0.670 µm — Red) and channel 2 (0.841–0.876 µm –Near Infrared) data were extracted from MODIS level 1b (MOD02QKM and MYD02QKM)
5	Tarpanelli A. et.al. (2017), Remote Sensing for Agriculture, Ecosystems, and Hydrology XIII,	Upper Tiber River	17,375 km^2	406 km long	MODIS 250 m resolution; 2006-2010 time series; MODIS channel 1 (0.620-0.670 µm) and channel 2 (0.841-0.876 µm) data were extracted from MODIS level 1b (MOD02QKM and MYD02 QKM)
6	Kwak Y. et.al. (2014), Artificial Life and Robotics, Daejeon, Korea	Indus River	1,165,500 km2	2900 km long	1. MODIS L3 8-day surface reflectance product (MYD09A1), 500 m resolution 2. DEM HydroSHEDS 15 arc-sec resolution 3. ALOS PALSAAR, PALSAR level 1.5 is a 16-bit unsigned integer and spatial resolution of 12.5 m with 70 km swath in high-resolution mode (HH polarization).

2.5 Types of Hydrologic Models

The rainfall-runoff model is a numerical model which defines the relationship between the rainfall-runoff in a catchment area, drainage basin, and watershed. It can be classified into lumped and distributed models, and deterministic and stochastic models. Lumped and distributed models are based on the model boundaries as a function of space and time. A deterministic model depends on different rules which will give similar output for a single arrangement of input values, whereas, in stochastic models, outputs are at least partially random. In lumped models, the watershed is spatially averaged, or regarded as a single point in space without dimensions whereas a distributed model studies the hydrologic procedures taking place at various points in space and describes the model variables as functions of the space dimensions had classified the models as event-based and continuous models (Chow et al., 1988; Wheater et al., 2008). The former produces output only for specific time periods while the latter produces a continuous output. According to Jackson et al. (2011), conceptual models are based on two principles: first of all, the structure of the model is quantified before any modeling is completed. Furthermore, not all model parameters are directly physically interpreted. Therefore, at least some conceptual model parameters must be estimated by calibration alongside observed data. Conceptual models usually characterize all the hydrological elements that are considered important to the input and output relationships of the catchment area.

There are many models for flood-inundation analysis, such as HEC-HMS, HEC-RAS, or a combination of both models. The HEC-HMS and HEC-RAS are hydrological models developed by the US Army Corps of Engineers. The HEC-HMS model is designed to estimate the comprehensive hydrological procedures of a dendritic catchment (Schaffenberg & Fleming, 2013). It can be used for flood analysis, flood frequency studies, flood alerts systems, reservoir, and overflow capacity studies, and many more (Samarasinghe et al., 2010). Both continuous and event-based can be applied in the model.

The HEC-RAS model is used for both steady, unsteady, one-dimensional, gradually varied flows in both natural and man-made river channels. HEC-RAS furthermore, enables sediment flow/ mobile bed calculations and water temperature modeling. Though, operators may find problems with mathematical uncertainty in unsteady analysis, especially on steep and/ or highly dynamic rivers and streams. In many cases, HEC-RAS can be used to overcome the instability problem caused by flow problems. Moreover, the combination of two different models can cause errors and may require many input datasets, which is difficult in a data-scarce region.

2.6 RRI Model

The RRI model is a distributed hydrological model which works on two-dimensional diffusion-wave equations to estimate water depths in each orthogonal grid cell and instantaneously incorporate the procedures of rainfall, runoff, and the propagation of flood inundation. It is widely used in different parts of the world, for instance, Bhagabati and Kawasaki (2017) performed the application of the RRI model in a limited data region in the Bago River basin, Myanmar. The model was calibrated for the 2011 flood event and validated for 2014 and 2015 flood events using observed discharge data. The model performed well for both high flows and low flows, respectively. Even though the estimated model streamflow displayed good agreement with observed streamflow, the estimated inundation area presented some inconsistencies due to some inadequacy of data.

Fattah et al. (2018) performed Rainfall-Runoff-Inundation (RRI) model for the 1,000-year return period in the Wadi Samail region, Oman. The study performed a sensitivity analysis for the governing model parameters which demonstrates that Manning's roughness coefficient for channel and hillslope are the significant parameters followed by the soil depth, porosity, and lateral saturated hydraulic conductivity. The most severe tropical cyclones in Oman, Gonu-2007, and Phet-2010 were applied to calibrate and validate the RRI model. From the result analysis, it was found that the RRI model could proficiently estimate the extreme weather conditions in the study area.

Naing (2014) conducted a study for flood inundation analysis by using RRI Model in Chindwin River, Myanmar. To develop flood hazard maps, different return periods such as 10, 50, and 100 years and the HEC-RAS model were applied. The generated maps were compared which was obtained by the Department of Meteorology and Hydrology. The results were obtained by the comparison of flood hazard maps, where both models showed similar high-risk inundated areas.

Nastiti et al. (2015) carried out Rainfall-Runoff-Inundation (RRI) model for inundation in West Java, Indonesia. The study was designed to build an enhanced RRI model with partial data and carry out a comparison between the model simulated inundation extent with the observed flood inundation map of the area.

Rasmy et al. (2019) conducted the Water and Energy Budget-based Rainfall-Runoff-Inundation (WEB-RRI) model in the Kalu (wet) and Mundeni (dry) River basins, Sri Lanka. The data used in this study were river discharge data, MODIS, Global Land Evaporation Amsterdam Model (GLEAM ET) data, and both ground and satellite inundation maps. The model was well calibrated and validated which approves to be extremely useful for stimulating the long-term (~20 years) observed streamflow which shows a Nash value of about 0.89. The model simulation on both basins was performed with averaged Evapotranspiration (ET) fluxes and the ET trends agreed better with GLEAM (RMSE: ~0.7–0.95 mm/day, correlation: ~0.35–0.39) than with MODIS (RMSE: ~0.96–1.04 mm/day, correlation: ~0.14–0.25). The inundation area obtained from the model showed reliable results with the ground and MODIS-driven inundation area maps.

Sayama et al. (2020) conducted a study on the reliability of hydrological modeling in the Mekong River Basin, Thailand. Rainfall-Runoff-Inundation (RRI) model in this basin was estimated using the observed precipitation data and five gridded precipitation datasets including Asian Precipitation-Highly-Resolved Observational Data Integration Towards Evaluation (APHRODITE), Global Precipitation Climatology Centre (GPCC), Precipitation Estimation from Remotely Sensed Information using Artificial Neural Networks- Climate Data Record (PERSIANN-CDR), Global Satellite Mapping of Precipitation- Microwave-Infrared Combined Reanalysis Product GSMaP (RNL), and Tropical Rainfall Measuring Mission (TRMM- 3B42V7) from 2000 to 2007. The results obtained from the estimated streamflow data specified that TRMM, GPCC, and APHRODITE performed better than other datasets. The statistical index of the yearly maximum flooded areas specified comparable decisions and provided valuable guidance for the application of gridded precipitation in hydrological modeling of the study area.

Yoshimoto and Amarnath (2017) carried out Rainfall-Runoff-Inundation (RRI) model for inundation in Mundeni Aru River Basin, Sri Lanka. The study was performed using

Satellite Rainfall Estimate (SRE) products (PERSIANN, TRMM, and GSMaP) which were analysed in the RRI model. The PERSIANN data was successful for estimating long-term variations in streamflow data. Results obtained from pre-processed satellite precipitation data tended to be underestimated compared to observed precipitation data. However, using scaling factors to modify precipitation data improved runoff simulation. The application process and proposals identified in this study will help authorities make more accurate assessments about early flood alerts and rapid flood forecasting, especially in regions with inadequate field data.

Table 2-3 represents the description of the RRI model used along with other satellite data used in various studies.

Table 2-3: Literature review summary for the RRI model

Sl No.	Name of Paper	Authors Name & Journal Published	River Name	Catchment Area	River Size	Satellite Data used
1	Consideration of the rainfall-runoff-inundation (RRI) model for flood mapping in a deltaic area of Myanmar	Bhagabati S. and Kawasaki A. (2017), Department of Civil Engineering, The University of Tokyo, Japan	Bago River	4,893 km^2	335 km long	1. RADARSAT-2 (2015) flood-water extent analysis map 2. HydroSHEDs (DEM) 90 m Resolution 3. Land cover map-(2009) GlobCover
2	Rainfall-Runoff Modeling for Extreme Flash Floods in Wadi Samail, Oman	Fattah et al. (2018); Journal of Japan Society of Civil Engineers	Wadi Samail River	1,741 km^2	5,100 m long	SRTM DEM, 3-sec resolution
3	The application of Rainfall-Runoff-Inundation (RRI) model for inundation case in upper Citarum Watershed, West Java-Indonesia	Nastiti K.D. et al. (2015), Procedia Engineering 125	Upper Citarum River	1,800 km^2	240 km long	DEM-HydroSHEDS 15-arc second resolution
4	Development Of Water And Energy Budget-Based Rainfall-Runoff-Inundation Model (WEB-RRI) And Its Verification In The Kalu And Mundeni River Basins, Sri Lanka.	Rasmy et al. (2019); Journal of Hydrology	Kalu Ganga	2,800 km^2	129 km long	MODIS 500 m resolution and GLEAM ET data
			Mudeni Aru	1,375 km^2.	86 km long	
5	Comparison of gridded precipitation datasets for rainfall-runoff and inundation modeling in the Mekong River Basin	Sayama et al. (2020); Plus, One, Remote Sensing Solutions	Mekong River	795,000 km^2	4,909 km long	APHRODITE, GPCC, PERSIANN-CDR, GSMaP (RNL), and TRMM (3B42V7) from 2000 to 2007

Sl No.	Name of Paper	Authors Name & Journal Published	River Name	Catchment Area	River Size	Satellite Data used
6	Applications of Satellite-Based Rainfall Estimates in Flood Inundation Modeling—A Case Study in Mundeni Aru River Basin, Sri Lanka	Yoshimoto S. and Amarnath G. (2017), International Water Management Institute (IWMI), Remote Sensing	Mundeni Aru River	1,300 km^2	224 km long	1. PERSIANN 0.25-degree, Multiple satellite infrared data 2. TRMM (3B42 V7)0.25 degree, 3. GSMaP (V6 reanalysis) 0.10 degree 4. DEM HydroSHEDS 30-arc-second resolution

Following are some of the advantages of the RRI model:

- Lowland flood simulations can be estimated using a 2D diffuse wave approximation model.
- Many hydrological processes can be applied to the RRI model, including vertical infiltration in the plains, transverse infiltration in the mountains, evapotranspiration, and dam effects.
- Both global data and satellite-based rainfall data can be used.
- The outputs given by the model are discharge, inundation area, and water level of the area.
- This model investigates both hydrological processes from precipitation to runoff and flood inundation in river basins simultaneously. It eliminates the two-stage simulation that is performed. It is used in traditional flood analysis models where the river channel runoff model first calculates flow rates and then the flood inundation model calculates this as a further considering the boundary conditions of the study area.

Following are some of the disadvantages of the RRI model:

- For bigger catchment areas, using of finer resolution of DEM takes more time for the run time of the model.
- Usage of finer resolution of DEM requires a high-quality computer to minimize the run time and to avoid any compatibility issues with the model.

For flood analysis, the calculation of simulated discharge and identification of inundated areas are important. Both hydrologic and hydraulic models are required to calculate discharge and flood inundation areas in river basins. However, the RRI model can simultaneously calculate precipitation to runoff and flood inundation, which eliminates the two-stage simulation and take less time to generate the results. Since each model will represent the real situation at a certain level which is evaluated by the accuracy of that model, using two models will even lower the total accuracy of the results. Considering the RRI model abilities which can model the hydrologic and hydraulic process simultaneously, will increase the overall accuracy of the results. Thus, due to the above advantages, the RRI model is selected for this study area.

2.7 Methods for Selection of Averaging of Point Rainfall over an Area

There are different methods for the selection of averaging of point rainfall over an area, such as Thiessen Polygon, Kriging and Inverse Distance Weighted (IDW), etc. Following are some of the literature reviews that presented the comparison of these three methods:

An assessment of interpolation techniques indicates the evaluation of the accuracy of interpolation techniques to examine the direct impact of rainfall on runoff and discharge at the basin outlet. To compare the three interpolation methods, it was applied for simulation of river runoff using the WetSpa model and compared the simulated daily values of the catchment water runoff with the observed data. The results showed that according to the data on maximum discharges, the Thiessen Polygon method was better than the other two methods (Zeinivand, 2015).

Another comparison between Inverse Distance Weighted (IDW) and Kriging showed that the kriging method of interpolation gives better results than the IDW method in terms of precession. Both methods give acceptable results, but the predicted height values are statistically equal to their respective known heights. The IDW method overestimates the interpolated values while the kriging method underestimates the interpolated height values (Ibrahim & Nasser, 2015).

A study for geostatistical interpolation approaches using Kriging and Radial basis function along with Thiessen polygon method and Inverse Distance Weightage was applied for Delhi and it has been demonstrated to have comparable methodologies in the prediction of annually rainfall values. The choice of interpolation method for predicting precipitation depends on the type of rainfall and the quality of the observations in the area. This study verified that kriging using linear interpolation and radial basis functions with other interpolation methods is satisfactory (Kumar & Tilak, 2018).

2.8 Model Discharge Evaluation Indices

For evaluating the discharge from the RRI model (goodness of fit), the indices (objective functions) selected for this study are Root Mean Square Error (RMSE), Mean Square Error (MSE), Coefficient of Determination (R^2), Nash Sutcliffe Efficiency (NSE), and Percent Bias (PBIAS).

The coefficient of determination is the portion of the total variation in the dependent variable that is explained by variation in the independent variable. The coefficient of determination is as well called r-squared and is denoted as R^2. With linear regression, the coefficient of determination is equal to the square of the correlation between the observed and simulated variables.

The range of values of R^2 depends on the type of model to be fitted; in standard cases such as linear least-squares regression models, they lie between 0 and 1. A value of 0 means there is no correlation at all, whereas a value of 1 means that the dispersion of the prediction is equal to that of the observation. Therefore, the higher the R^2 value, the better the model describes the data (Bucchianico, 2008).

The Root Mean Square Error (RMSE) is defined as the square root of the mean square, which is the arithmetic mean of the squares of a group of values. RMSE value near 0 indicates that the model can predict the data accurately (Barnston, 1992).

$$\mathrm{RMSE} = \sqrt{\frac{\sum_{i=1}^{n}(Q_{obs} - Q_{sim})^2}{N}} \quad [2\text{-}1]$$

Mean Square Error (MSE) is defined as the average of the squares of the errors, which means the average squared difference between the estimated values and the actual value. The value of MSE near 0 indicates that there is a good agreement of the observed data with the model.

$$\mathrm{MSE} = \frac{\sum_{i=1}^{n}\left(Q_{obs} - Q_{sim}\right)^2}{N} \quad [2\text{-}2]$$

where Q_{obs} is observed discharge, Q_{sim} is model simulated discharge, and N is the number of data points used for the calculation.

Nash and Sutcliffe (1970) developed a normalized statistic to measure residual variance in comparison to the observed variation. The NSE value indicates how closely the observed vs. simulated data graphic fits the 1:1 line (Moriasi, 2007). The formula is given in Equation [2-3].

$$\mathrm{NSE} = 1 - \frac{\sum(\mathrm{Q_{obs}} - \mathrm{Q_{sim}})^2}{\sum(\mathrm{Q_{obs}} - \mathrm{Q_{mean}})^2} \qquad [2\text{-}3]$$

where Q_{obs} is the observed value of discharge, Q_{sim} is the simulated value and Q_{mean} is the mean of observed data. NSE range varies from 0 to 1, with 1 being the intended value. NSE values between 0.6 to 1.0 are considered as good agreement with the model. However, NSE = 0 represents that the mean observed value is a stronger predictor of hydrological data than the simulated value, signifying poor performance.

The percent bias (PBIAS) or percent flow error (PVE) measures the average probability of simulated data to be bigger or smaller than observed data. It indicates general agreement between simulated and observed flows over a given time period (Gupta, 1999). PBIAS ideal value is 0.0, where low magnitude values indicate an accurate model simulation. A positive score suggests a bias that undervalues the model, while a negative value implies an overestimation.

$$\mathrm{PBIAS} = 1 - \frac{\sum_{i=1}^{n}(\mathrm{Q_{obs}} - \mathrm{Q_{sim}}) * 100}{\sum_{i=1}^{n} \mathrm{Q_{obs}}} \qquad [2\text{-}4]$$

Since the main purpose of this study was to analyse the flood peaks and inundation for the extreme events that have occurred in the Kalu Ganga basin, the most suitable objective functions which are used by many researchers for RRI model performance evaluation have been adopted in this study as well (Ramsy, 2019; Fattah et al., 2018).

Therefore, in this study for the development of the RRI model, RMSE, R^2, MSE, and NSE values were used for evaluating the model discharge indices.

CHAPTER 3

3 MATERIALS AND METHODS

3.1 Methodology

The overall methodology adopted for this study is shown in Figure 3-1. First of all the study area was identified and a detailed literature review was studied using different processes for flood inundation analysis. According to various literature of different hydrological models, the Rainfall-Runoff-Inundation (RRI) model can easily estimate precipitation to runoff and flood inundation simultaneously. The RRI model eliminates the two-stage simulation and takes less time to generate the results. Thus, the RRI model was selected for this study area. The required input datasets given in the RRI model were collected from respective departments. The inputs given to the model are rainfall data, Digital Elevation Model (DEM) of the study area, landuse map, and streamflow data for inflow to the river. All these inputs were applied in the RRI model and sensitivity analysis was calculated for the development of the model. Finally, the outputs were obtained as the discharge of the river, water level of the area, and flood inundation area. Afterward, the development of the model, the governing parameters were selected, parameter fine-tuning was evaluated to determine the model performance and calibration and validation of the model were performed.

Sentinel 1A SAR satellite images were downloaded from the European Space Agency (ESA) and pre-processed by using the Sentinel Application Platform (SNAP) software tool. Then from the corrected images, maximum likelihood supervised classification will be estimated using ArcGIS 10.5 software and the flood and non-flood classification of the satellite image will be defined. After the classification, flood and non-flood maps of the area were produced. This map was compared with the flood inundation area from the RRI model output and then a comparative study was performed using observed discharge and inundation area of the basin. The difference between the RRI generated flooded areas and satellite-generated flooded areas will be estimated by subtracting the area containing permanent water bodies from the landuse map of the study area. Finally, after that results, conclusions, and recommendations were obtained.

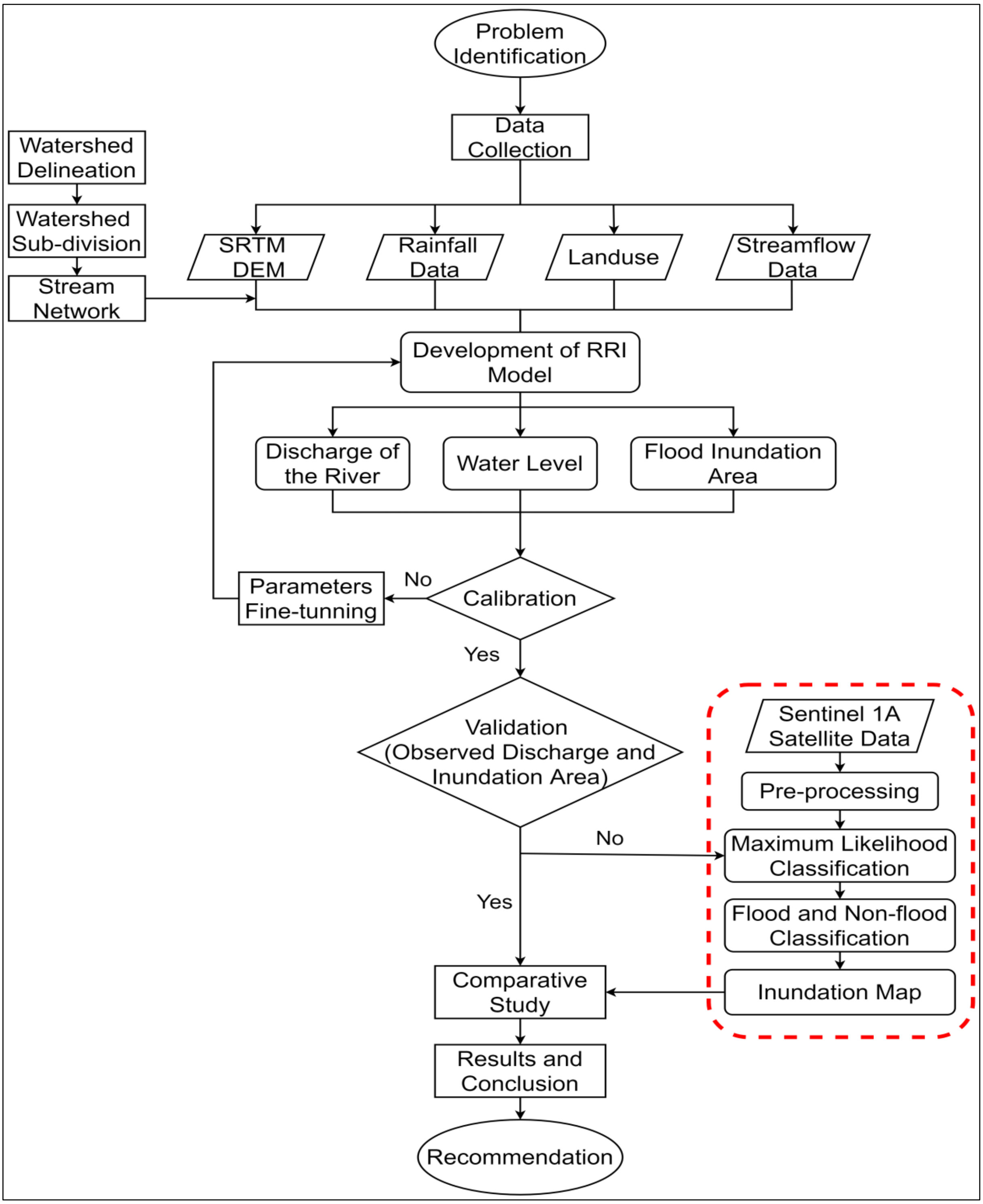

Figure 3-1: Methodology flowchart for the study area

The detailed methodology flowchart for inundation analysis is shown in Figure 3-2. For this study area, Sentinel 1A, GRD-IW mode of VV polarization, and spatial resolution of 20 m were acquired and pre-processed using the SNAP software. The purpose of radiometric calibration is to create an image in which the value of each pixel is directly related to backscattering from the surface (σ_0). It is essential for quantitatively analyzing the images. After this, the speckle filter was processed. The pixels representing water bodies have a smaller backscattering coefficient, $\sigma_{0,}$ compared to other features. Then, the Lee Sigma method has been applied to reduce the speckle noise effect (Senel et al., 2020). Although several other filters (i.e., Boxcar, Lee Sigma, and Gamma-MAP) are available in SNAP, the Lee Sigma, has been preferred since it has been reported to supply better results than the others (Tavus et al., 2019; Tavus et al., 2018). A geometric correction is required to remove the effects of side-looking geometry of SAR images. Therefore, the Range Doppler Terrain Correction algorithm has been applied to generate terrain-corrected and ortho-rectified SAR images. The digital topographic data, Shuttle Radar Topography Mission (SRTM)-3 arc sec, along with bilinear interpolation has been used as the base digital elevation model (DEM) for the correction (Anusha & Bharathi, 2019).

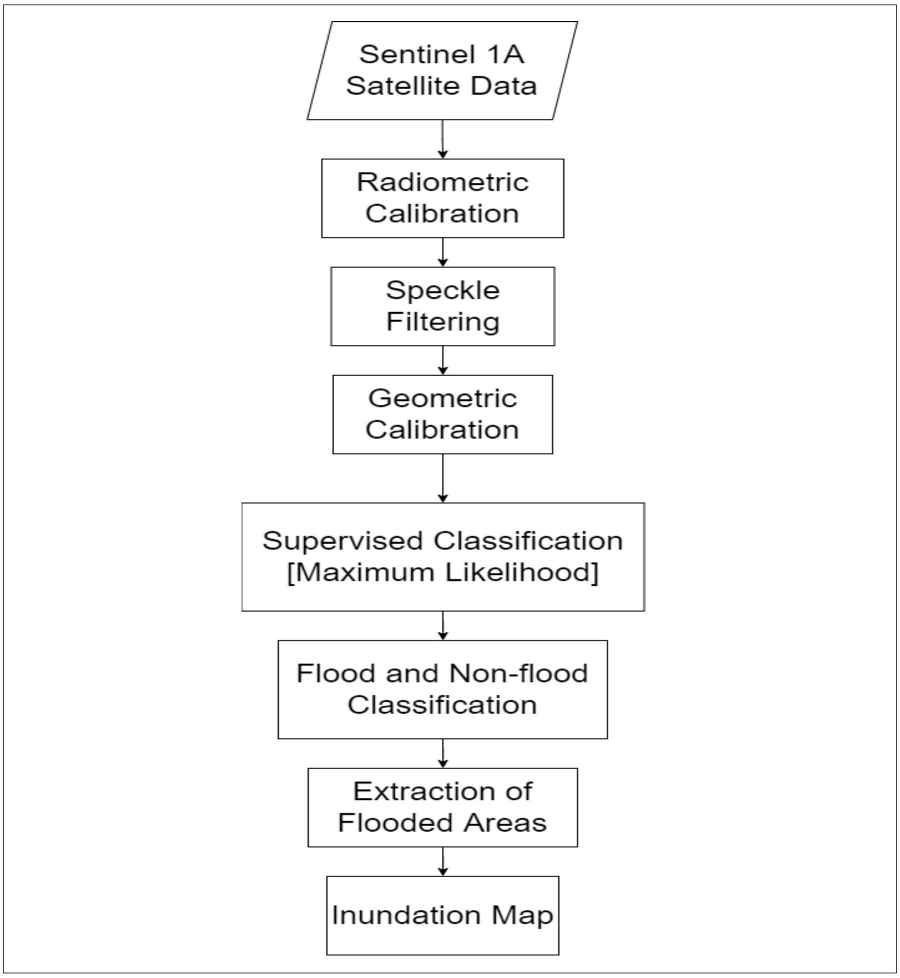

Figure 3-2: Methodology flowchart for the inundation analysis

After the correction, the image file was converted to tiff format and maximum likelihood supervised classification was applied by using ArcGIS software (Gomathi et al., 2018). In maximum likelihood classification, a threshold value for each class was obtained from the training datasets called the signature. Depending on the threshold value, the classifier estimates the likelihood probability of a given pixel that belongs to a specific class. All pixels are classified to a particular class based on the highest probability of the assigned class. The images are classified as flood and non-flood class and finally, extraction of flooded areas can be calculated and inundation maps can be generated (Gomathi et al., 2018).

3.2 Study Area

Kalu Ganga River is the second largest river basin in Sri Lanka. The river originates from Sri Padhaya peak and reaches the sea at Kalutara. The basin area is about 2,839 km^2 and lies in the Western Province and Wet Zone of Sri Lanka (Irrigation Department, 2017). The forests of Central Province and the Sinharaja Forest Reserve are the key components of water for the Kalu Ganga. The average annual precipitation in the basin is 4,000 mm, with an annual runoff of 4,000 million m^3. The Kalu Ganga Basin accounts for the largest amount of water available per capita annually. It is approximately 7,750 m^3, far exceeding the annual per capita water availability at 2,300 m^3 at the national level (Imbulana & Neupane, 2003). The following Figure 3-3, and Figure 3-4 represent the study area, slope map, and landuse map of Kalu Ganga Basin, respectively.

Figure 3-4 represents the slope of the Kalu Ganga basin where the range of slope is about 0-77 degrees. Figure 3-5 represents the landuse map of the study area. The area is mainly covered by forest along with rubber and tea cultivation in the upstream part of the basin. About 20 % of the area is homestead/ garden and heavily urbanized in the downstream part of the study area. Nearly about 16 % area is coconut cultivation, and 11 % area is paddy cultivation. Other cultivation like rubber and tea plantation is moreover present in the upper part of the catchment.

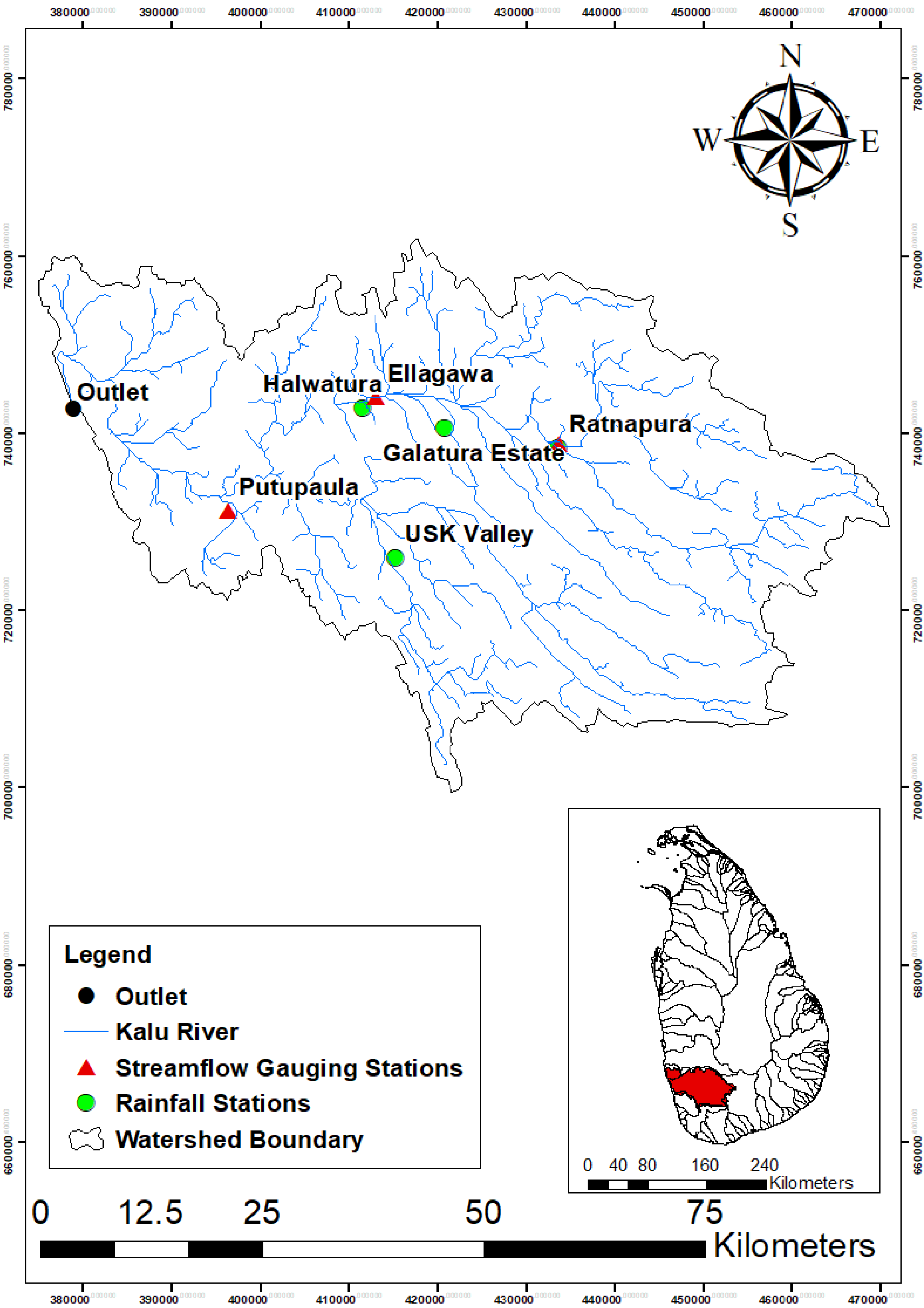

Figure 3-3: Study area

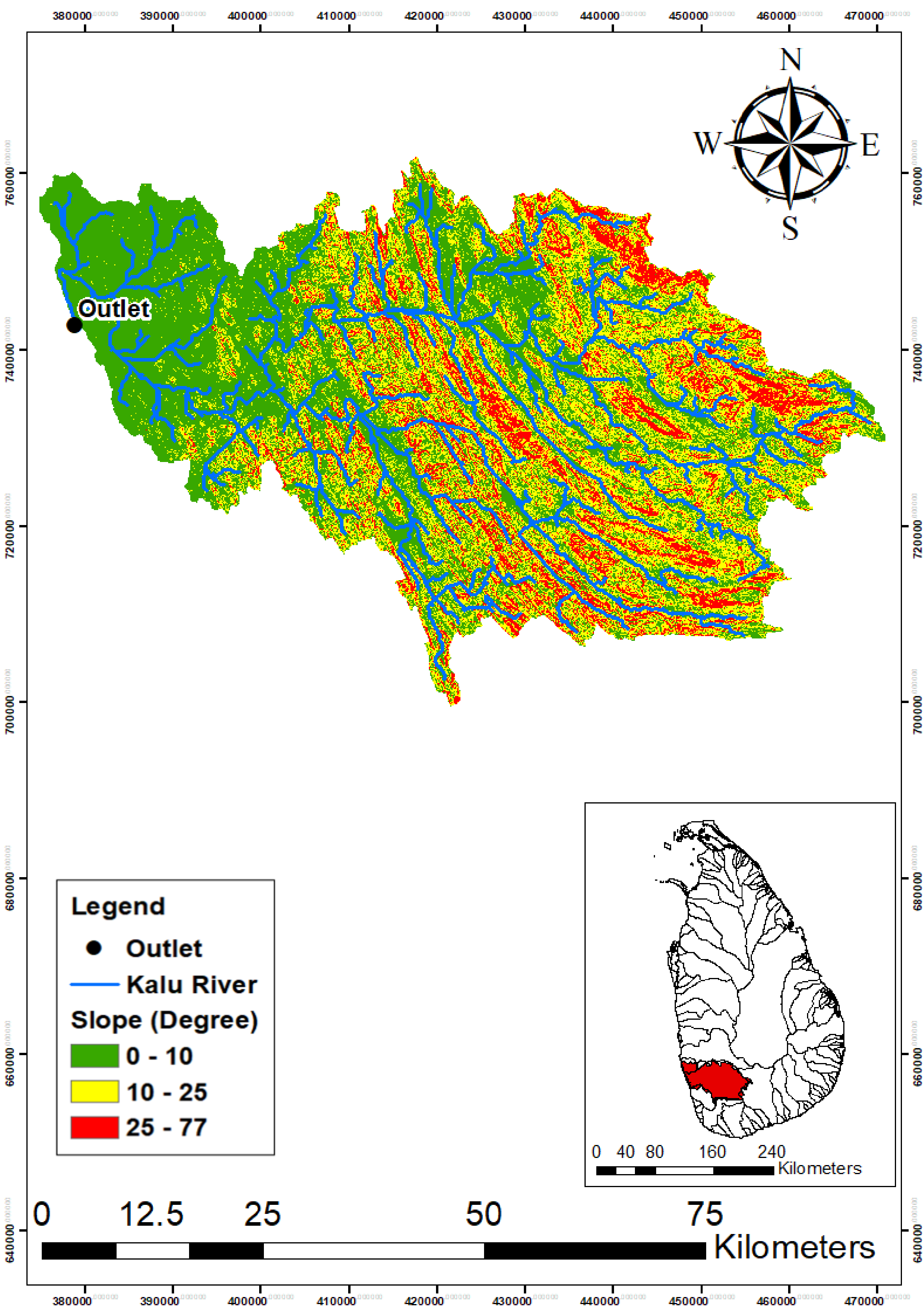

Figure 3-4: Slope map of Kalu Ganga River Basin *[Source: SRTM DEM http://srtm.csi.cgiar.org]*

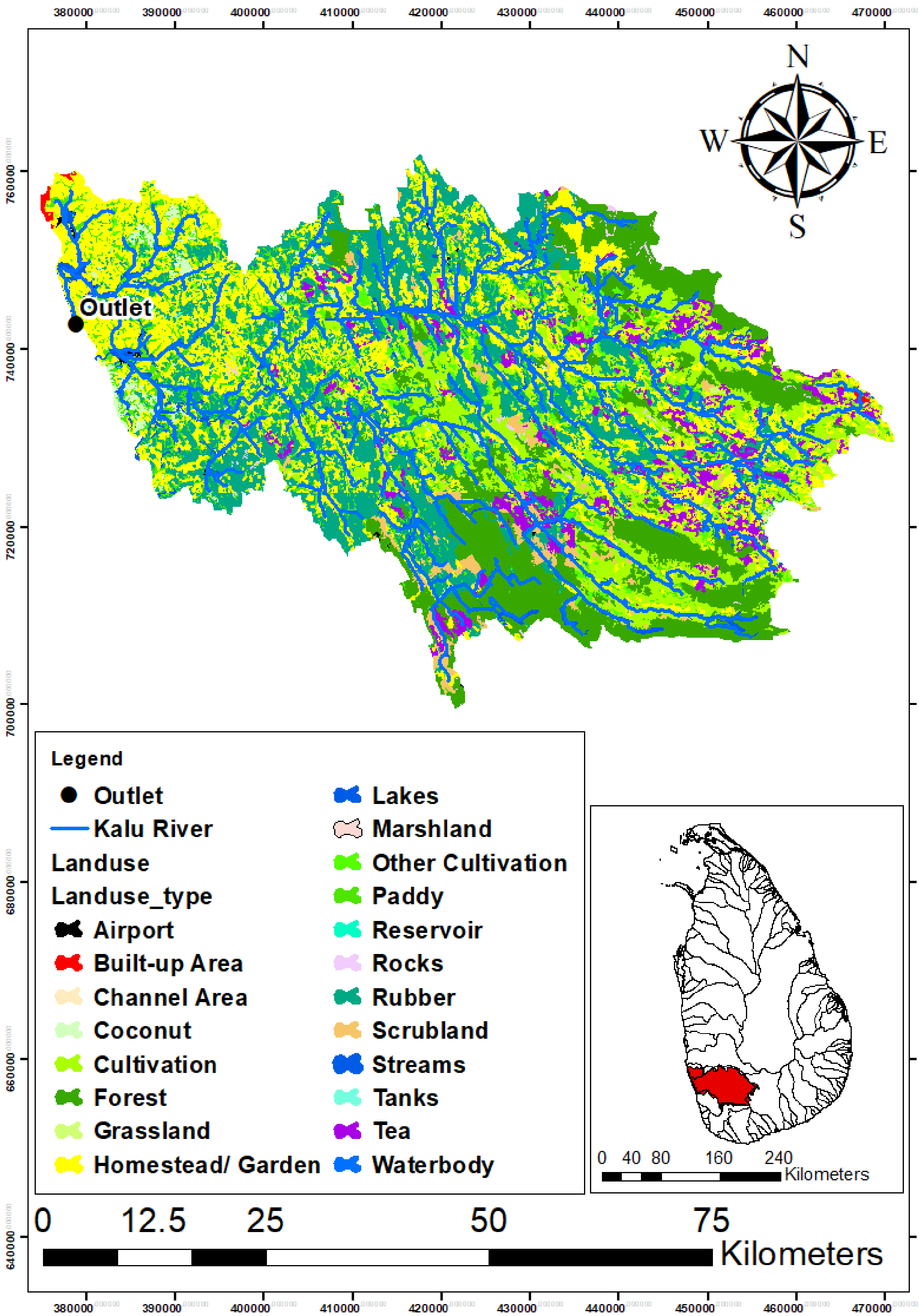

Figure 3-5: Landuse map of Kalu Ganga River Basin *[Source: Survey Department of Sri Lanka, 1999]*

3.3 Data Checking and Analysis

The data required for this study area were collected from their respective sources. Four rainfall stations are selected namely, Ratnapura, Galatura Estate, Halwatura, and USK Valley. There are three streamflow gauging stations, which are Ratnapura, Ellagawa, and Putupaula, out of which Ratnapura and Putupaula streamflow stations data were considered for applying in the model. The data required and their probable sources for the study are listed in Table 3-1.

Table 3-1: Data and data sources

Sl No.	Data	Temporal/ Spatial Resolution	Source
1	DEM	90 m DEM	SRTM http://srtm.csi.cgiar.org
2	Landuse	1:10,000 or 300 m resolution	Survey Department Sri Lanka or GlobCover 2009
3	Daily rainfall	30 years duration	Meteorological Department of Sri Lanka
4	Sentinel 1A	20 m resolution	https://scihub.copernicus.eu/
5	Daily discharge	20-year duration	Irrigation Department of Sri Lanka

3.3.1 Tools to be used for data processing

Following tools to be used for data processing:

- ArcGIS 10.5
- Rainfall-Runoff- Inundation Model (RRI)
- Sentinel Application Platform (SNAP)

3.3.2 Thiessen polygon for selection of rainfall gauging station

Thiessen polygon method was applied in ArcGIS 10.5 software for selecting the rainfall gauging stations. The streamflow data were collected from the Irrigation Department of Sri Lanka and rainfall data were collected from the Meteorological Department of Sri Lanka. Following Table 3-2 shows the data collected for the study area.

Table 3-2: Data collection

Sl No.	Station name	Data type	Resolution	Data collection period
1	Ratnapura	Streamflow	Daily Average	1977-1996 and 2006-2020
2	Ellagawa	Streamflow	Daily Average	1981-2020
3	Putupaula	Streamflow	Daily Average	1994-2017
4	Ratnapura	Rainfall	Daily	1961-2020
5	Halwatura	Rainfall	Daily	1961-2020
6	Galatura Estate	Rainfall	Daily	1961-2020
7	Usk Valley S/P	Rainfall	Daily	1961-2020

For the selection of rainfall gauging stations, the following steps are completed:

- The rainfall gauging stations were selected from the Isohyetal map of Sri Lanka and were plotted in the map and the Thiessen Polygon method was used in ArcGIS to assign areal significance to point precipitation values.
- Perpendicular bisectors are created to the lines joining each measuring station with those immediately surrounding it. These bisectors were built for the lines that connect each measuring station to the lines that surround it directly. These bisectors form a series of polygons where each polygon comprises a rainfall gauging station.
- After classifying, the weightage of each station was calculated and was be multiplied by the rainfall values of each station.

Figure 3-6: demonstrates the Thiessen polygon map of the study area along with the location of the rainfall stations. The highest weightage was obtained for the Ratnapura station, which was 0.41, followed by Halwatura station of about 0.28, USK Valley of about 0.21, and the lowest weightage was obtained for the Galatura Estate station which was 0.09.

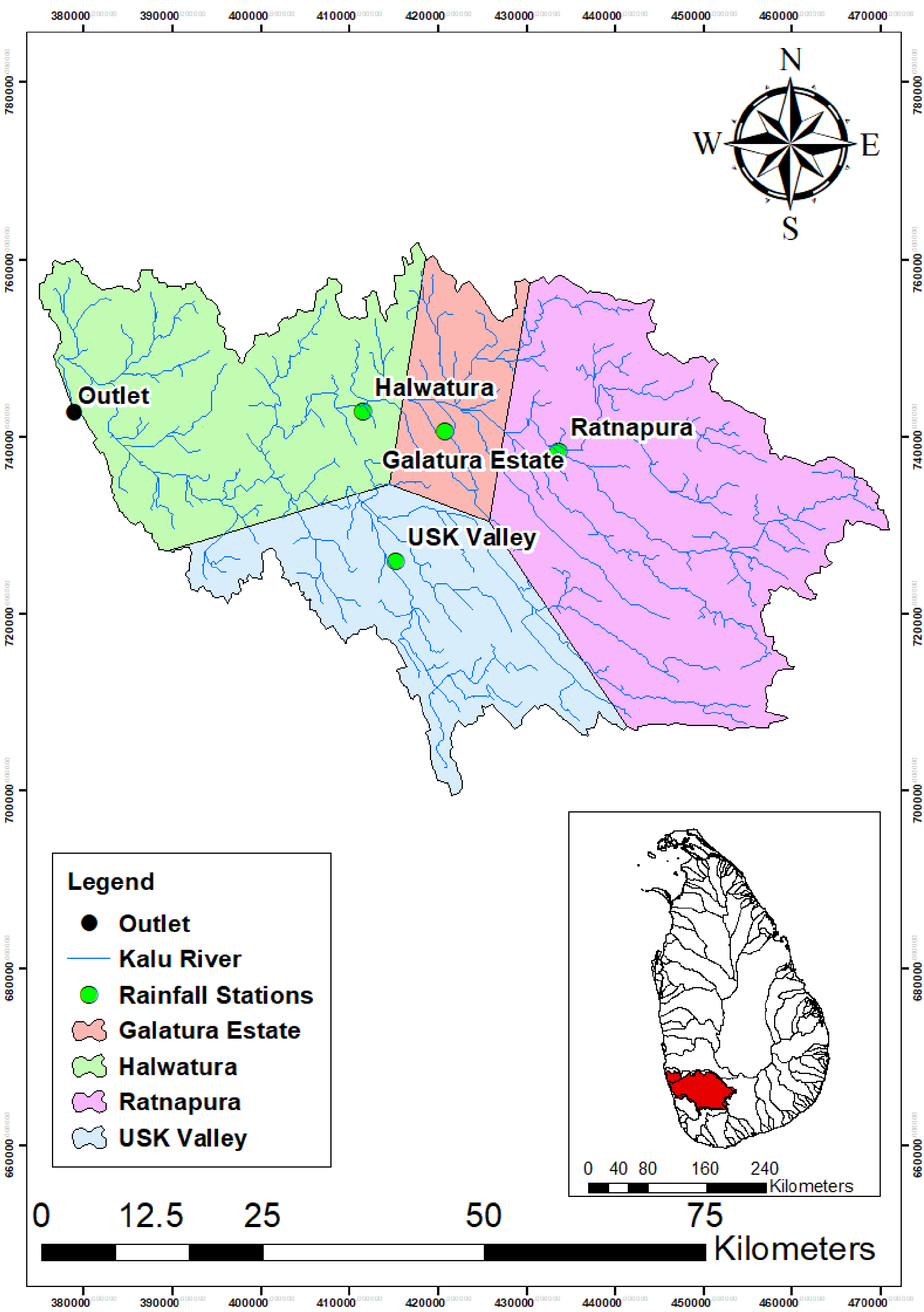

Figure 3-6: Thiessen polygon map of Kalu Ganga Basin

3.3.3 Data checking for missing values

Firstly, collected data was checked visually using excel tools like conditional formatting, charts, and graphs. Then computational checks were obtained through average and seasonal values. Rainfall data was arranged in chronological order with every station data in columns for easy comparison. Missing values were identified using the conditional formatting tools by visually observing the data sets even in monthly arrangements. A detailed table has been shown in Annexure 1, where the missing values were identified as negative values or blank cells.

3.3.4 Filling of missing values of rainfall data

Rainfall data were collected from 1969 to 2020 from the Meteorological Department of Sri Lanka. The percentage of missing data in the four rainfall stations are given below:

1. Ratnapura = 5.30 %
2. Galatura Estate = 1.33 %
3. USK Valley = 2.16 %
4. Halwatura = 3.50 %

Out of the four rainfall stations, Ratnapura has the maximum number of missing values and Galatura Estate has the least number of missing values. For filing of missing values of rainfall data, a linear regression method was applied. Linear regression determines the model relationship between two variables by fitting linear equations to the observed data. One variable is considered an explanatory variable and the other variable is considered a dependent variable. A linear regression line has an equation of the form:

$$Y = a + bX \quad [3\text{-}1]$$

where X is the explanatory variable and Y is the dependent variable. The slope of the line is b, and a is the intercept (the value of y when $x = 0$). A scatterplot graph was plotted which helps in determining the strength of the relationship between two variables. The following Figure 3-7 shows the scatterplot graphs of all the four rainfall gauging stations (Uyanıka, 2013).

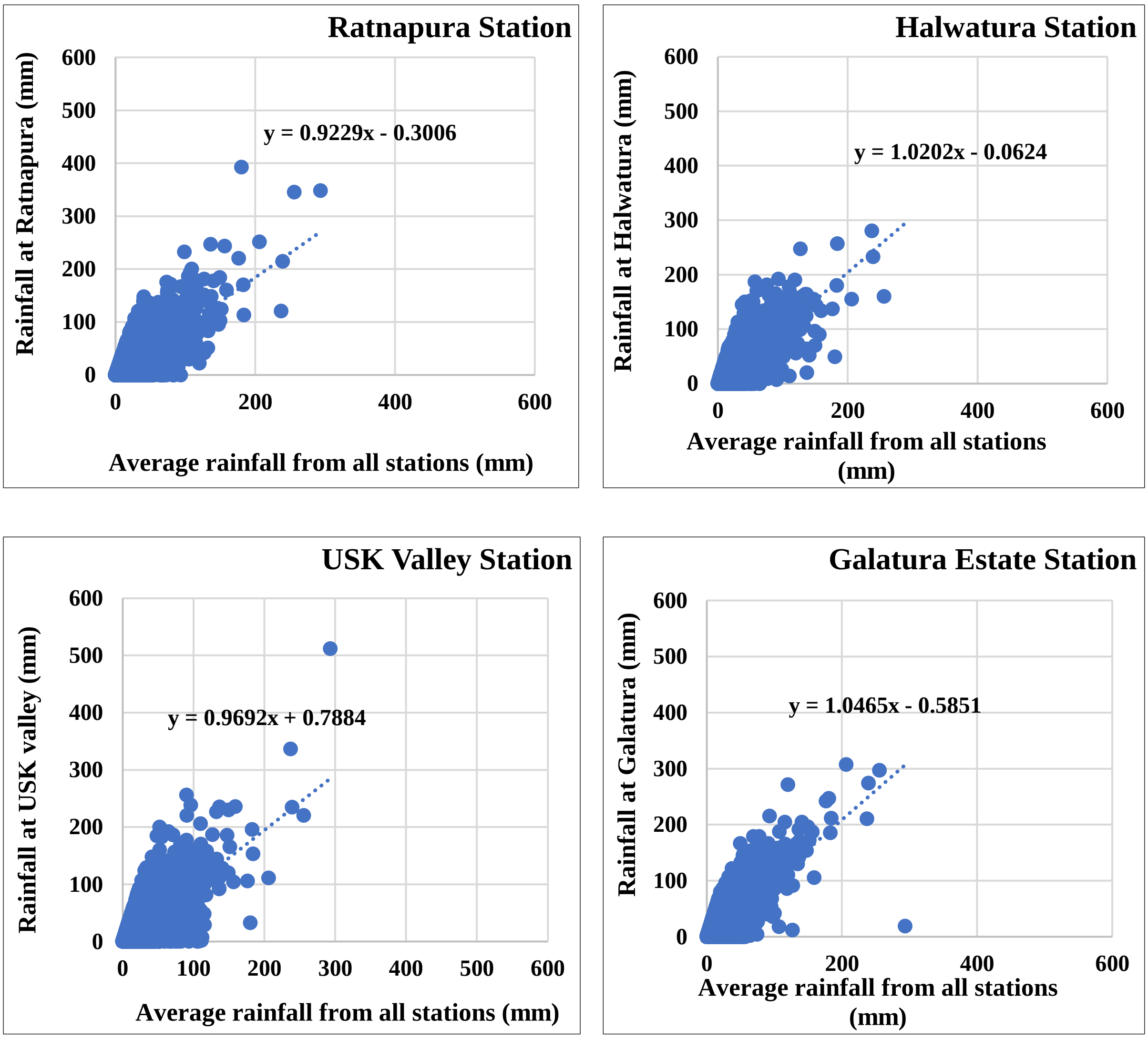

Figure 3-7: Linear regression analysis for Ratnapura, USK Valley, Galatura, and Halwatura rainfall gauging stations

3.3.4.1 Single mass curve and double mass curve analysis for all rainfall gauging station

To evaluate the consistency of the rainfall data, a single mass curve and double mass curve graph were plotted for all the rainfall gauging stations. The mass curve of rainfall is a plot of the accumulated precipitation against time, plotted in chronological order. Mass curves of rainfall are very useful in extracting information on the duration and magnitude of a storm. Moreover, intensities at various time intervals in a storm can be obtained by the slope of the curve. For non-recording rain gauges, mass curves are prepared from knowledge of the approximate beginning and end of a storm and by using the mass curves of adjacent recording gauge stations as a guide. Figure 3-8 represents the single mass curve of all the four rainfall stations. Figure 3-9 shows the single mass curve of all combined rainfall gauging stations. It can be seen that USK Valley has some inconsistency from the year 1993 to 2003. Other rainfall stations are fairly the same and show consistent behaviour of rainfall patterns.

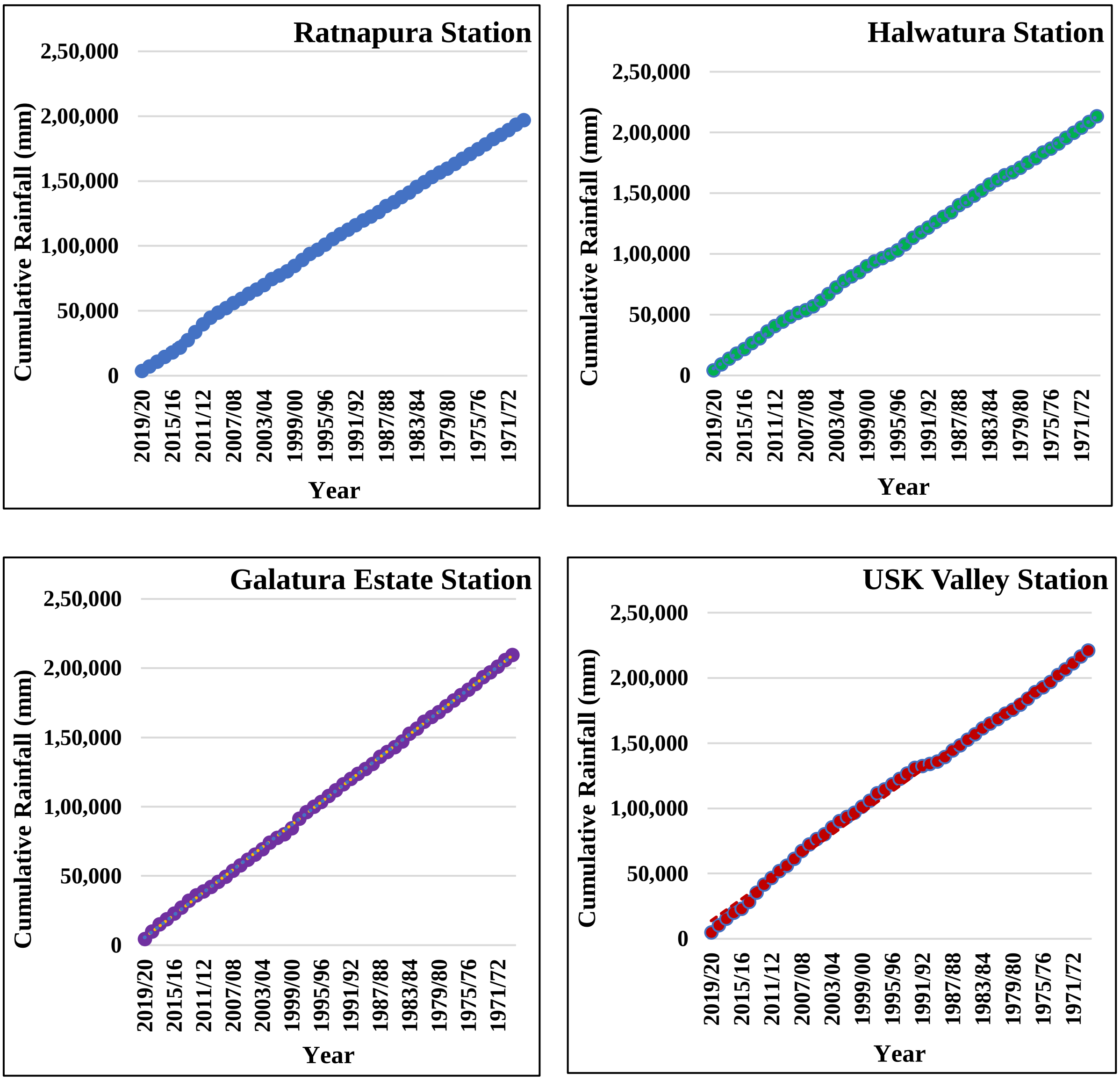

Figure 3-8: Single mass curve

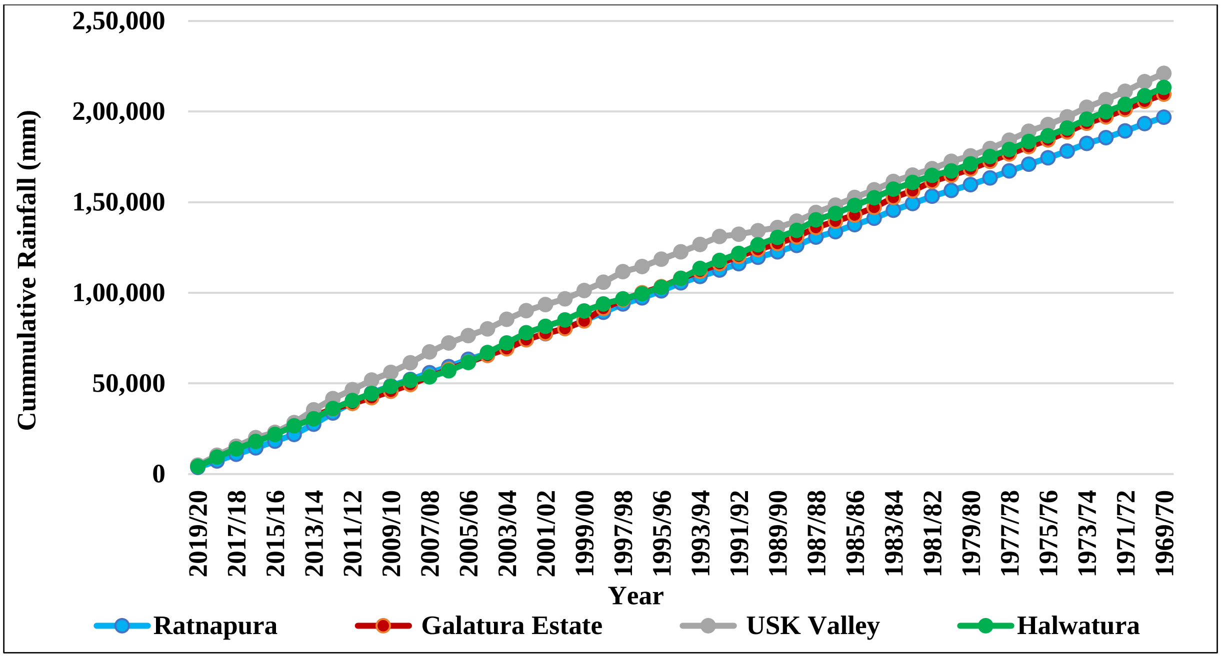

Figure 3-9: Single mass curve of all combined rainfall gauging stations

The double mass curve plots the cumulative data of one variable against the cumulative data of the second variable. A break in the slope of a linear function that fits the data is thought to represent a change in the relation between the variables. This approach provides a robust method to determine any change in the precipitation values.

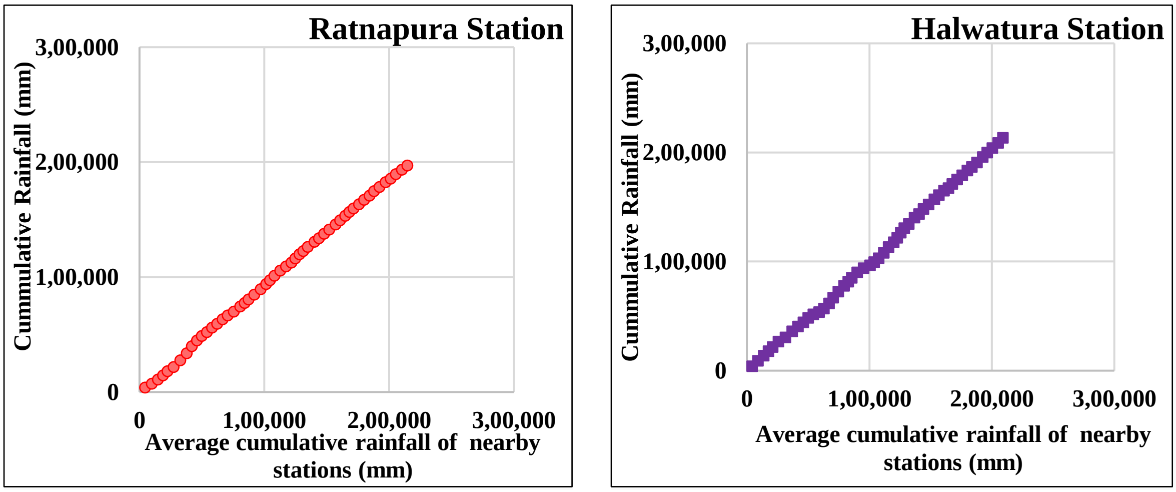

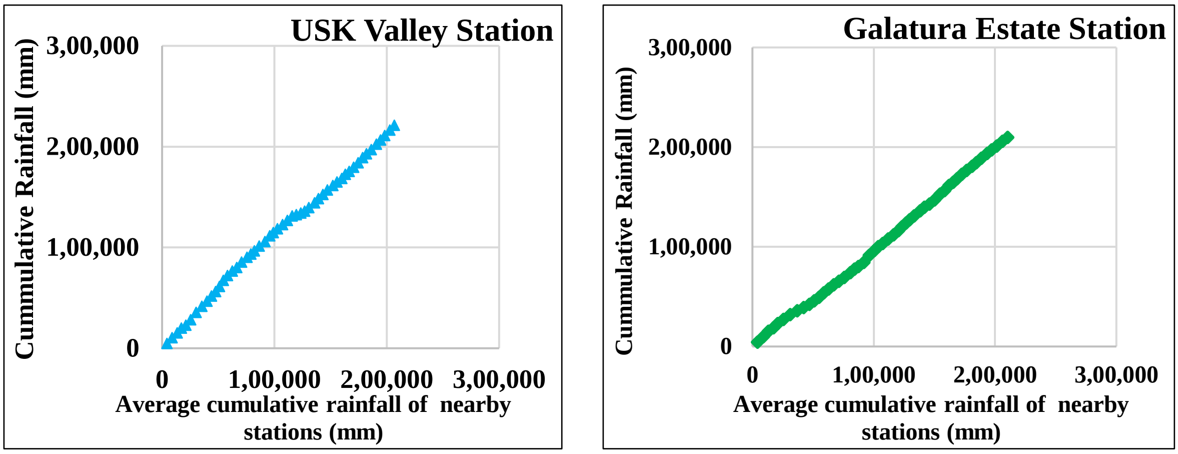

Figure 3-10: Double mass curve of all rainfall stations

Subsequently, when the rainfall data is plotted on an annual scale, the trend of the data can be observed by adding the trendline in the chart. The yearly variation of all the four rainfall station data was plotted on an annual scale which is shown in Figure 3-10. The graphs were plotted to check any missing values and inconsistency or irregularities of the dataset. Precautions should be applied while identifying outliers and it should be verified whether it is an extreme event or an outlier from other secondary sources. Figure 3-11 represents the yearly rainfall variation of all the four rainfall stations from the year 1969 to 2020. In this graph, USK Valley shows a different trend in the year 1989/90 and 1991/92. Other rainfall stations show a yearly rainfall variation between 3,500-4,500 mm per year.

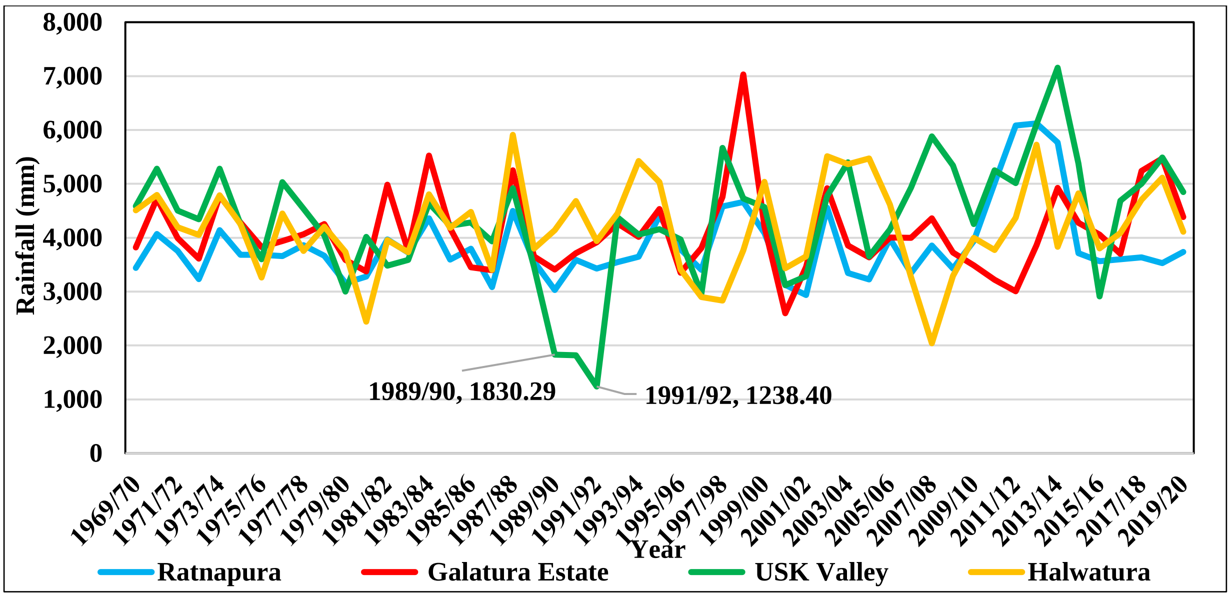

Figure 3-11: Yearly rainfall variation (mm) of Kalu Ganga Basin from 1969-2020

3.3.5 Seasonal trends

There are four seasons in Sri Lanka influenced by variation in rainfall throughout the year. First, inter-monsoon rainfall occurs during March and April which succeeds to south-west monsoon rainfall from May till September. October and November month experience second inter monsoon rainfall succeeded by north-east monsoon during December and ends in February. For checking seasonal trends in the Kalu Ganga basin, all the seasons were plotted for the year as shown below.

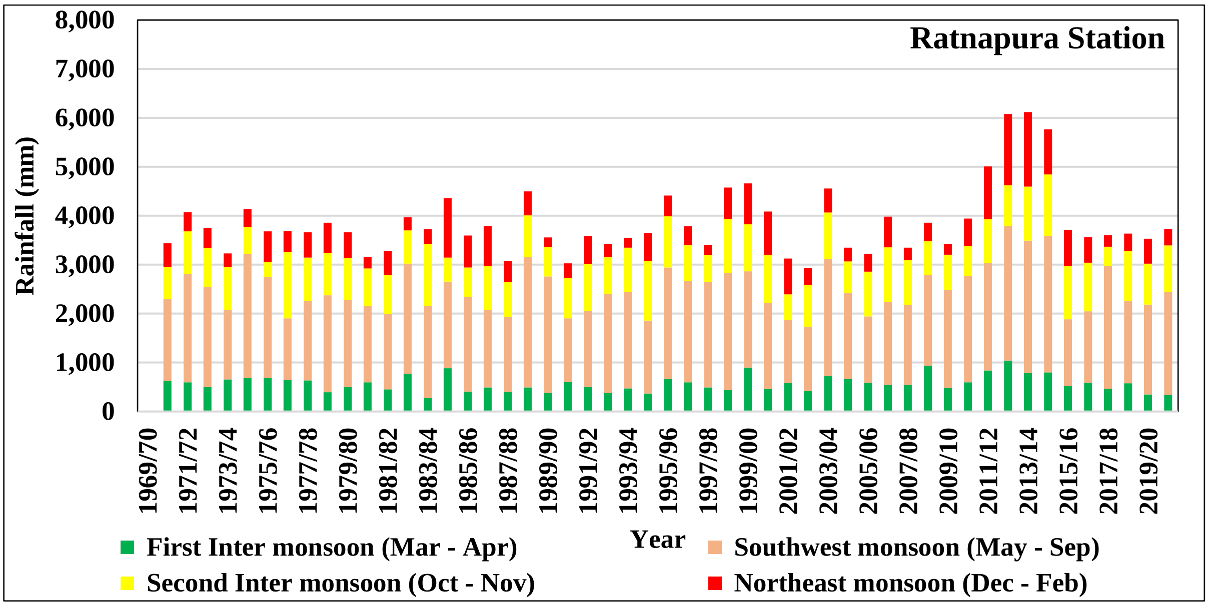

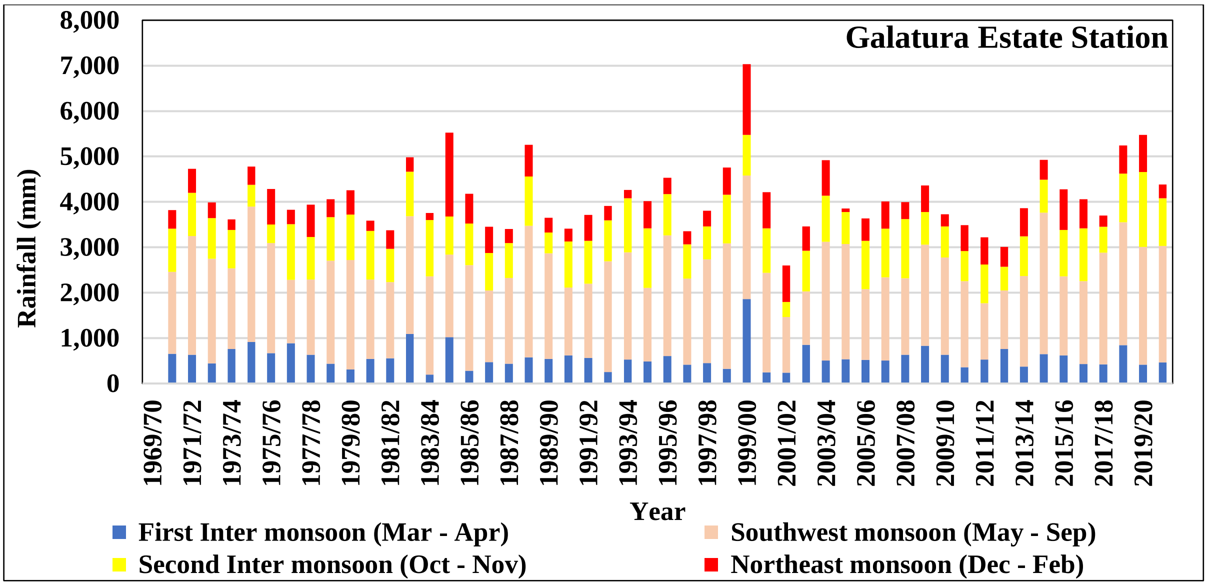

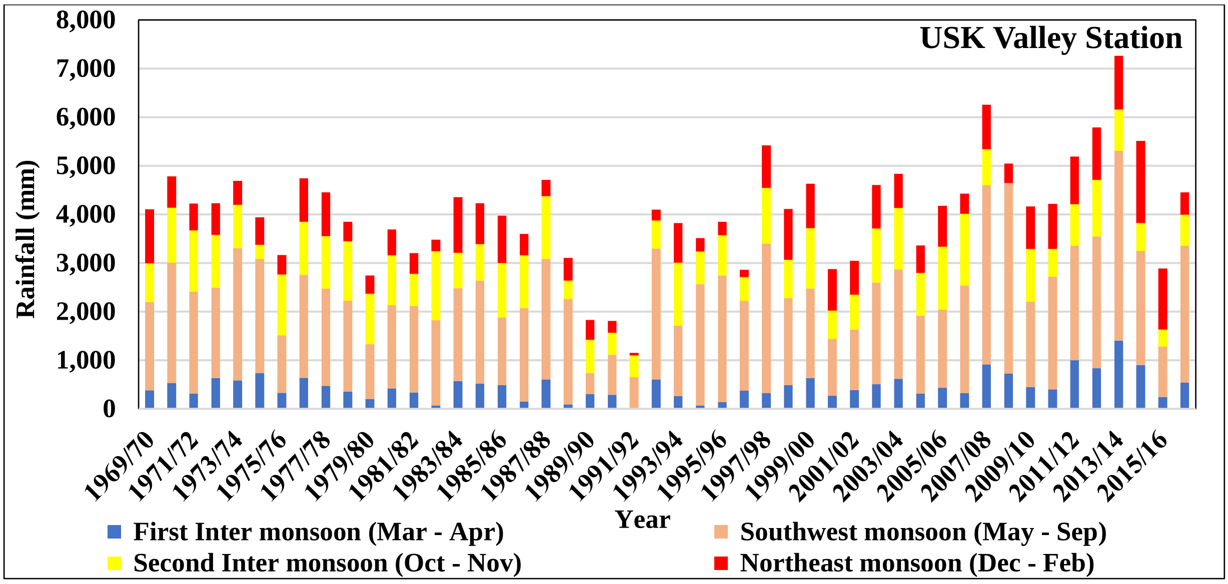

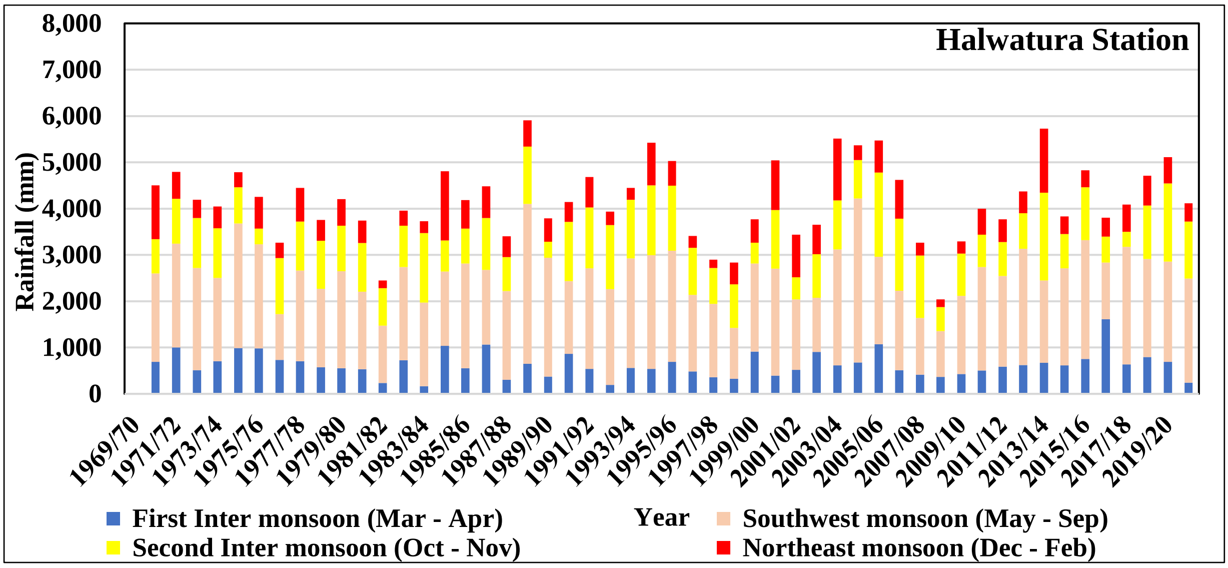

Figure 3-12: Seasonal variation of Ratnapura, USK Valley, Galatura Estate, and Halwatura rainfall gauging stations

From Figure 3-12 it can be seen that more rainfall is contributed during Southwest monsoon followed by Second Inter-monsoon rain in all the four rainfall stations.

Missing data can moreover be found from rainfall vs streamflow graph where any of the parameters does not follow the trend of other parameters usually indicate missing or outliers as shown in Figure 3-13 below for Ratnapura station. The following figure shows that there has been missing streamflow data from 1996 to 2006 for the rainfall values present in those years.

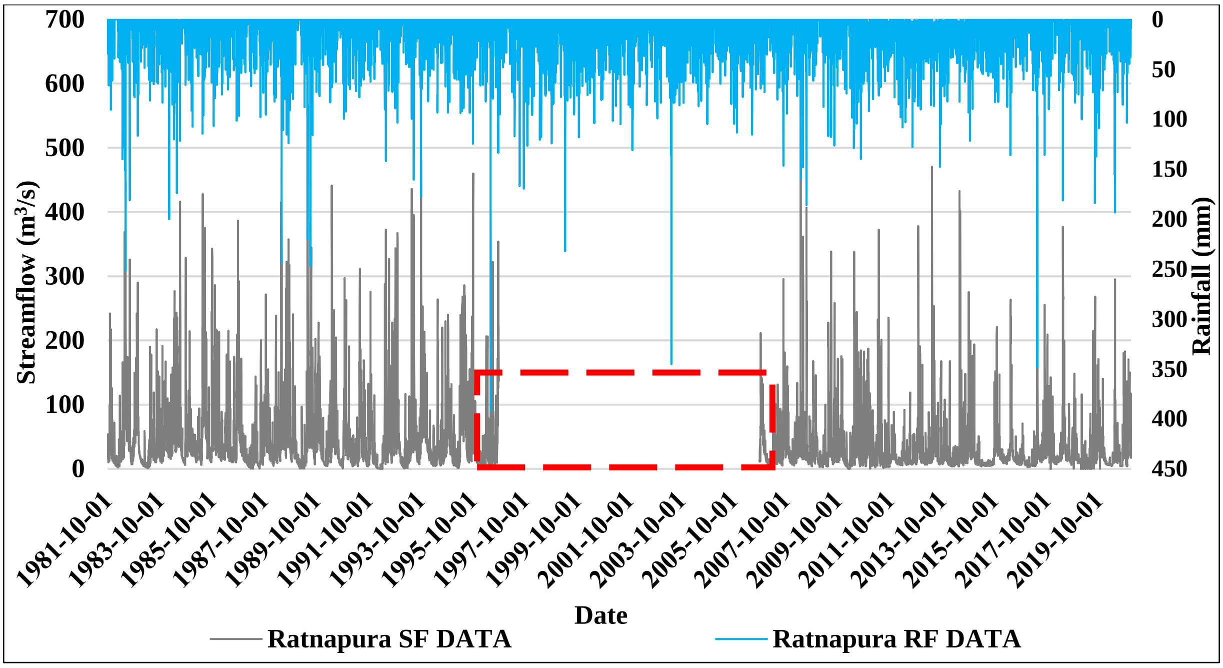

Figure 3-13: Rainfall and streamflow graph for Kalu Ganga Basin

The maximum, minimum, and median values of all the rainfall gauging stations are shown in the box plot graph in the following Figure 3-14. A box plot is a special type of diagram that shows the quartiles in a box and the line extending from the lowest to the highest value. The box plot distribution represents the variability of data, skewness of data, and the symmetry of data. It can moreover show any outliers that are present in the data, which generally falls far top or bottom side of the ordered data.

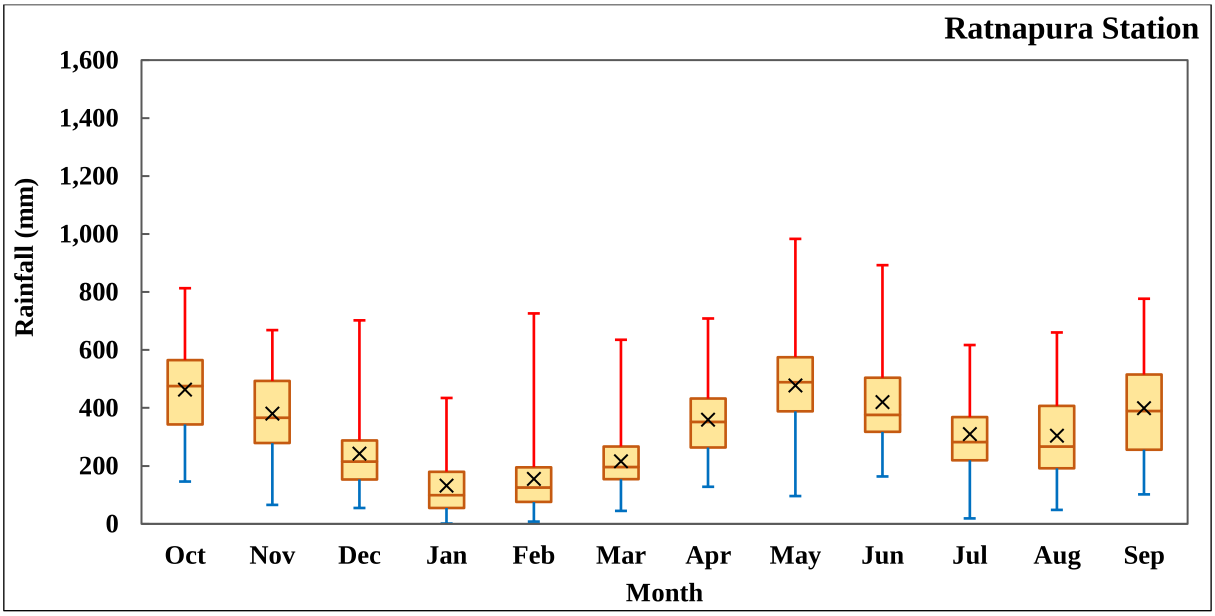

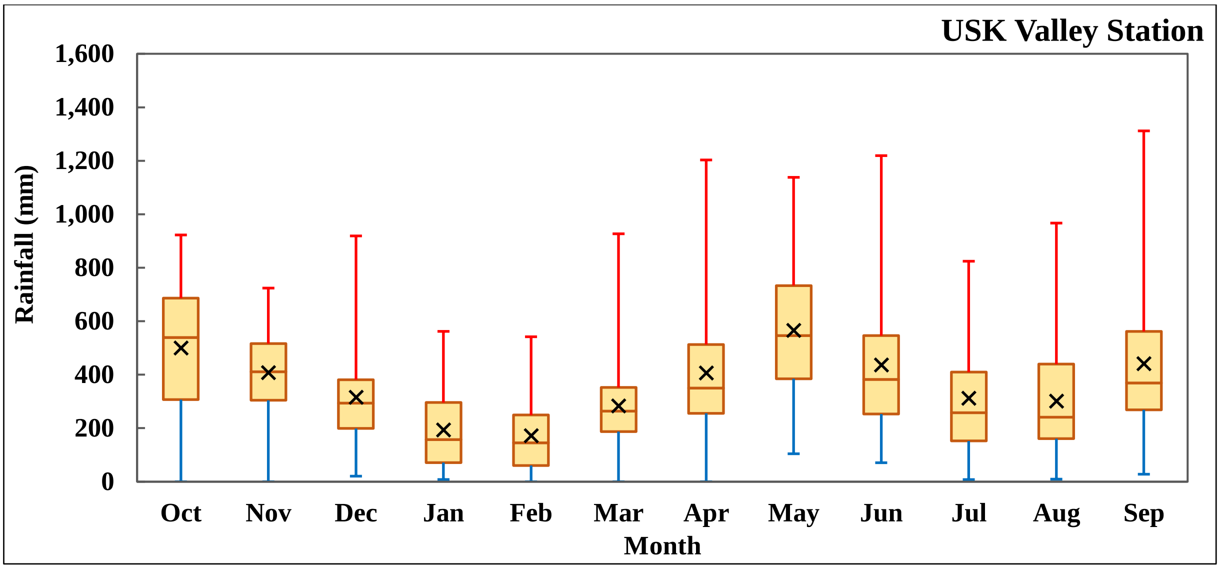

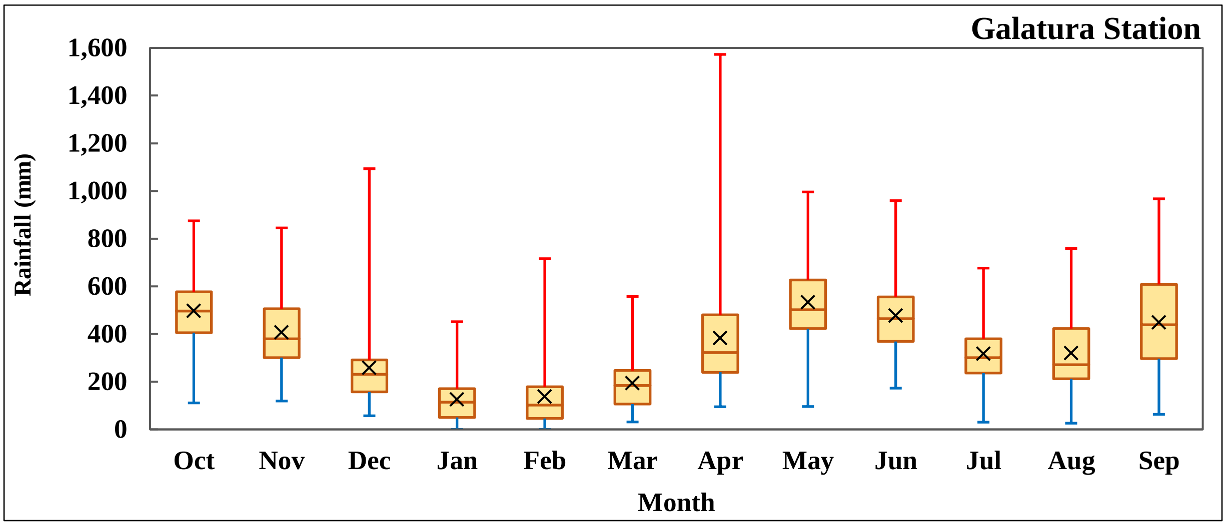

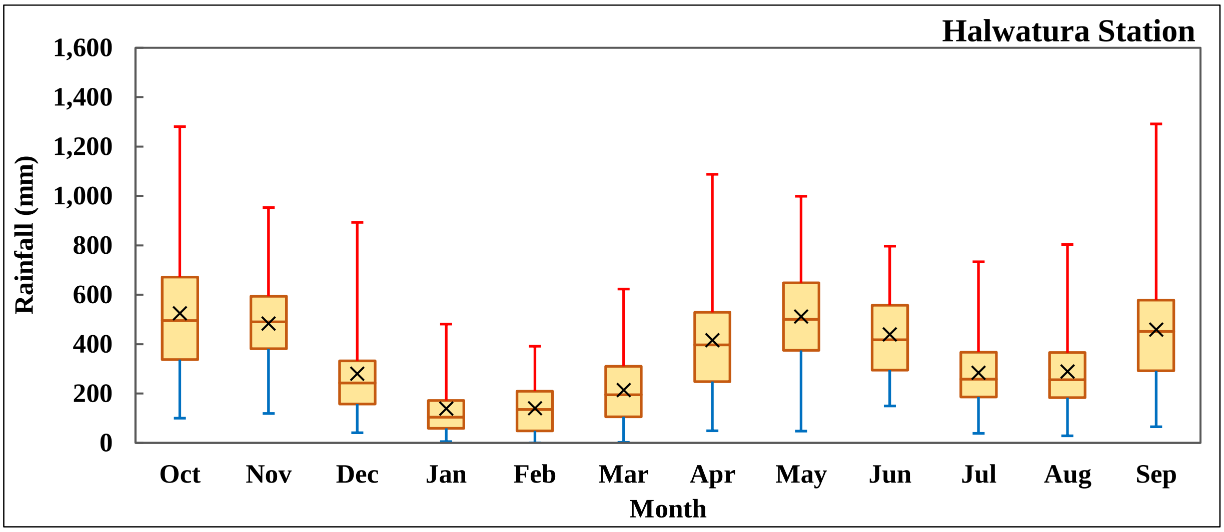

Figure 3-14: Box plot graph of all rainfall gauging stations

Figure 3-14 represents the box plot graph for all rainfall stations. Galatura rainfall station showed the maximum amount of rainfall during April compared to the other stations. The highest rainfall was recorded during April, May, and June in all the stations, while the lowest rainfall was recorded during January and February. All the stations showed a higher variation of rainfall in April, May, September, and October and lower variations of rainfall in January and February.

3.3.6 Streamflow data

The streamflow data were collected from the Irrigation Department of Sri Lanka of three stations- Putupaula, Ellagawa, and Ratnapura station. Streamflow data from 1994 to 2017 has been collected from Putupaula station, 1981 to 2020 has been collected from Ellagawa station, and 1981 to 1996 and 2006 to 2020 collected from Ratnapura station. The following graph shows the average annual streamflow, average monthly streamflow, and seasonal variations in the three streamflow gauging stations.

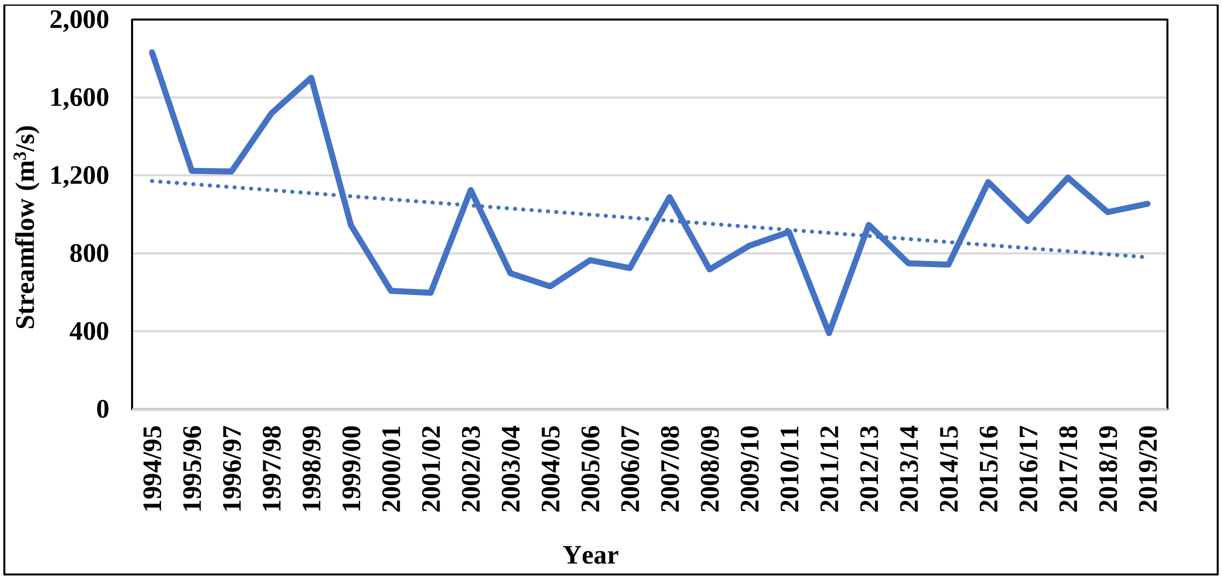

Figure 3-15: Annual total streamflow at Ellagawa station

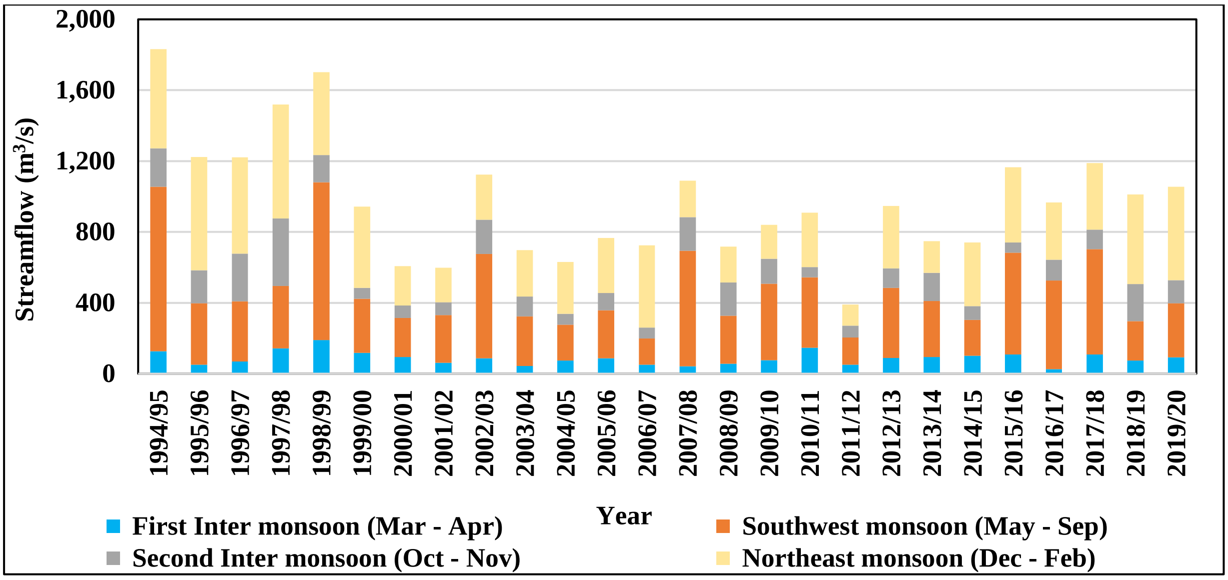

Figure 3-16: Seasonal variation of streamflow at Ellagawa station

Figure 3-15 shows that there has been decreasing trend in the average annual streamflow in the station. The seasonal variation of streamflow is plotted in Figure 3-16, and it can be seen that the maximum amount of streamflow is recorded during the Southwest monsoon season. The maximum, minimum, and average values of streamflow in the Ellagawa station are as shown in the graph below in Figure 3-17.

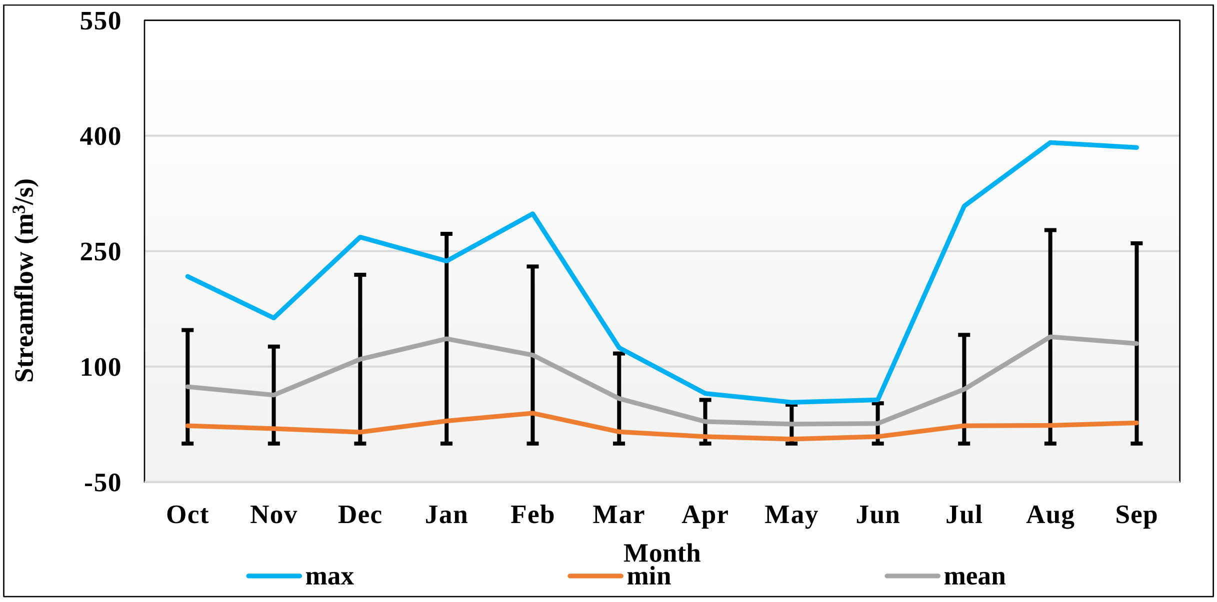

Figure 3-17: Maximum, minimum, and average streamflow- Ellagawa station

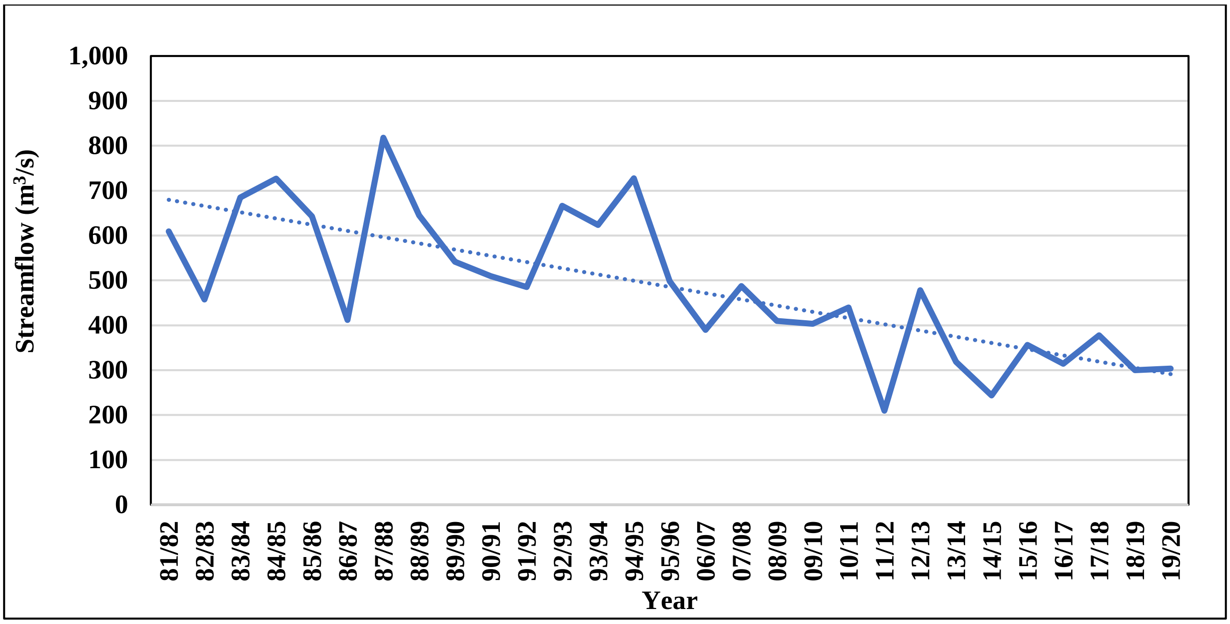

Figure 3-18: Annual total streamflow at Ratnapura station

Figure 3-18 represents the yearly variation of the Ratnapura streamflow station. The graph shows a decreasing trend from the year 1981 to 2020. The maximum streamflow recorded was about 800 m^3/s in 1987/88. Figure 3-19 represents the average monthly streamflow at Ratnapura station, where the monthly variation can be estimated. It can be noted that in June- 1984/85 the streamflow was maximum as compared to other months.

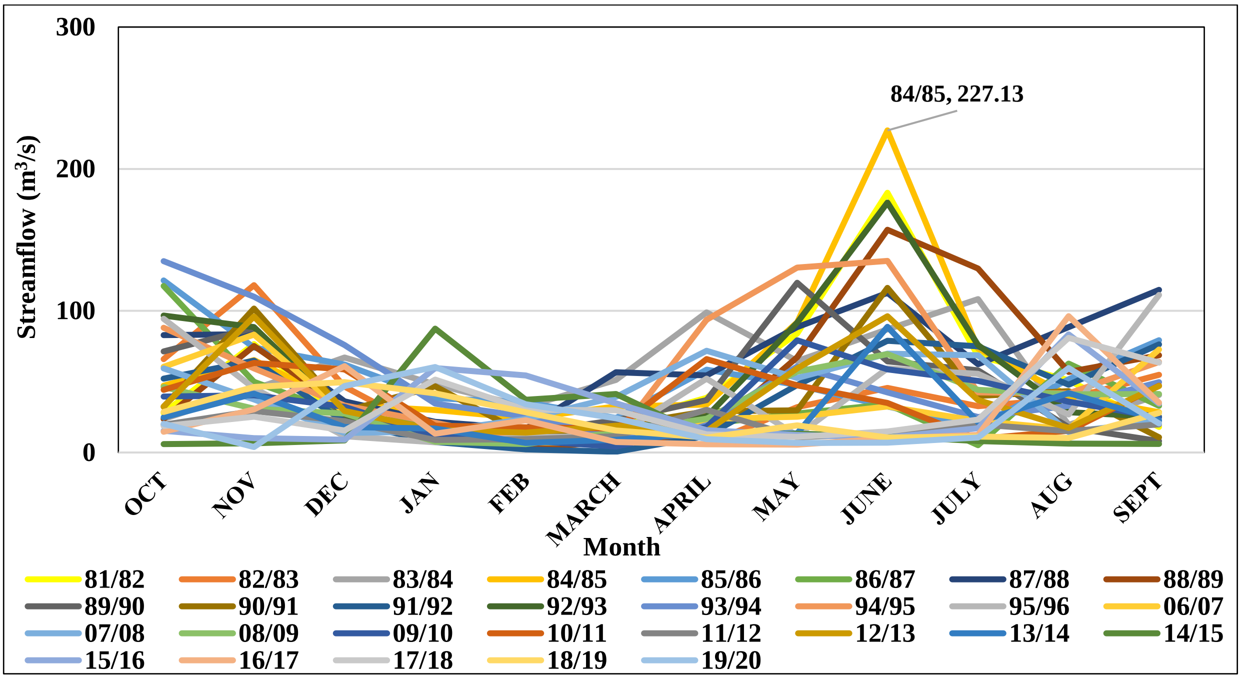

Figure 3-19: Average monthly streamflow at Ratnapura station (1981-1996 and 2006-2020)

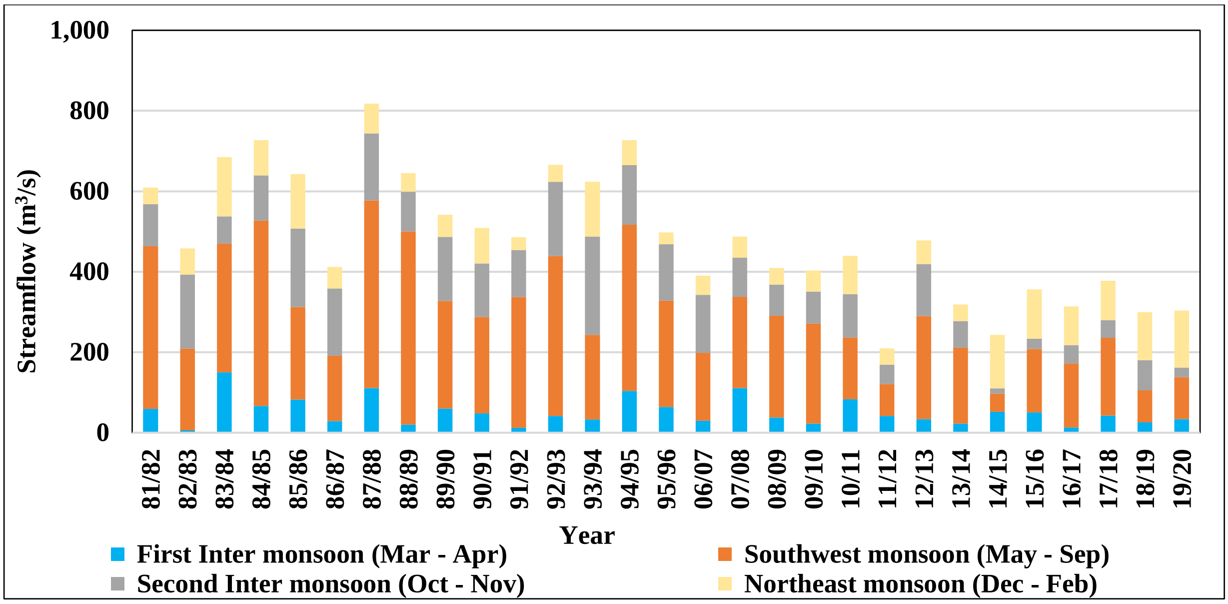

Figure 3-20: Seasonal variation of streamflow at Ratnapura station

Figure 3-20 represents the seasonal variation of streamflow in Ratnapura station. The maximum amount of streamflow is recorded during the South-west monsoon season.

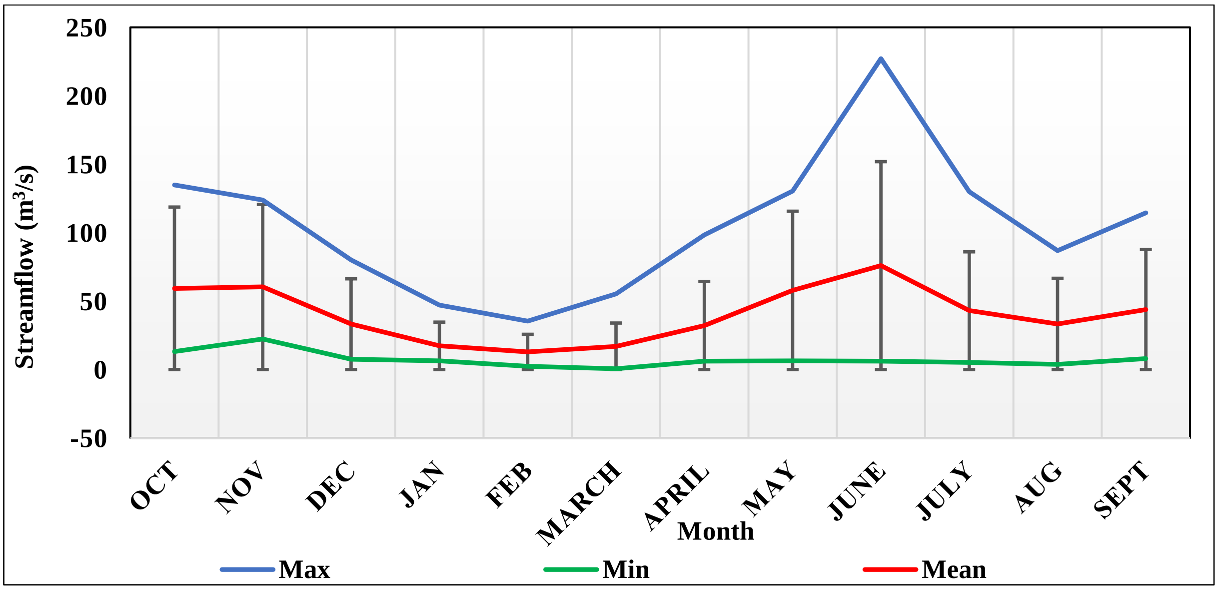

Figure 3-21: Maximum, minimum, and mean of the streamflow recorded at Ratnapura station

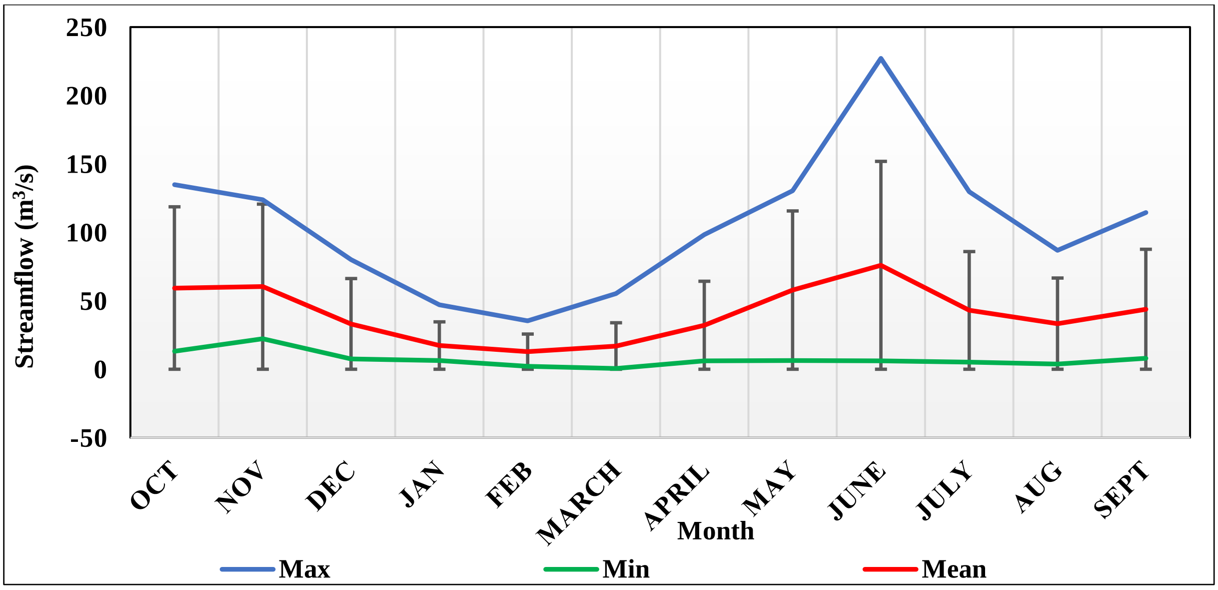

Figure 3-21: Maximum, minimum, and average Streamflow- Ratnapura station

Figure 3-22 represents the yearly variation of streamflow in the Putupaula gauging station. The highest streamflow recorded is about 2,500 m^3/s in the year 1994/95. The graph shows a decreasing trend from 1994-2017. Figure 3-23 represents the monthly variation of streamflow, where all the months show a similar trend but in August and September of 1994/95, it shows the highest streamflow of about 500 m^3/s.

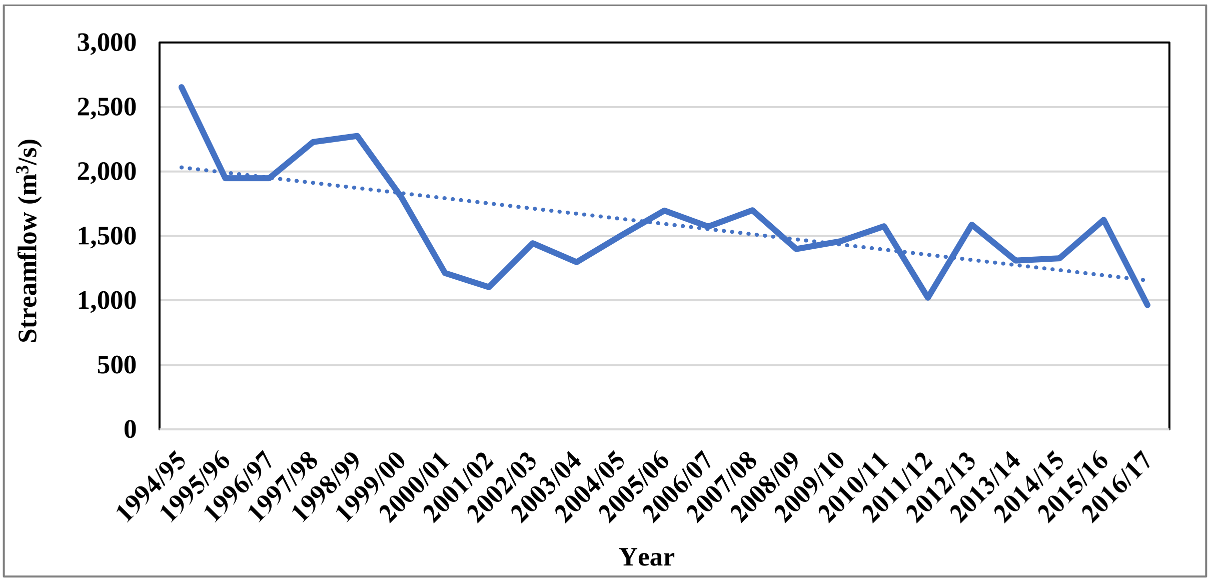

Figure 3-22: Annual total streamflow at Putupaula station

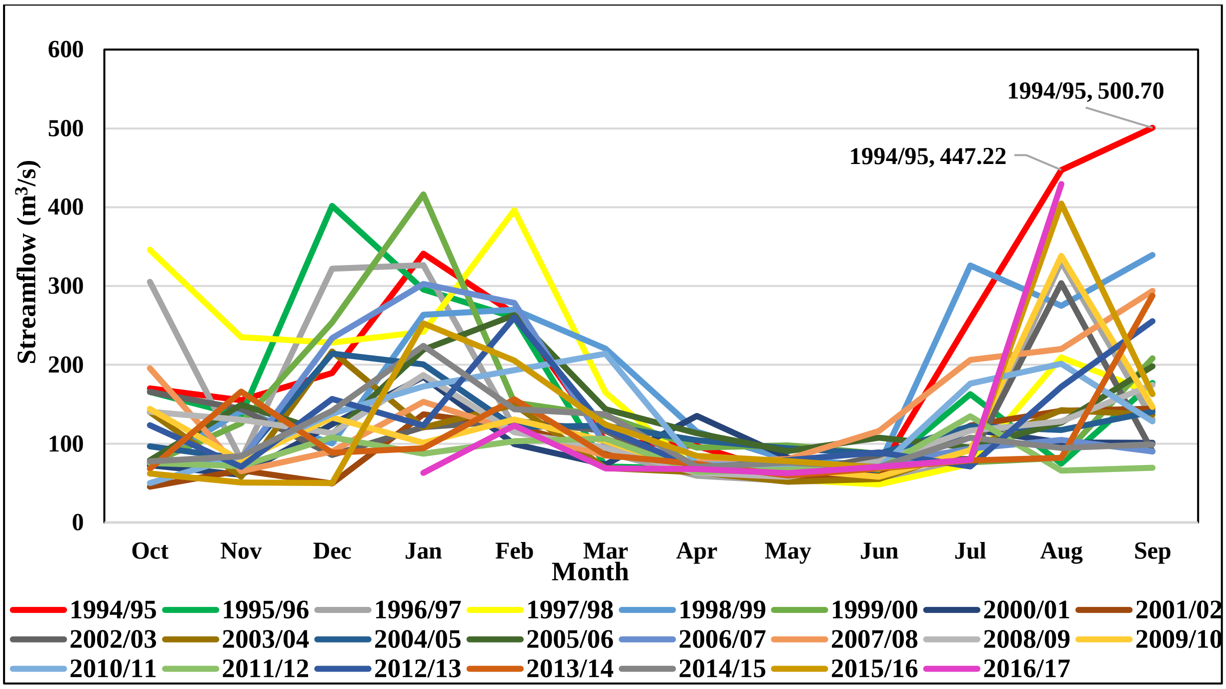

Figure 3-23: Average monthly streamflow at Putupaula station from 1994-2017

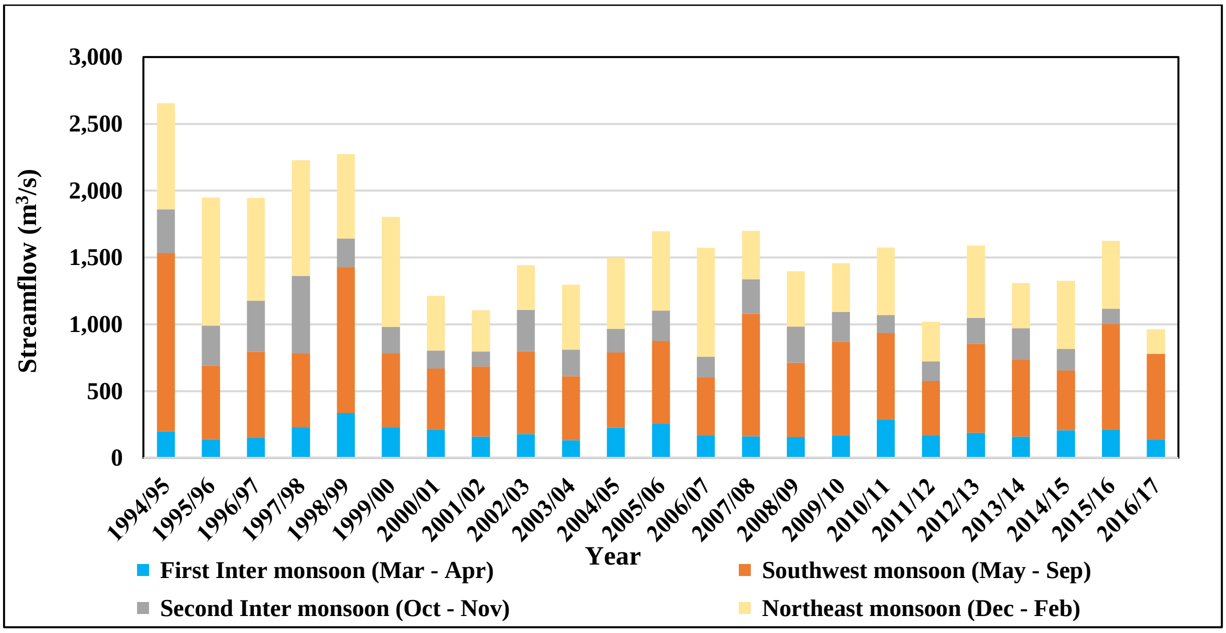

Figure 3-24: Seasonal variation of streamflow at Putupaula station

Figure 3-24 represents the seasonal variation of streamflow in the Putupaula station. The maximum amount of streamflow is recorded during the South-west monsoon season. Figure 3-25 represents the maximum, minimum, and mean of the streamflow recorded at Putupaula station.

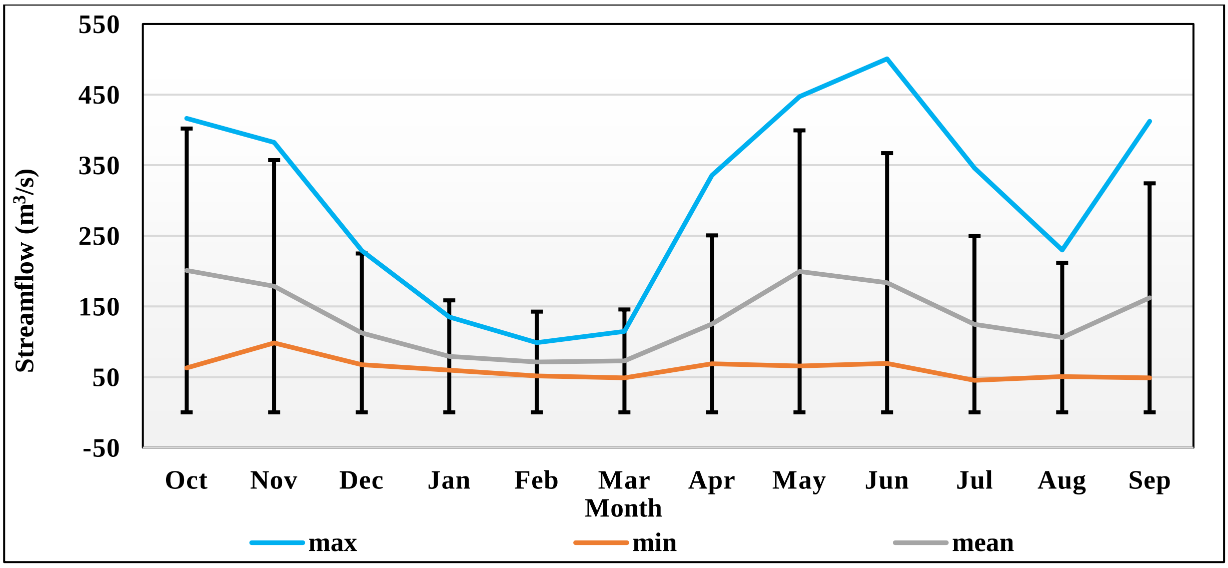

Figure 3-25: Maximum, minimum, and average streamflow- Putupaula station

3.3.7 Gumbel distribution method

Gumbel distribution is one of the most extensively used probability distribution functions for extreme values in hydrological and meteorological studies to predict flood peaks, maximum rainfall, maximum winds, etc. The potential applicability of the Gumbel distribution is to signify the distribution of maximum values related to extreme value theory which specifies that it is likely to be suitable for the distribution of the underlying sample data that is normal or exponential type.

For the study area, the yearly maximum rainfall values were taken and the Reduced variate (y_t) and flood value of recurrence interval in time period T, (x_t) were calculated and plotted in the graph (Subramanya, 2013). After plotting the rainfall data in a semi-log for Gumbel's distribution, it can be noticed that all stations are approximately following a straight line except for the USK Valley station. To verify the usage of the Gumbel method in this study, an effort was made to assess the streamflow distribution based on Gumbel's method and it can be noticed from Figure 3-27 that it follows a straight line. Therefore, the return periods were calculated and major events were selected for calibration and validation accordingly. Following Figure 3-26 represents the Gumbel distribution plotted for all rainfall gauging stations.

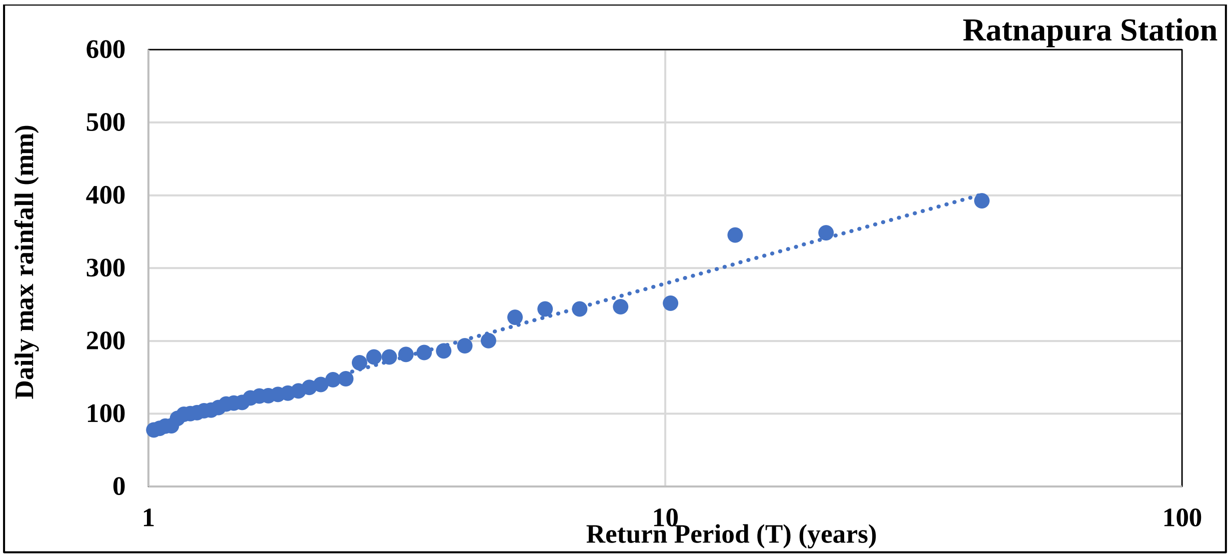
Ratnapura Station
Daily max rainfall (mm)
600
500
400
300
200
100
0
1
10
100
Return Period (T) (years)

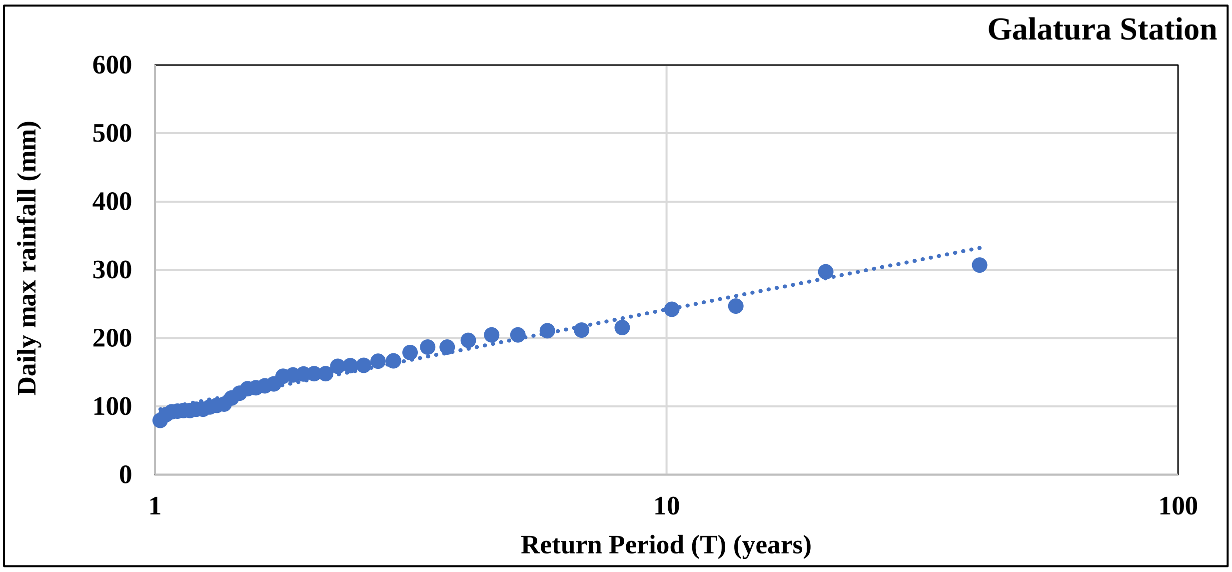
Galatura Station
Daily max rainfall (mm)
600
500
400
300
200
100
0
1
10
100
Return Period (T) (years)

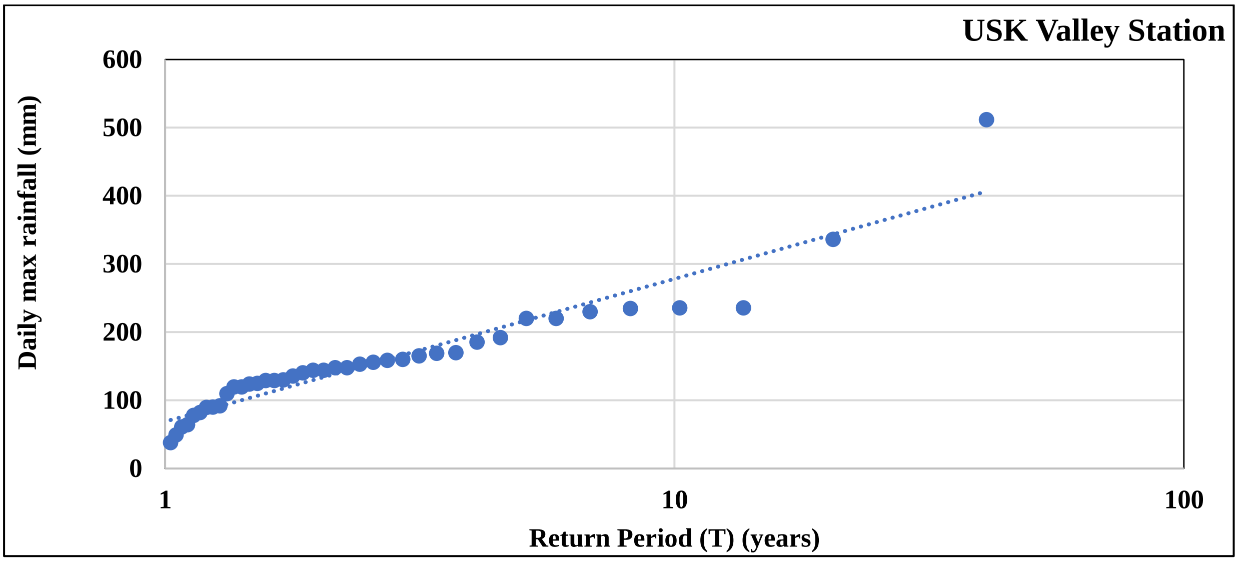
USK Valley Station
Daily max rainfall (mm)
600
500
400
300
200
100
0
1
10
100
Return Period (T) (years)

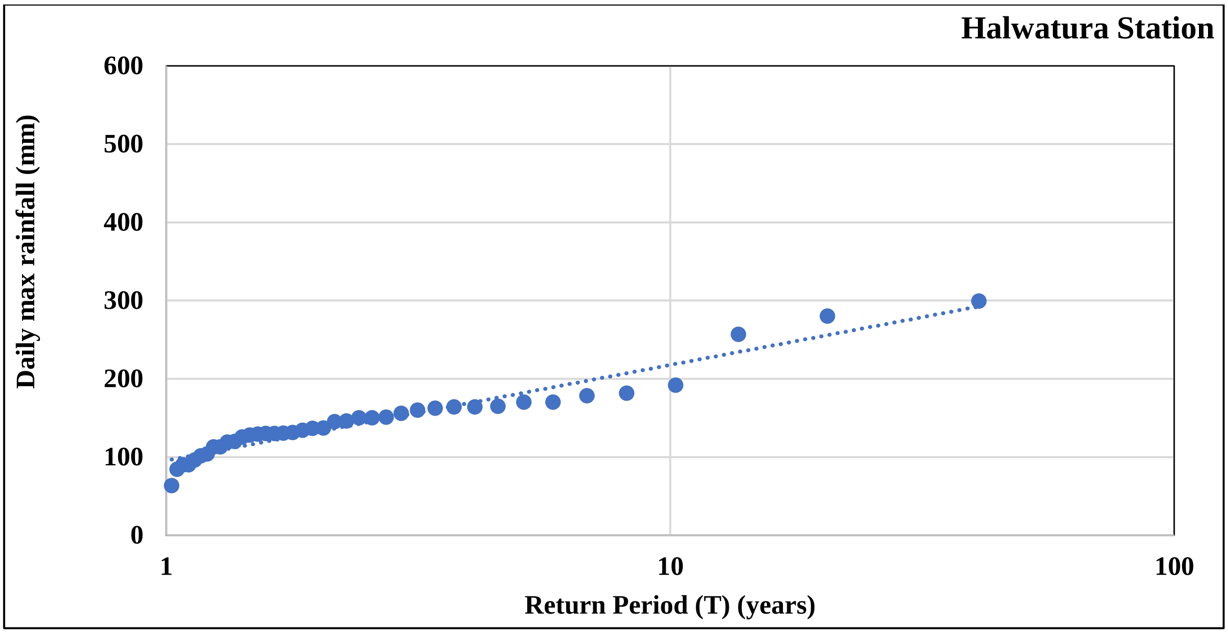

Figure 3-26: Gumbel distribution of all rainfall stations

Gumbel defined a flood as the largest of the 365 daily flows and the annual series of flood flows constitute a series of largest values of flows (Subramanya, 2013). According to this theory of extreme events, the probability of occurrence of an event is equal to or larger than a value x_o which is,

$$P(x \geq x_0) = 1 - e^{-e^{-y}} \qquad [3\text{-}2]$$

in which *y* is a dimensionless variable given by

$$y = \alpha(x - a);\ a = \bar{x} - 0.45005\,\sigma_x;\ \alpha = \frac{1.2825}{\sigma_x}$$

$$y = \frac{1.285(x - \bar{x})}{\sigma_x} + 0.577 \qquad [3\text{-}3]$$

where $\bar{x}$ = mean, σ_x = standard deviation of variate *x*. The value of *x* for a given *P* that is required is transposed as:

$$y_P = -\ln(-\ln(1 - P)) \qquad [3\text{-}4]$$

Thus, Return period, T = 1/P

y_T = value of *y* called reduced variate for a given *T*

$$y_T = -\left(l_n \cdot l_n \frac{T}{T-1}\right) \quad [3\text{-}5]$$

$$y_T = -\left(0.834 + 2.303 \log\log \frac{T}{T-1}\right) \quad [3\text{-}6]$$

Now rearranging the value of variate *x* with return period *T* is given by:

$$x_T = \bar{x} + k\sigma_x \quad [3\text{-}7]$$

The value of *k* is given by,

$$k = \frac{y_T - \overline{y_n}}{s_n} \quad [3\text{-}8]$$

For this study, $\overline{y_n}$ = reduced mean = 0.5926

s_n = reduced standard deviation = 1.0864

Table 3-3 represents the estimation of x_T for Putupaula streamflow station. The calculated return period along with the estimated peak discharge is shown in Table 3-4.

Table 3-3: Gumbel distribution of Putupaula streamflow station

Year	Max SF (m^3/day)	Max SF (m^3/sec)	Rank (M)	Recurrence Interval	Reduced variate (y_t)	Frequency factor (k)	Flood Discharge (x_t)
2017	2,316.37	0.026	1	25.00	3.199	2.457	1789.97
2008	1,355.63	0.015	2	12.50	2.484	1.799	1540.32
2003	1,082.48	0.012	3	8.33	2.057	1.406	1390.96
1999	1,054.54	0.012	4	6.25	1.747	1.120	1282.47
2014	1,003.48	0.011	5	5.00	1.500	0.893	1196.22
2016	996.77	0.011	6	4.17	1.293	0.703	1123.90
2010	958.94	0.011	7	3.57	1.113	0.537	1061.04
1998	899.81	0.010	8	3.13	0.953	0.390	1004.97
2000	851.73	0.009	9	2.78	0.807	0.255	953.93
1995	839.2	0.009	10	2.50	0.672	0.131	906.72
2005	831.73	0.009	11	2.27	0.545	0.014	862.44
1996	826.77	0.009	12	2.08	0.425	-0.097	820.39
1997	790.23	0.009	13	1.92	0.309	-0.203	780.03
2012	778.18	0.009	14	1.79	0.197	-0.306	740.87

Year	Max SF (m^3/day)	Max SF (m^3/sec)	Rank (M)	Recurrence Interval	Reduced variate (y_t)	Frequency factor (k)	Flood Discharge (x_t)
2004	709.21	0.008	15	1.67	0.087	-0.407	702.47
2011	699.13	0.008	16	1.56	-0.021	-0.507	664.43
2006	693.93	0.008	17	1.47	-0.131	-0.608	626.29
2007	670.61	0.007	18	1.39	-0.241	-0.710	587.55
2015	645.19	0.007	19	1.32	-0.356	-0.815	547.59
2009	590.85	0.006	20	1.25	-0.476	-0.926	505.57
2001	588.92	0.006	21	1.19	-0.606	-1.045	460.18
1994	540.72	0.006	22	1.14	-0.752	-1.179	409.21
2013	489.94	0.005	23	1.09	-0.927	-1.340	348.04
2002	354.56	0.004	24	1.04	-1.169	-1.564	263.28
Mean	857.04						
S.D.	379.75						

Table 3-4: Return period and flood discharge of Putupaula streamflow station

Sl No.	Return Period (T) (years)	Flood Discharge (x_t) (m^3/s)
1	2	800.0
2	5	1,196.2
3	10	1,458.5
4	15	1,606.5
5	20	1,710.2
6	25	1,790.0
7	50	2,035.9
8	100	2,279.9

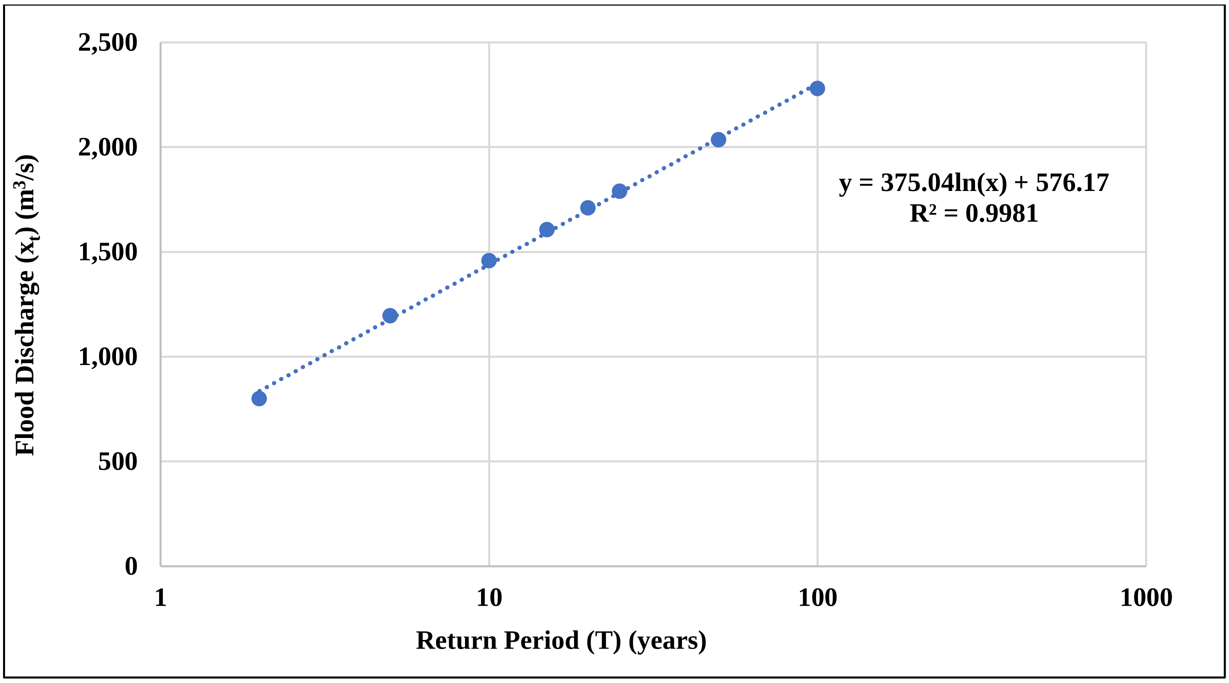

Figure 3-27: Return period and flood discharge using Gumbel distribution for Putupaula streamflow station

Figure 3-27 represents the return period along with the peak discharge estimated using the above equations. The line connecting the dots for return period and flood discharge is known as the curve fitting where it can capture the trend in the data by assigning a single function across the entire range. It is useful for determining the extreme values both maximum and minimum in a dataset and it rapid and straightforward method to apply to any data, relative to many other statistical methods (Javier & Alboreca, 2015). According to Subramanya, (2013) to verify whether a given dataset follows Gumbel distribution, the plot of X_t vs T on a convenient paper such as semi-log, log-log, or Gumbel probability paper should result in a straight line. Since in this study, the plot of X_t vs T follows a straight line which is shown in Figure 3-27. Therefore, it follows the Gumbel distribution and is used for event selection.

Using Gumbel's distribution, the value of variate for a given return period X_t determined, can have errors due to the limited sample data used, an estimate of the confidence limits is desirable. The confidence interval indicates the limits about the calculated value between which the true value can be said to lie with a specific probability based on sampling errors only. For confidence probability c, the confidence interval of the variate X_t is bounded by values x_1 and x_2 given by:

$$x_{1/2} = x_t \pm f(c)\ Se \qquad [3\text{-}9]$$

$$\text{Probable error, } Se = b\,\frac{\sigma_{n-1}}{\sqrt{N}} \qquad [3\text{-}10]$$

$$b = \sqrt{1 + 1.3k + 1.1k^2} \qquad [3\text{-}11]$$

where, σ_{n-1} = Standard deviation of the sample

k = Frequency factor given by Equation [3-8]

N = sample size

Table 3-5 shows the estimated confidence limits for the different return periods. For this study, 99 % confidence probability was considered for the selection of the flood events in the RRI model.

Table 3-5: Confidence limits for different return period

Return Period	b	Probable Error (Se)	99 % Confidence Probability (X1)	99 % Confidence Probability (X2)	95 % Confidence Probability (X1)	95 % Confidence Probability (X2)	90 % Confidence Probability (X1)	90 % Confidence Probability (X2)
2	0.9	70.6	997.7	602.3	938.4	661.6	916.2	683.9
5	1.7	135.1	1,574.6	817.9	1,461.1	931.4	1,418.5	973.9
10	2.4	187.0	1,982.1	935.0	1,825.0	1,092.0	1,766.1	1,150.9
15	2.8	217.2	2,214.7	998.4	2,032.2	1,180.8	1,963.8	1,249.3
20	3.1	238.6	2,378.2	1,042.2	2,177.8	1,242.6	2,102.6	1,317.7
25	3.3	255.1	2,504.3	1,075.6	2,290.0	1,289.9	2,209.7	1,370.3
50	4.0	306.5	2,894.1	1,177.6	2,636.6	1,435.1	2,540.1	1,531.6
100	4.6	357.9	3,281.9	1,277.9	2,981.3	1,578.5	2,868.6	1,691.2

3.3.8 Identification of floodplain areas

The floodplain areas are identified using the Flood extent map of Sri Lanka from the website using Synthetic Aperture Radar (SAR) of 250 m resolution conducted by National Aeronautics and Space Administration- Jet Propulsion Laboratory (NASA JPL), where main channel and secondary channel sections were identified in the Kalu Ganga Basin (Priority Index Sri Lanka Floods, 2017), shown in Figure 3-31 and Figure 3-31, respectively (Edirisooriya, 2018).

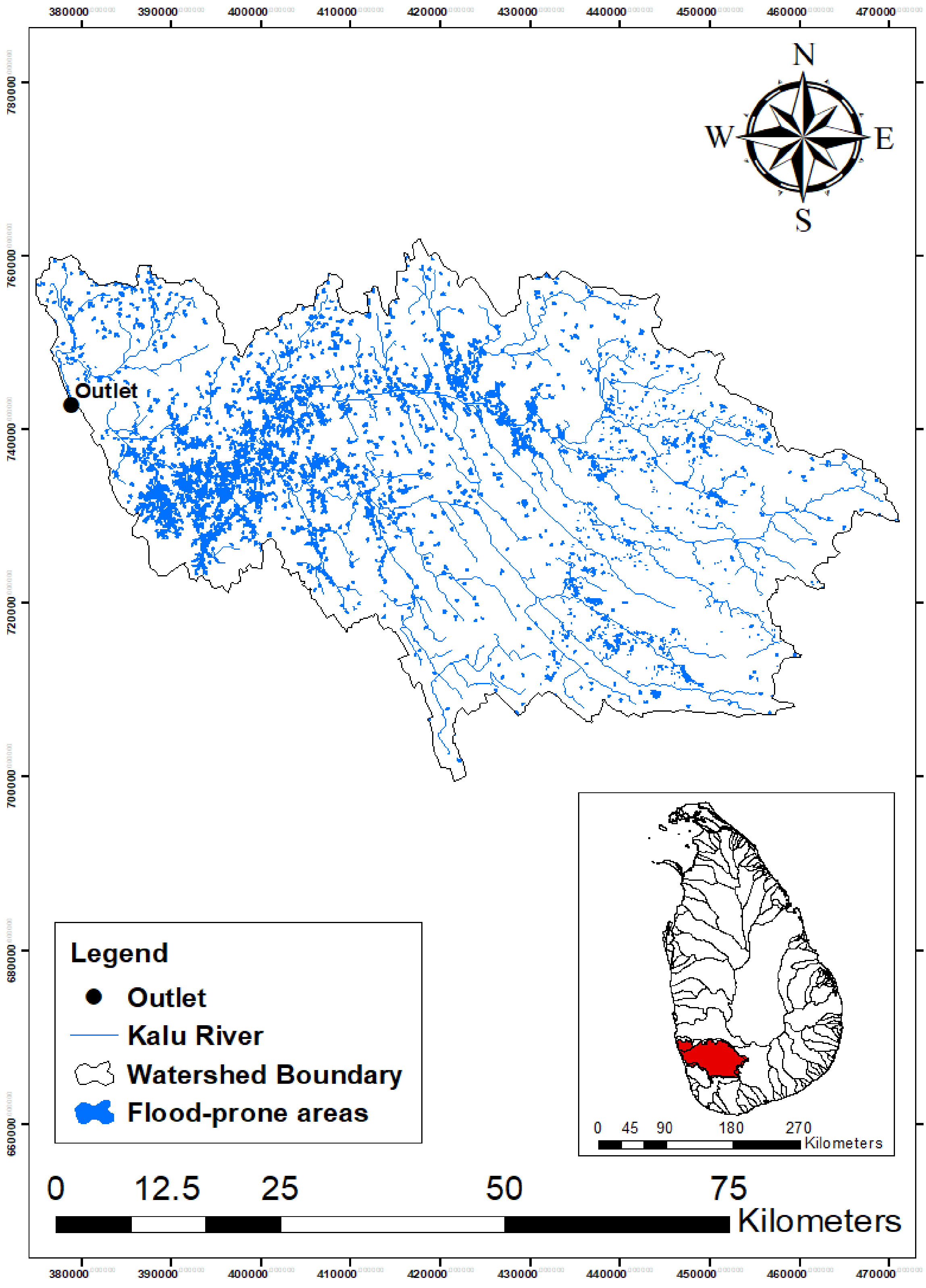

Figure 3-28: Flood-prone areas in the Kalu Ganga basin

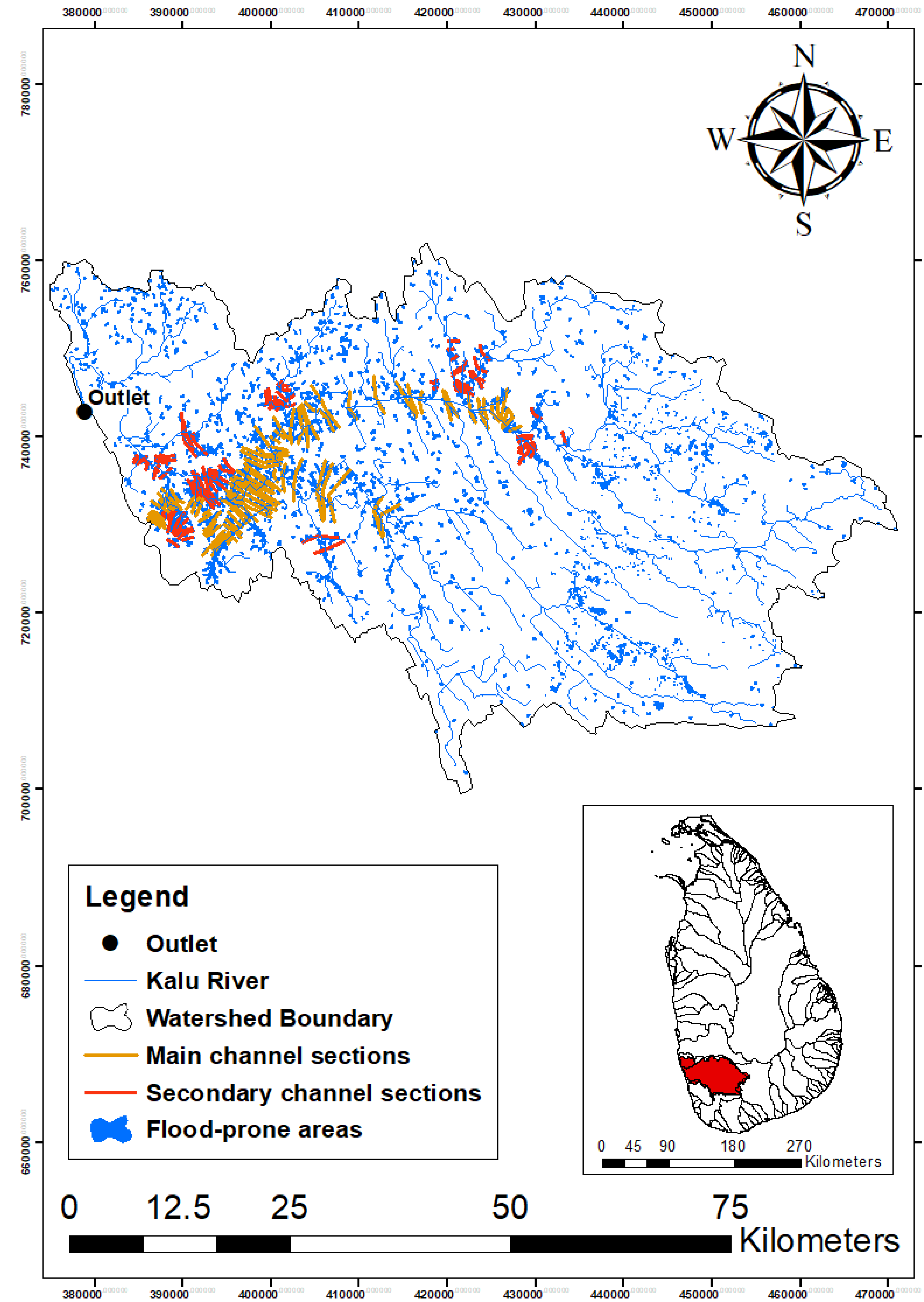

Figure 3-29: Floodplain sections in the Kalu Ganga basin

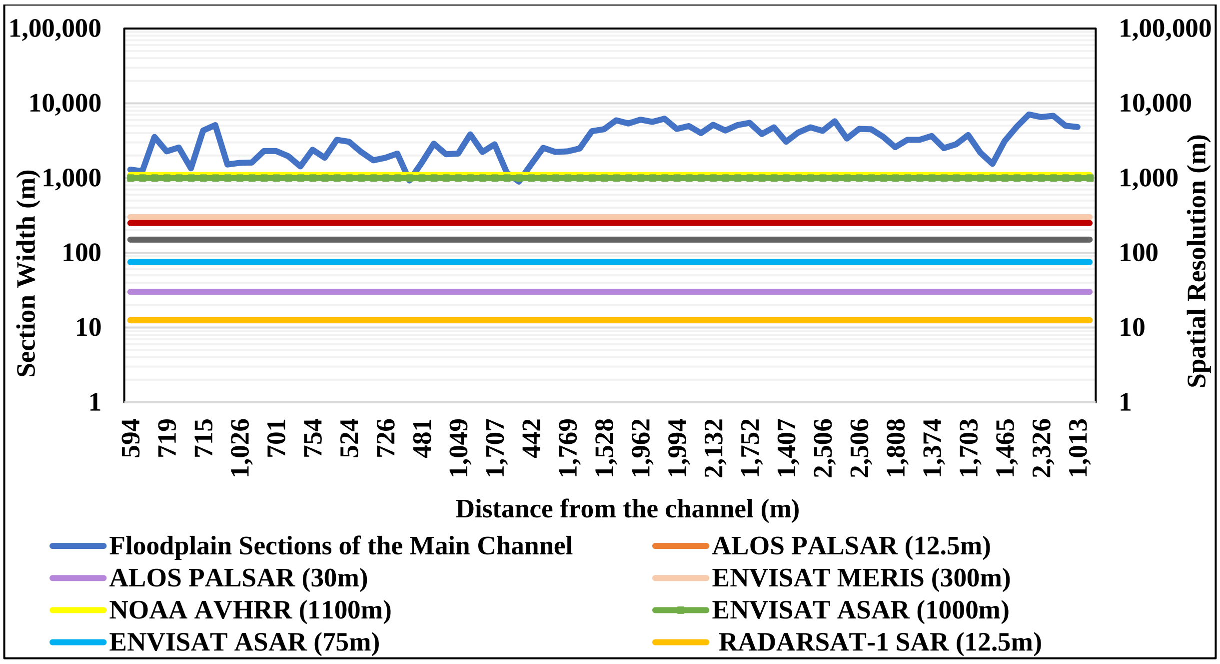

Figure 3-30: Floodplain sections of the main channel of the Kalu Ganga basin along with the spatial resolution of various satellite data

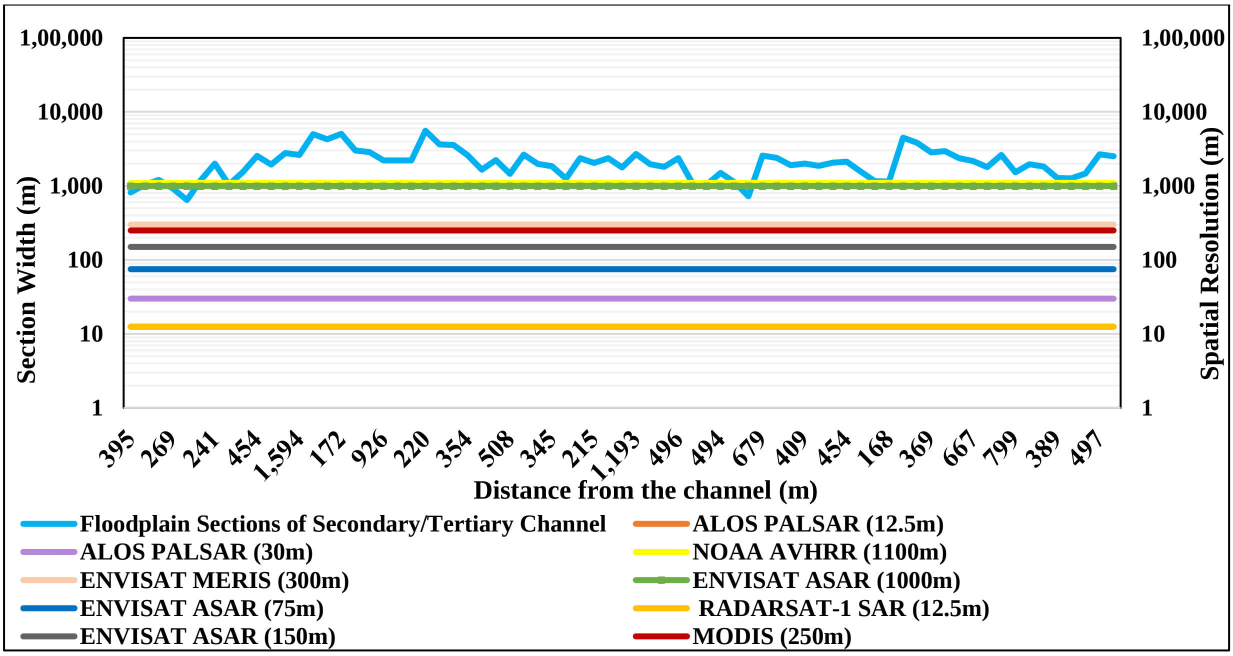

Figure 3-31: Floodplain sections of secondary/tertiary channels of the Kalu Ganga basin along with the spatial resolution of various satellite data

Figure 3-31 and Figure 3-32 show the graphical representation of the floodplain section width of the main channel and secondary/tertiary channel, respectively along with the spatial resolution of various satellite data and the distance of the floodplain section from the channel.

The floodplain sections were taken where the flood extent was more. Main channel sections and secondary/ tertiary channel sections were classified and different graphs were plotted for the distance from the channel, respectively. The graph shows that most of the satellite data covers all the section width of the basin. Therefore, for Kalu Ganga using ALOS PALSAR (12.5 m, 30 m) and RADARSAT-1 SAR (12.5 m) satellite data will be accurate enough to detect and analyze all floodplain areas in the basin.

CHAPTER 4

4 MODEL DEVELOPMENT AND APPLICATIONS

4.1 RRI Model Application

The Rainfall-Runoff-Inundation (RRI) model is developed by Dr. Takahiro Sayama (Sayama et al., 2011) and has been used in many event-based flood evaluations studies. The RRI model uses flood applications with two-dimensional diffusion-wave equations to estimate water depths in each orthogonal grid cell and instantaneously incorporate the procedures of rainfall, runoff, and the propagation of flood inundation (Fattah et al., 2018; Rasmy et al., 2019). The 2D model moreover simulates vertical infiltration and saturated subsurface flow in hilly areas using the Green-Ampt model and saturated subsurface flow in the hilly areas. The Green-Ampt model is a method that assumes the soil is fully saturated and has uniform conductivity to whatever depth the infiltrating water has penetrated the soil under the conditions of ponding (Yoshimoto & Amarnath, 2017). The flow within a river channel can be calculated using the 1D diffusive wave model built-in, whose lateral influx and outflow, often known as overbank flow, are calculated by combining with the two-dimensional land model The river's interaction with the flow at each time step, the channel and slope are predicted depending on the water level, multiple overflowing formulae exist and levee height conditions (Sayama et al., 2011).

4.1.1 Overview of the model structure

The RRI model can estimate rainfall-runoff and flood inundation simultaneously and with river channels and slopes separately (Sayama, 2012). For every grid cell with a river channel, the model assumes that both the slope and the river are in the same grid cell. The channels are discretized as a single vector along the centerline of the overlying slope grid cell. Channels represent an additional flow path between grid cells lying over the actual river course. Lateral flows are estimated in a slope cell on a 2D basis. There are two depths in the slope grid cell of the river channel. One is for waterways and the other is for the slope (or floodplain) itself. Slope and river inflow-outflow interactions are estimated based on different overflow equations depending on water level and embankment height conditions. Figure 4-1 shows the schematic diagram of the rainfall-runoff–inundation (RRI) model, where the input given was rainfall, DEM, land cover, and cross-section, and the outputs obtained are discharge, water level, and inundation areas (Sayama et al., 2011).

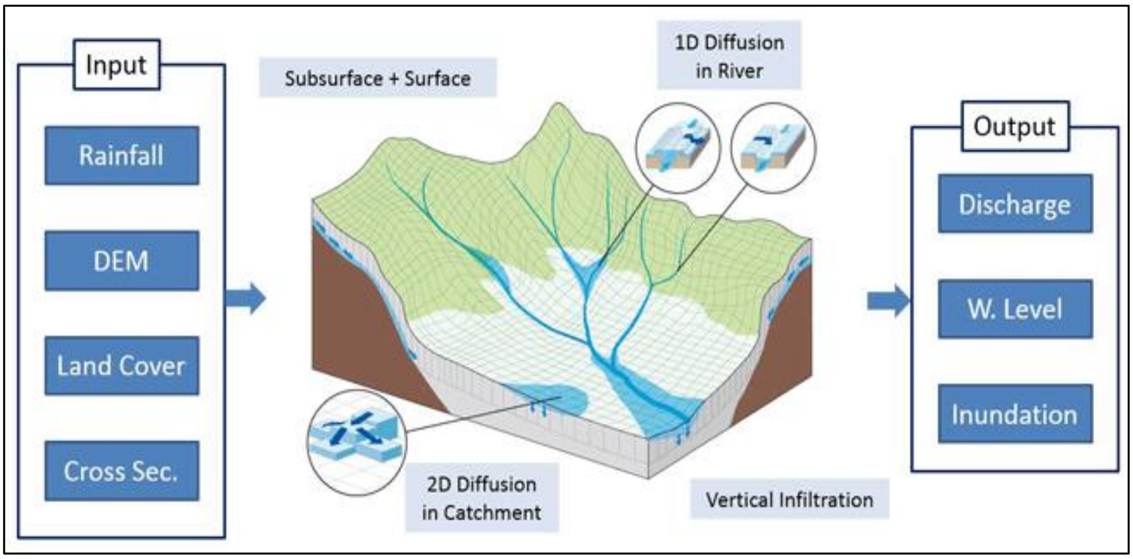

Figure 4-1: Schematic diagram of the rainfall-runoff–inundation (RRI) model

4.1.2 Two-dimensional surface and subsurface flow model

To estimate lateral flows on slope grid cells, in the RRI model, it can be considered as “a storing cell-based flood model” (Hunter, 2005). To calculate lateral flows on slope grid cells, in the RRI model, it can be characterized as “a storage cell-based inundation model” (Hunter, 2005). The model equations are derived based on the following mass balance from Equation [4-1] and momentum Equation [4-2] for gradually varied unsteady flow:

$$\frac{\partial h}{\partial t} + \frac{\partial q_x}{\gamma x} + \frac{\partial q_y}{\partial y} = r \qquad [4\text{-}1]$$

$$\frac{\partial q_x}{\partial t} + \frac{\partial u q_x}{\partial x} + \frac{\partial v q_x}{\partial x} = -gh\frac{\partial H}{\partial x} - \frac{\tau_x}{\rho_w} \qquad [4\text{-}2]$$

$$\frac{\partial_{q_y}}{\partial t}+\frac{\partial u q_y}{\partial y}+\frac{\partial v q_y}{\partial y}=-gh\frac{\partial H}{\partial Y}-\frac{\tau_y}{\rho_w} \quad [4\text{-}2]$$

where h is the height of the water from the local surface, q_x and q_y are the unit width discharges in x and y directions, u and v are the flow velocities in x and y directions, r is the rainfall intensity, H is the height of the water from the datum, ρ_w is the density of water, g is the gravitational acceleration, and τ_x and τ_y are the shear stress in x and y directions. The second terms of the right-hand side of equations [4-3] and [4-4] are calculated with Manning's equation:

$$\frac{\tau_x}{\rho_w}=\frac{gn^2u\sqrt{u^2+v^2}}{h^{1/3}} \quad [4\text{-}3]$$

$$\frac{\tau_x}{\rho_w}=\frac{gn^2v\sqrt{u^2+v^2}}{h^{1/3}} \quad [4\text{-}4]$$

where n is Manning's roughness parameter. Under the diffusion wave approximation, inertia terms are neglected. Moreover, by separating x and y directions (i.e., ignoring v and u terms in Equations [4-3] and [4-4], respectively), the following equations are derived:

$$q_x=-\frac{1}{n}h^{5/3}\sqrt{\left|\frac{\partial H}{\partial x}\right|}\,\mathrm{sgn}\left(\frac{\partial H}{\partial x}\right) \quad [4\text{-}5]$$

$$q_y=-\frac{1}{n}h^{5/3}\sqrt{\left|\frac{\partial H}{\partial x}\right|}\,\mathrm{sgn}\left(\frac{\partial H}{\partial y}\right) \quad [4\text{-}6]$$

where *sgn* is the signum function.

The RRI model spatially discretizes mass balance Equation [4-1]] as follows:

$$\frac{dh^{i,j}}{dt}+\frac{q_x^{i,j-1}\quad-1-q_x^{i,j}}{\Delta x}+\frac{q_y^{i-1,j}-q_y^{i,j}}{\Delta y}=r^{i,j} \quad [4\text{-}7]$$

where $q_x^{i,j}$, $q_y^{i,j}$ are x and y-direction discharges froma grid cell at (i, j).

By combining Equation [4-5], [4-6], and [4-7], water depths and discharges are calculated at each grid cell for each time step. A significant difference between the RRI model and other flood models is that RRI uses different types of runoff and hydraulic gradient relationships, so the same algorithm can be used to run both subsurface and subsurface flows simultaneously. The RRI model replaces these equations with Equations [4-8] and [4-9]. The first parts of Equations [4-8], and [4-9] describes the saturated subsurface flow based on Darcy's law, while the second parts describe the combination of the saturated subsurface flow and the surface flow:

$$q_x = \begin{cases} -kh\frac{\partial H}{\partial x} \\ -\frac{1}{n}(n-d)^{5/3}\sqrt{\left|\frac{\partial H}{\partial x}\right|}\ \mathrm{sgn}\left(\frac{\partial \varkappa}{0x}\right) - k(h-d)\frac{\partial H}{\partial x} \end{cases} \quad [4\text{-}8]$$

$$q_y = \begin{cases} -kh\frac{\partial H}{\partial y} \\ -\frac{1}{n}(n-d)^{5/3}\sqrt{\left|\frac{\partial H}{\partial y}\right|}\ \mathrm{sgn}\left(\frac{\partial \varkappa}{0y}\right) - k(h-d)\frac{\partial H}{\partial y} \end{cases} \quad [4\text{-}9]$$

where k is the lateral saturated hydraulic conductivityand d is the soil depth times the effective porosity. Equations [4-8] and [4-9] represent when ($h \leq d$) and ($d<h$). Using diffusion wave approximation streamflow was moreover calculated. The form of streamflow equations was essentially the same as Equations [4-5], and [4-7] but one-dimensional (q_y = 0). The shape of the channel was assumed to be a rectangle, whose geometries were defined with three parameters, width, depth, and levee height.

A simple infiltration component module is added based on the Green-Ampt infiltration model (Rawls, 1992):

$$f = k_v\left[1 + \frac{(\phi - \theta_1)s_f}{F}\right] \quad [4\text{-}10]$$

where f is the infiltration rate, k_v is the vertical saturated hydraulic conductivity, φ is the soil porosity, θ_i is the initial water volume content, S_f is the suction at the vertical wetting front and F is the cumulative infiltration depth (Sayama, 2012).

The RRI model uses flow direction and flow accumulation information only for identifying river channels but not for flood routing since the flow direction differs, depending on water levels. The river depths D (m) and widths W (m) were estimated by the following equation:

$$W = C_w A^{S_w} \quad [4\text{-}11]$$

$$D = C_D A^{S_D} \quad [4\text{-}12]$$

where A is upstream contributing area (km^2). The obtained parameters were obtained from (Rasmy et al., 2019): C_W = 6.5, S_W = 0.35, C_D = 0.8 and S_D = 0.25.

4.2 Model Setup and Development

The Rainfall-runoff-inundation model is used for this study area. The model is set up to run for the 2008 flood event to check the accuracy of the DEM used in the study area and verify the flood extent of the model with the Flood extent map of Sri Lanka (2017). For the input rainfall data, the 1st row represents the number of gauging stations taken along with the latitude and longitude of all the stations. From the 4th row, the data is written in the format of yy/mm/dd/hr, and all the precipitation values are written as in Table 4-1.

Table 4-1: Input data- observed rainfall data for 2008 flood event

4	Ratnapura (mm)	Galatura (mm)	USK Valley (mm)	Halwatura (mm)
Lat (°N)	6.68	6.70	6.57	6.72
Lon (°E)	80.40	80.28	80.20	80.20
2008/05/22 00:00	20.70	92.00	0.00	4.00
2008/05/23 00:00	3.20	27.00	36.30	3.20
2008/05/24 00:00	0.00	23.00	10.00	0.00
2008/05/25 00:00	0.70	17.00	0.00	0.00
2008/05/26 00:00	3.10	15.00	0.00	2.10
2008/05/27 00:00	9.30	85.00	27.50	7.00
2008/05/28 00:00	64.30	27.50	60.20	8.00
2008/05/29 00:00	20.70	32.00	78.50	19.00
2008/05/30 00:00	148.10	144.00	235.00	20.00
2008/05/31 00:00	110.20	110.00	206.00	14.00
2008/06/01 00:00	57.60	48.00	150.00	42.10
2008/06/02 00:00	48.60	120.00	135.60	28.00
2008/06/03 00:00	6.00	24.00	120.40	16.00
2008/06/04 00:00	3.50	10.00	110.60	0.00
2008/06/05 00:00	0.90	0.00	2.30	0.00
2008/06/06 00:00	31.40	23.00	3.10	73.00
2008/06/07 00:00	3.60	16.00	37.70	4.00
2008/06/08 00:00	30.80	8.00	42.20	14.00
2008/06/09 00:00	8.40	3.50	21.30	11.00

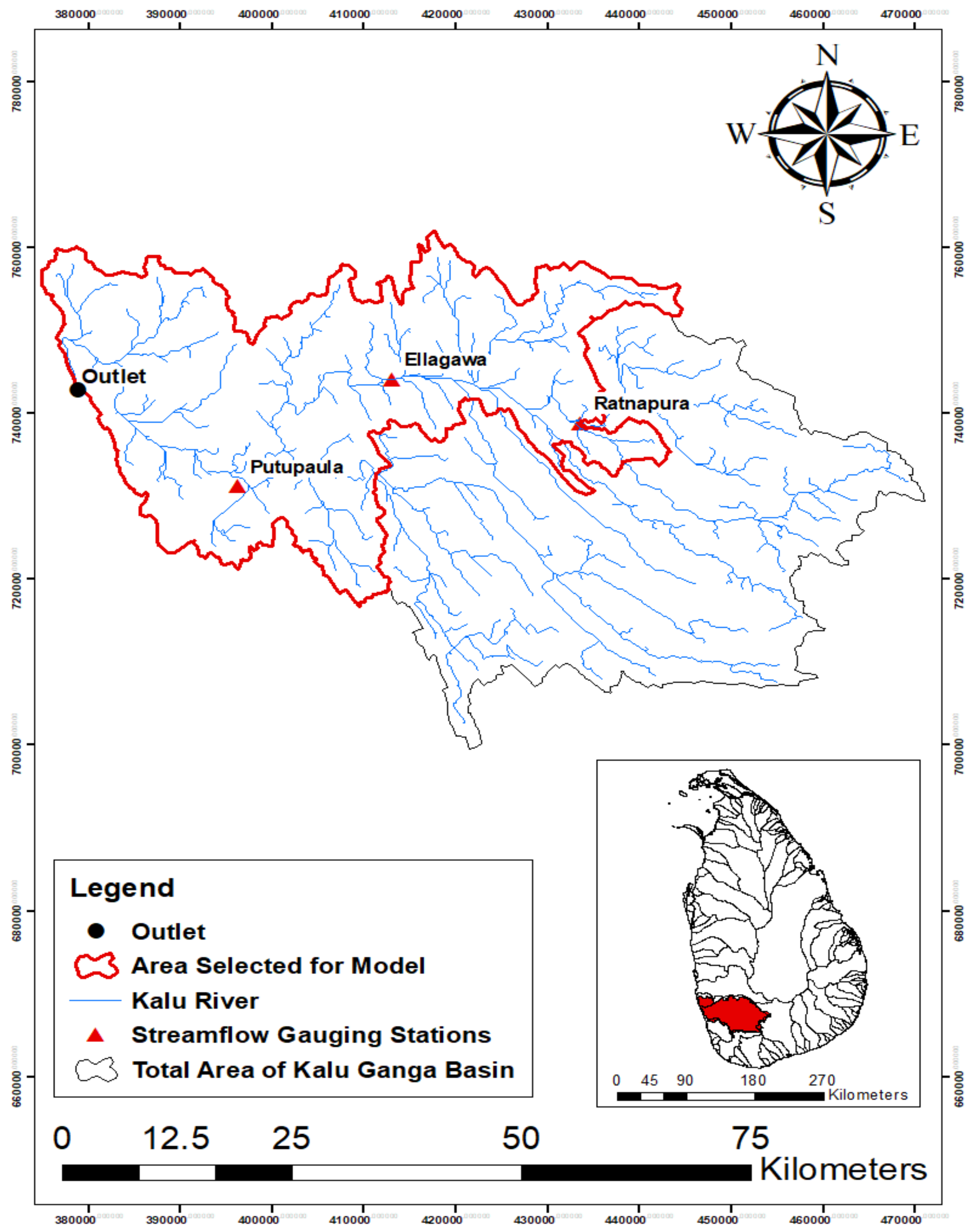

Figure 4-2: Area selected for RRI model

Figure 4-2 represents the area selected for the model, which has an area of about 1,526 km^2. The area selected for the model is taken from the Ratnapura station as the upstream boundary point to the outlet near the sea in Kalutara. Putupaula streamflow gauging station will be considered for the calibration and verification of the RRI model.

Following are the input data provided in the model shown in Figure 4-3, Figure 4-5, Figure 4-6, Figure 4-7, Figure 4-8, Figure 4-9, and Figure 4-9.

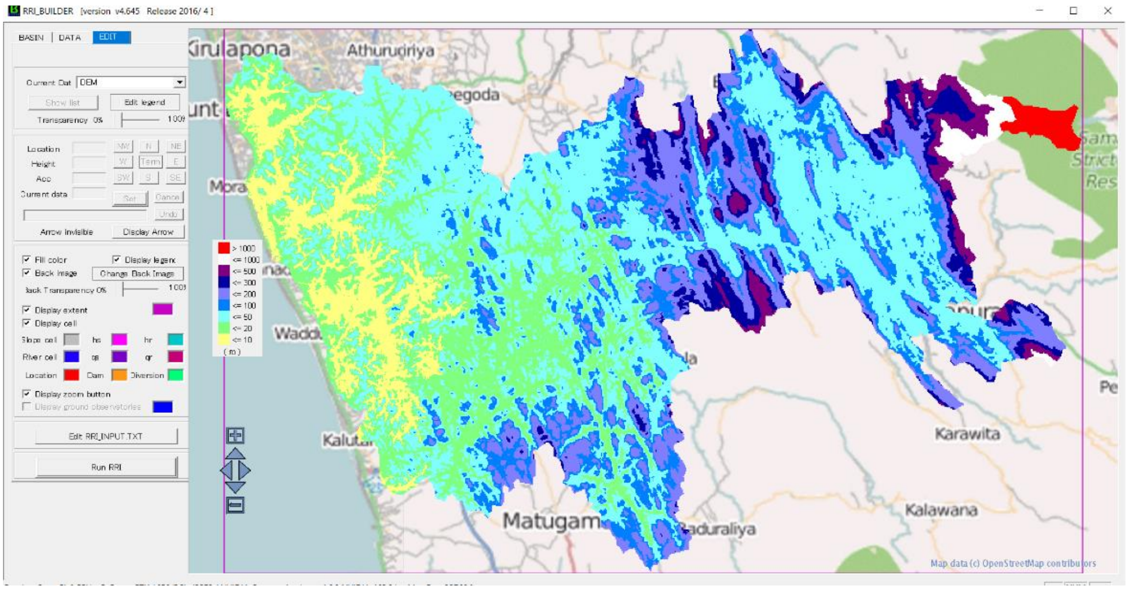

Figure 4-3: Digital Elevation Model of the study area

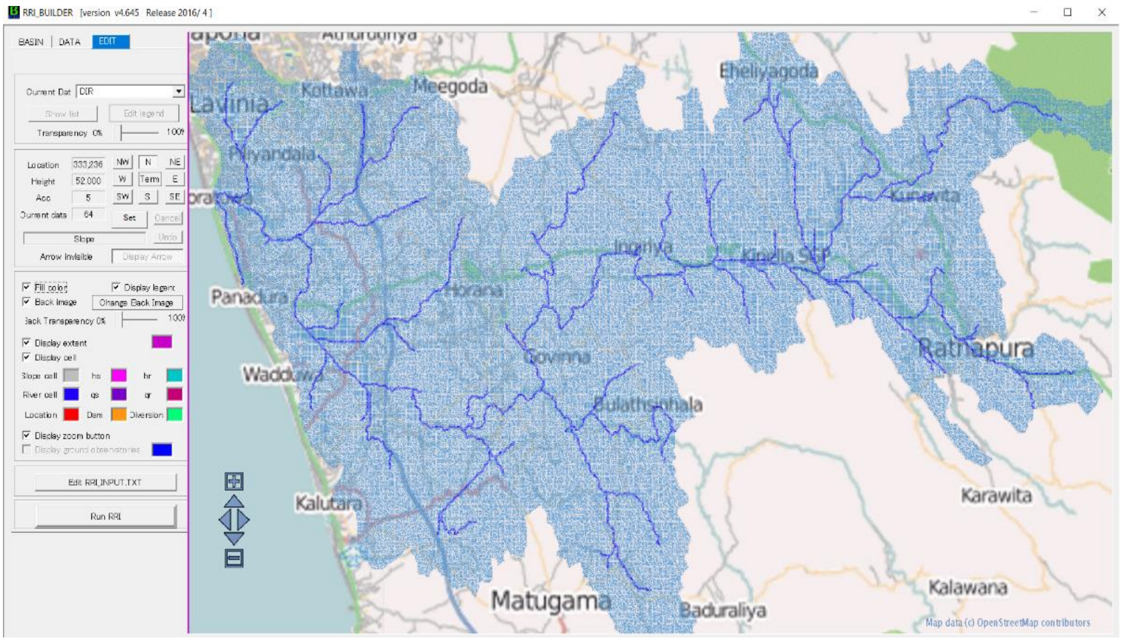

Figure 4-4: Flow direction of the study area

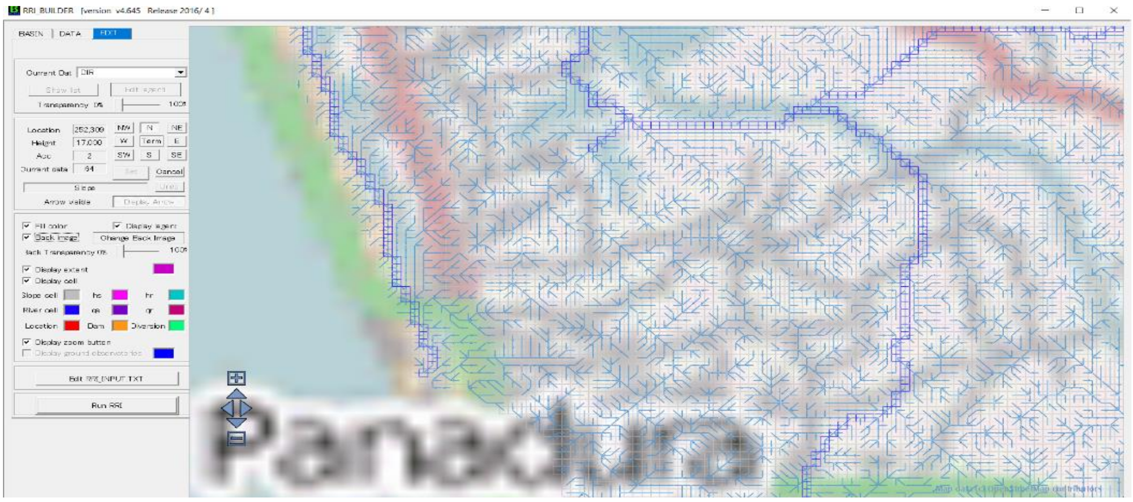

Figure 4-5: Zoomed view of flow direction near the outlet of the study area

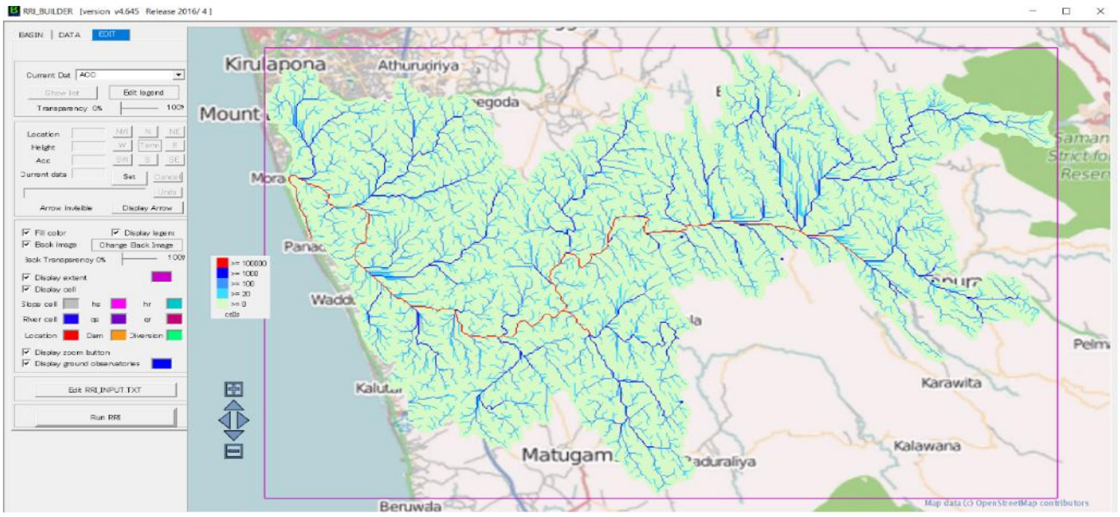

Figure 4-6: Flow accumulation of the study area

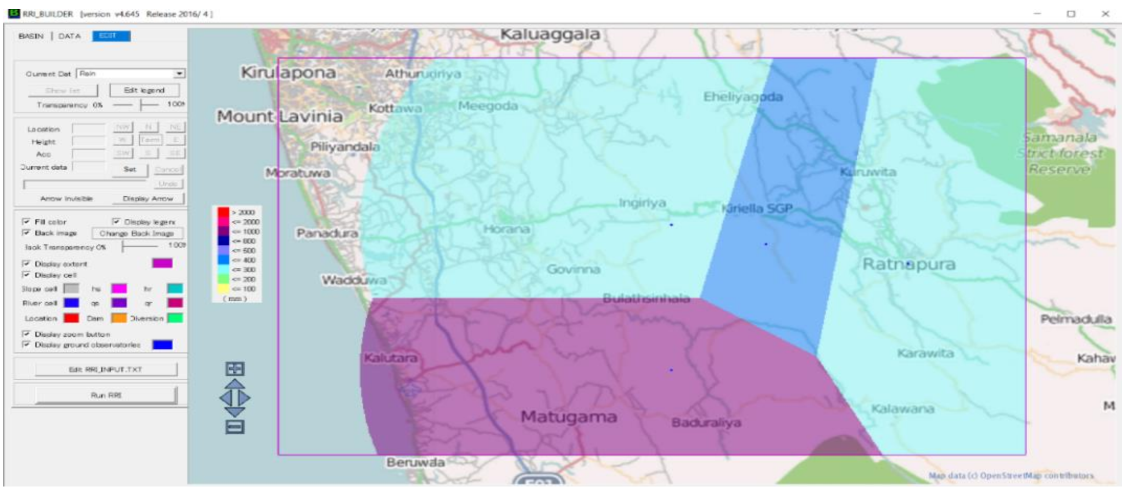

Figure 4-7: Thiessen polygon map of the study area

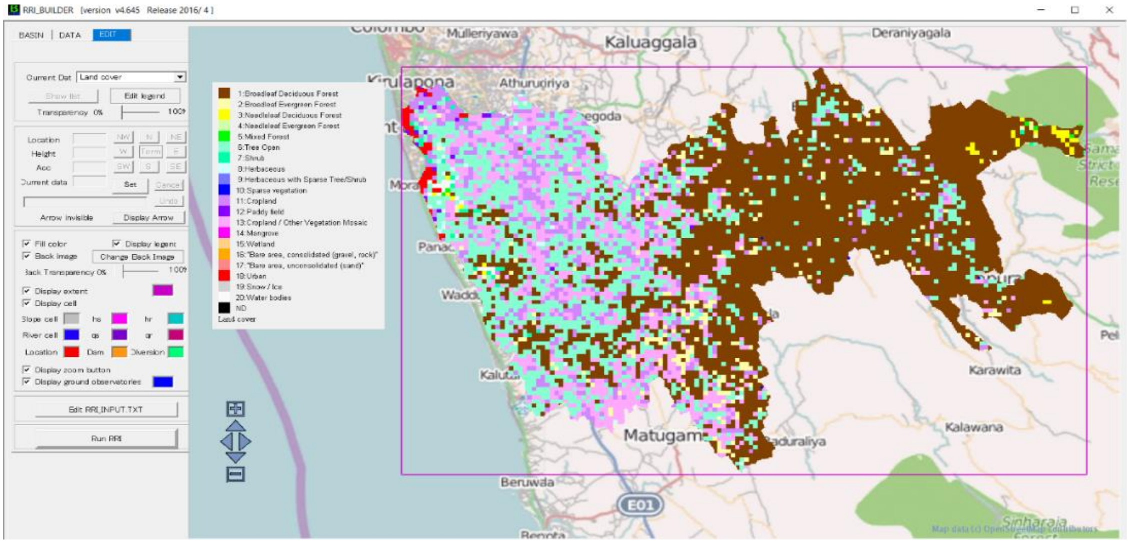

Figure 4-8: Landuse of the study area *[Source: Global Land Cover Characterization provided by USGS]*

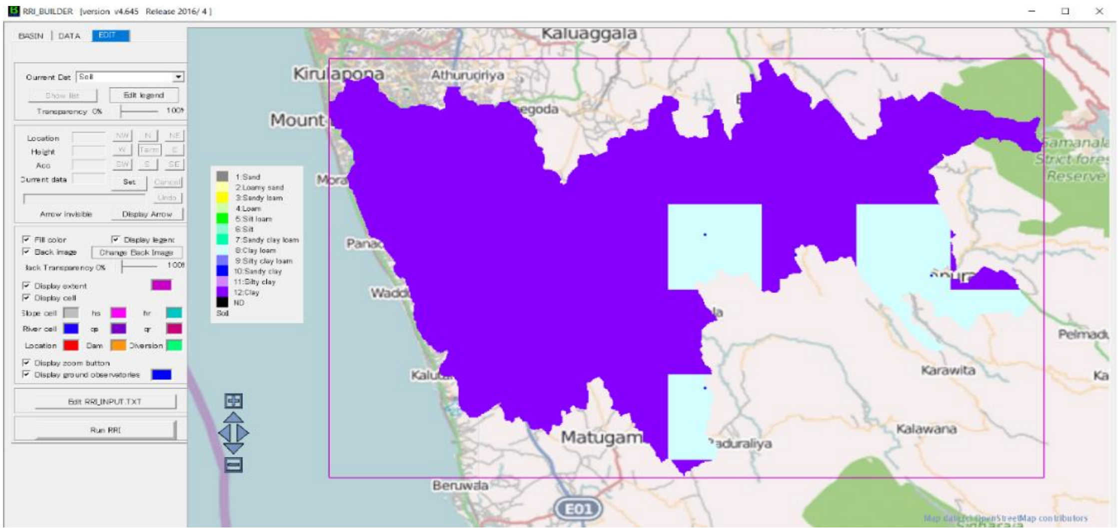

Figure 4-9: Soil cover of the study area *[Source: Global Land Cover Characterization provided by USGS]*

The 2008 flood event was selected for calibrating the model. After the development of the model, initial water depth (*hr* initial) and discharge boundary condition (*Qr*) was given from the Ratnapura streamflow station, which is taken as the upstream point. The output extracted from the model is converted in raster format from ASCII format in ArcGIS 10.5 software. Table 4-1 and Table 4-2 shows the input data given in the RRI model.

Table 4-2: Initial boundary condition for RRI model

Sl No.	Date	Boundary condition (Ratnapura Station) (m^3/s)
1	2008-05-22	37.66
2	2008-05-23	57.97
3	2008-05-24	31.93
4	2008-05-25	17.03
5	2008-05-26	14.70
6	2008-05-27	25.61
7	2008-05-28	27.84
8	2008-05-29	119.78
9	2008-05-30	84.15
10	2008-05-31	328.79
11	2008-06-01	361.41
12	2008-06-02	319.45
13	2008-06-03	291.35
14	2008-06-04	224.64
15	2008-06-05	134.11
16	2008-06-06	56.67
17	2008-06-07	43.74
18	2008-06-08	36.51
19	2008-06-09	41.79

Figure 4-10 represents the dataset for the 2008 flood event, where the rainfall data of the four gauging stations were plotted along with the streamflow data from Ratnapura and Putupaula station. The highest streamflow recorded was found to be 1,355.63 m^3/s and 361.41 m^3/s for Putupaula and Ratnapura station, respectively.

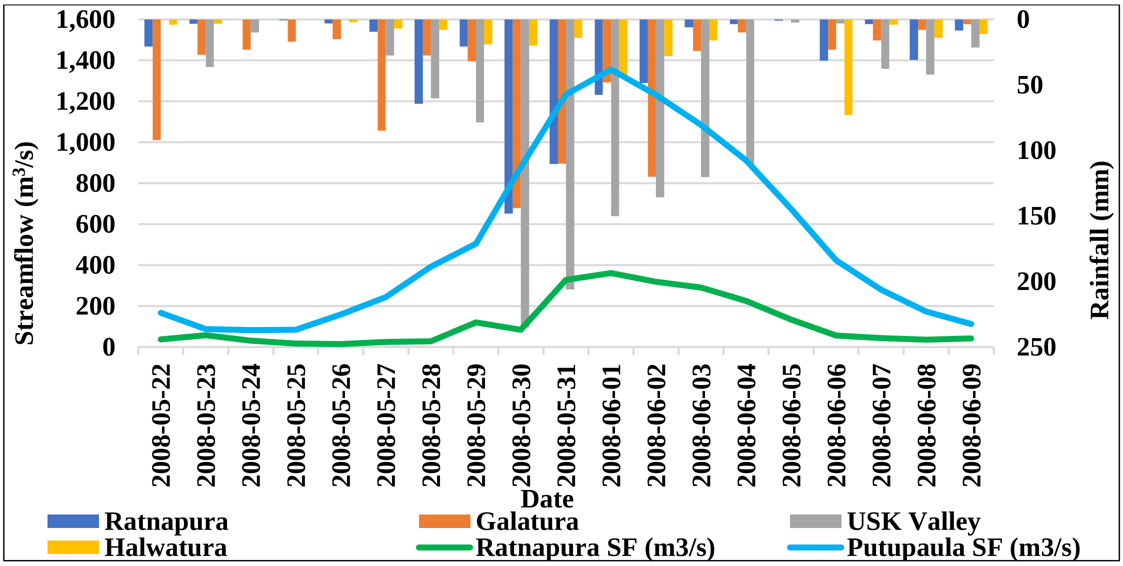

Figure 4-10: Dataset for 2008 flood event

4.3 Sensitivity Analysis

The RRI model has three streamflow cases or assumptions for every basin network, based on land and soil properties as follows: a) surface overflow, b) penetration abundance surface spillover and Green-Ampt model for vertical invasion, and c) immersion overabundance surface run-off and unsaturated subsurface overflow (Ramsy, 2019).

Sensitivity analysis was performed to estimate the weights of various control parameters using the three model configurations described above (Fattah et al., 2018). This model was calibrated using the Putupaula streamflow station.

The Manning's roughness coefficient n_r value, hillslope coefficient n_s, soil depth *d*, and lateral saturated hydraulic conductivity *Ka* were used for sensitivity analysis in the RRI model. The values were adjusted to those between the highest and lowest values specified by the RRI manual. This was to evaluate the impact of these parameters on the discharge, water level, and inundation area simulated by the RRI model. Table 4-2 shows the default and range values of different parameters along with their processes for analysis in the RRI model.

Table 4-3 shows the parameters selected for this study area along with their default values and range values. Manning's roughness coefficient for river channel, hillslope coefficient, soil depth, and lateral saturated hydraulic conductivity parameters was selected according to the relationship with the peak discharge, and the soil condition was considered for calibrating and validating the RRI model.

Table 4-2: Parameter value and ranges for sensitivity analysis

Sl No.	Parameters		Default Values	Range Values	Process
1	n_r (m^3/s)	Manning's roughness coefficient for river channel	0.030	0.015-0.040	Channel
2	n_s (m^3/s)	Hillslope coefficient	0.300	0.150-1.000	Runoff
3	d (m)	Soil depth	1.000	0.500-2.000	Soil

Sl No.	Parameters		Default Values	Range Values	Process
4	gammaa	Soil porosity	0.475	0.300-0.500	Soil
5	Ksv (m/s)	Vertical saturated hydraulic conductivity	$5.56*10^{-7}$	$6.540*10^{-5}$ – $1.670*10^{-7}$	Soil
6	S_f (m)	Suction at vertical wetting front	0.316	0.049-0.316	Soil
7	Ka (m/s)	Lateral saturated hydraulic conductivity	0.100	0.010-0.300	Soil
8	gammam	Unsaturated effective porosity	0.000	0.020-0.400	Soil

Table 4-3: Considering different values for sensitivity analysis

Sl No.	Parameters		Default Values	Range Values
1	n_r (m^3/s)	Manning's roughness coefficient for river channel	0.03	0.015-0.04
2	n_s (m^3/s)	Hillslope coefficient	0.30	0.15-1.00
3	d (m)	Soil depth	1.00	0.50-2.00
4	Ka (m/s)	Lateral saturated hydraulic conductivity	0.10	0.01-0.30

Table 4-4: Parameters considered for sensitivity analysis

Sl No.	Parameter	Parameter Values	Peak Discharge (m^3/s)
1	Hillslope Coefficient	0.150	949.50
		0.350	958.86
		0.500	978.05
		0.800	1,311.00

Sl No.	Parameter	Parameter Values	Peak Discharge (m^3/s)
2	Manning's roughness coefficient for river channel	0.015	1,413.00
		0.017	1,219.38
		0.020	995.30
		0.030	953.68
3	Soil depth	0.100	1,056.83
		0.500	972.31
		1.000	953.68
4	Lateral saturated hydraulic conductivity	0.010	948.95
		0.100	953.00
		0.300	955.70

Table 4-4 shows the parameter considered and their values with the peak discharge simulated from the RRI model for the sensitivity analysis. Different values were considered from the range values of each parameter. These values were then compared with the magnitude of the discharge obtained from the RRI model. The highest peak discharge was obtained when the hillslope coefficient was 0.8 and Manning's roughness coefficient for the river channel was 0.015.

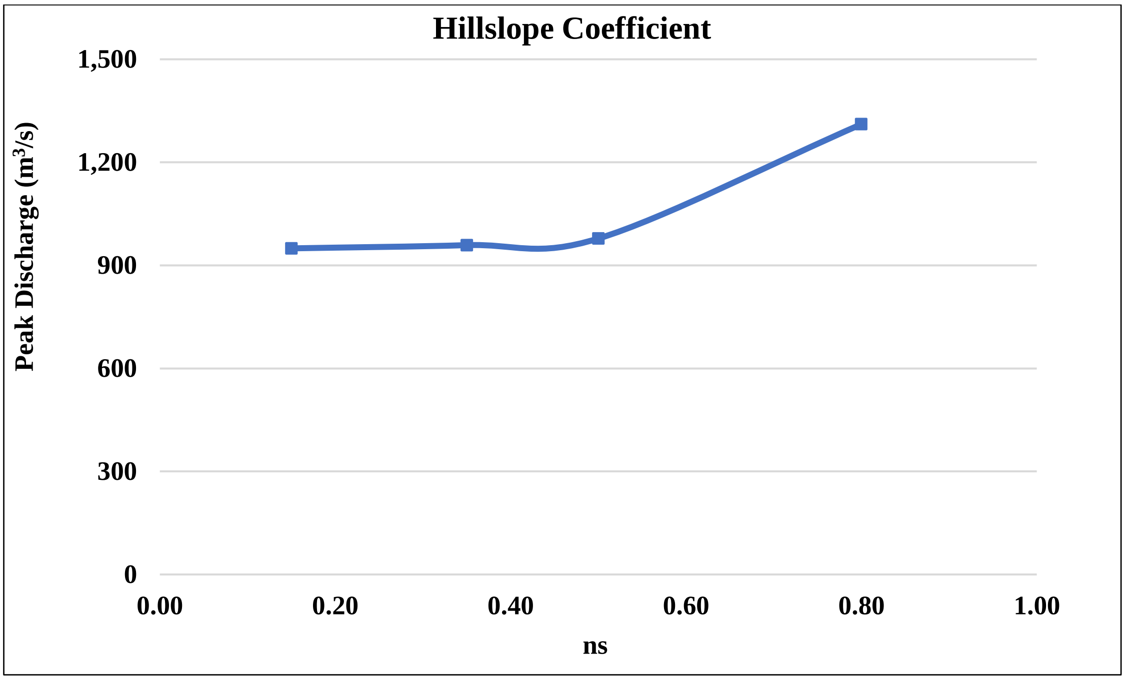

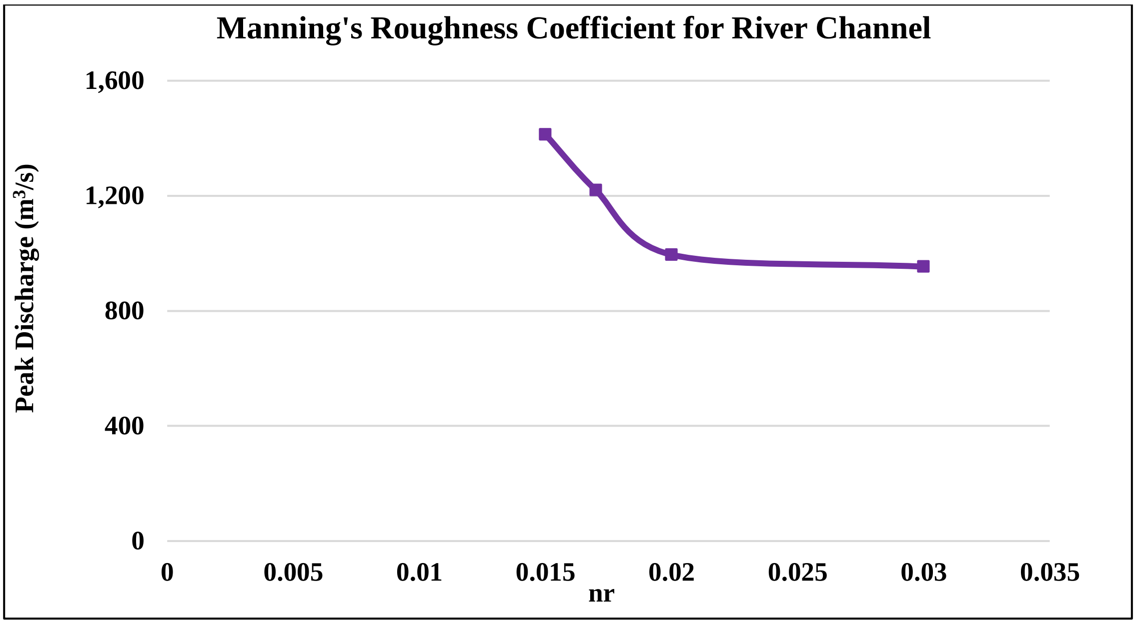
Manning's Roughness Coefficient for River Channel
Peak Discharge (m3/s)
1,600
1,200
800
400
0
0
0.005
0.01
0.015
0.02
0.025
0.03
0.035
nr

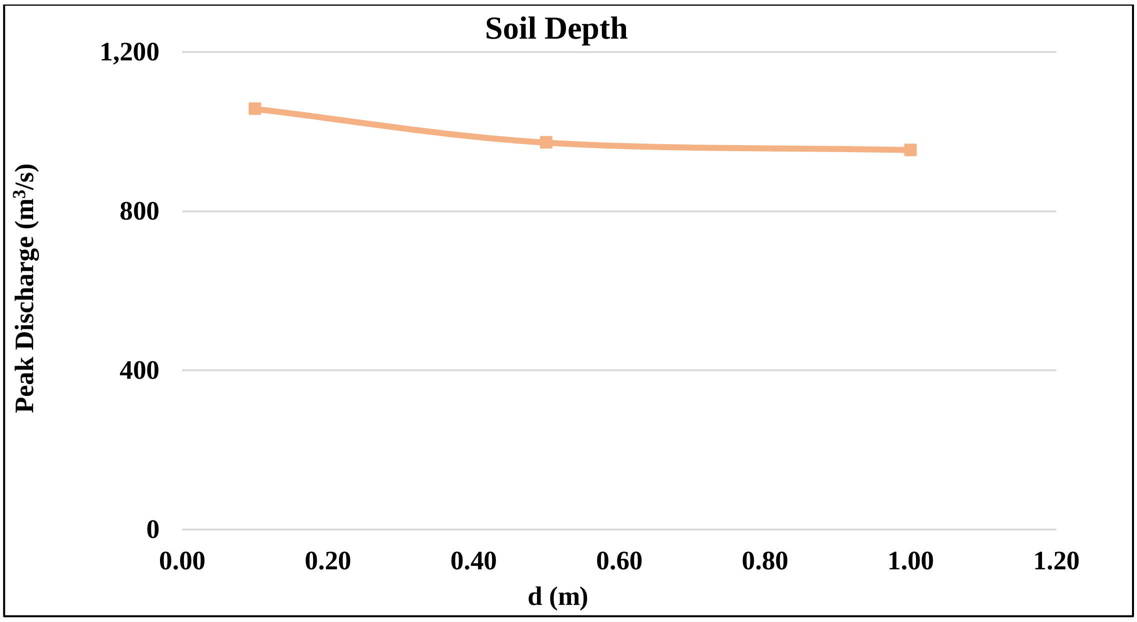
Soil Depth
Peak Discharge (m3/s)
1,200
800
400
0
0.00
0.20
0.40
0.60
0.80
1.00
1.20
d (m)

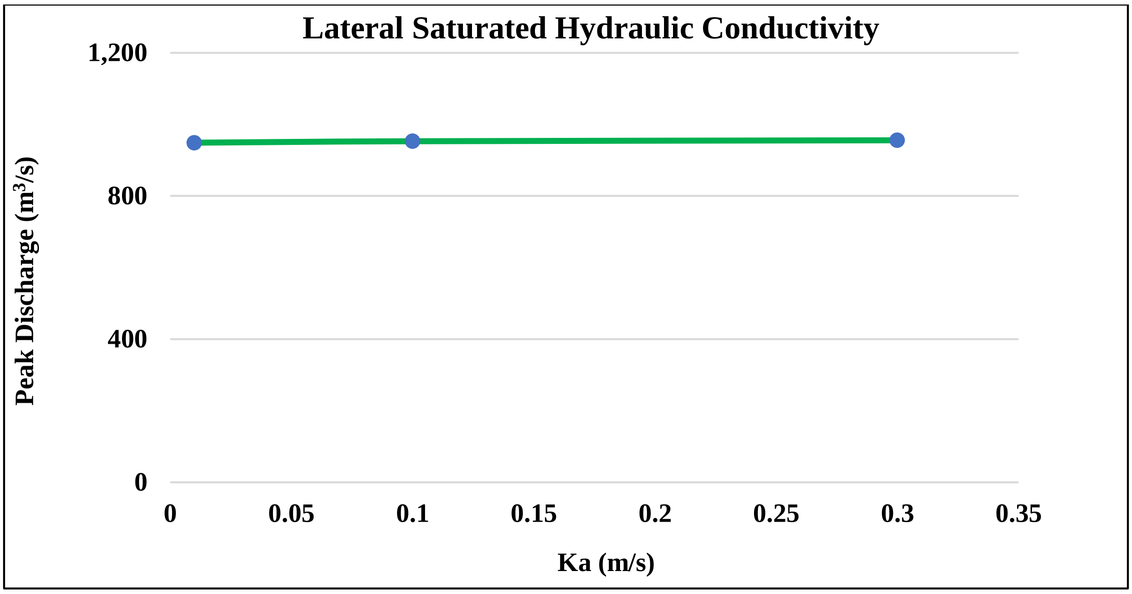

Figure 4-11: Sensitivity analysis graph for Manning's roughness coefficient for the river, hillslope coefficient, soil depth, and lateral saturated hydraulic conductivity

From the sensitivity analysis shown in Figure 4-11, the most sensitive parameters were found to be Manning's roughness coefficient for the river channel and hillslope coefficient.

The hillslope coefficient parameter was found to be directly proportional to the peak discharge as it depends on the slope of the landuse of the catchment. The slope of the landuse is related to the soil characteristics and the types of landuse present in the catchment. Therefore, the more the slope, the more peak discharge will be simulated in the catchment.

The Manning's roughness coefficient for the river channel was found to be indirectly proportional to the peak discharge as it depends on the characteristics of the bed materials of the river. From Manning's equation:

$$Q = A * \frac{1}{n} R^{2/3} S^{1/2} \quad [4\text{-}13]$$

where, Q = discharge (m^3/s)

A = area of the catchment (m^2)

R = hydraulic radius (m)

S = bed slope (m/m)

Discharge *Q* is inversely proportional to *n*, which is the roughness of the river channel. Increasing roughness increases the friction between the river bed and the water. This decreases the velocity which additionally decreases the flow rate of water.

Figure 4-12 represents the peak model discharge of about 665.91 m^3/s, Figure 4-13, and Figure 4-14 shows the inundation area and maximum water level, respectively from the RRI model which is about 8 m during the initial run of the RRI model for the 2008 flood event.

Figure 4-12: Model discharge from RRI model at the outlet

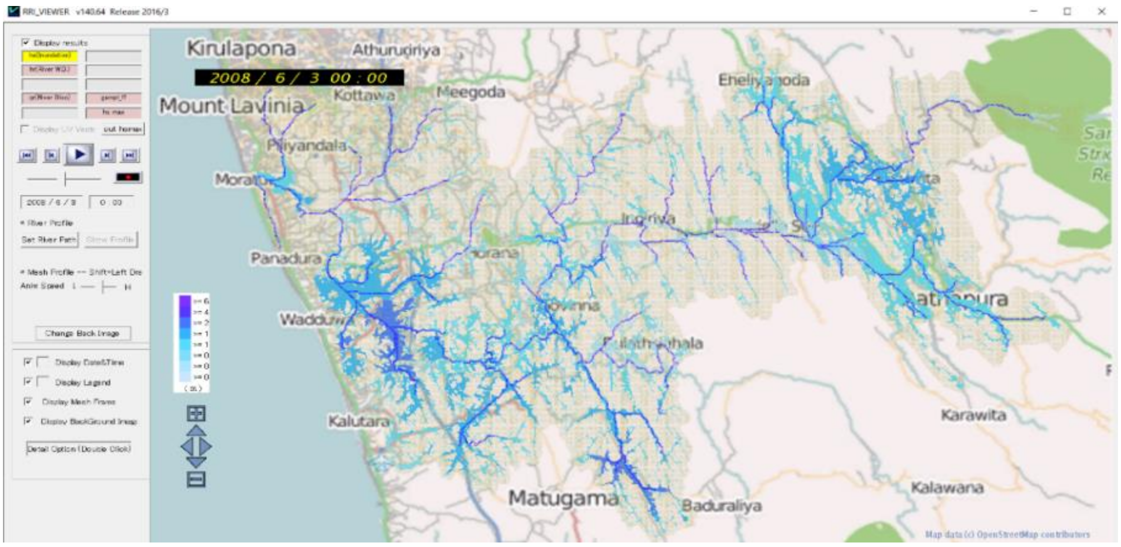

Figure 4-13: Inundation area obtained for 2008 flood event

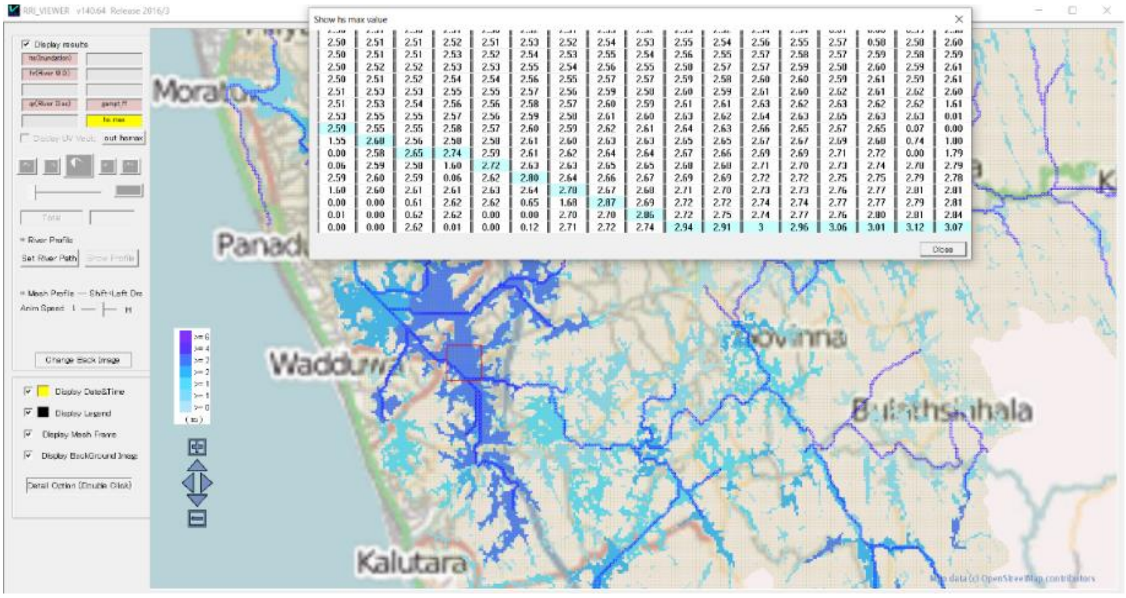

Figure 4-14: Maximum inundation at the outlet for 2008 flood event

CHAPTER 5

5 RESULTS

To perform calibration of the RRI model, 2008 and 2014 flood events were selected, and validation was obtained by the 2016 and 2017 flood events. The objective functions for each flood event were calculated to check the performance of the model with the observed streamflow values. According to the RRI manual, there are three types of soil conditions depending on the infiltration and subsurface process.

A. Only overland flows without infiltration or subsurface flow processes are considered.

B. Infiltration surplus overland flow and vertical infiltration flow are considered.

C. Saturation excess overland and saturated subsurface flow are considered.

Table 5-1: RRI model parameter in different flow conditions

Case A	**Case B**	**Case C**
Ksv = 0	n_r = 0.015-0.04	Ksv = 0
	n_s = 0.15-1	
Ka = 0	d = 0.5-2	Ka = 0.01-0.3
	gamma = 0.3-0.5	

For this study, the soil was considered 100 % saturated condition which means that the soil has reached its saturation level and water cannot penetrate more inside the soil particles. Hence, there will be no suction pressure, which means water coming to the catchment will be directly contributed to the runoff. Therefore, for this study Case C was selected where saturation excess overland flow and saturated subsurface flow were considered in calibrating and validating the RRI model shown in Table 5-1.

5.1 Model Calibration

The calibration of the RRI model was obtained by setting the parameter values after optimization. From the sensitivity analysis shown in Table 4-4, it was found that the peak discharge values match well with the observed streamflow data when Manning's roughness coefficient value was 0.015. Hence, it was considered for calibrating the model. Similarly, peak discharge values match well with the observed streamflow data when the hillslope coefficient value was 0.8, soil depth was 0.1 m, and lateral saturated hydraulic conductivity was 0.3 m/s. Therefore, the values of the parameters used were: 0.015 for Manning's roughness coefficient for river channel (n_r), 0.8 for hillslope roughness coefficient (n_s), 0.1 m for soil depth (d), and 0.3 for lateral saturated hydraulic conductivity (Ka). The following Table 5-2 shows the calibration result of the 2008 flood event.

Table 5-2: Calibration results for 2008 flood event

Date	Model SF (m^3/s)	Water Level (m)	Observed SF (m^3/s)	Total RF (mm)
2008-05-22	162.00	2.22	167.67	116.70
2008-05-23	63.00	1.71	87.65	69.70
2008-05-24	72.00	1.69	82.95	33.00
2008-05-25	71.00	1.67	85.29	17.70
2008-05-26	105.00	2.07	158.88	20.20
2008-05-27	246.00	3.26	244.51	128.80
2008-05-28	441.00	4.33	392.19	160.00
2008-05-29	895.00	5.86	505.39	150.20
2008-05-30	1,202.00	6.78	878.39	547.10
2008-05-31	1,310.00	7.17	1,233.60	440.20
2008-06-01	1,311.00	7.28	1,355.63	297.70
2008-06-02	1,084.00	6.95	1,232.56	332.20
2008-06-03	774.00	6.10	1,085.06	166.40
2008-06-04	480.00	5.03	911.04	124.10
2008-06-05	527.00	4.91	675.33	3.20
2008-06-06	691.00	4.71	424.45	130.50
2008-06-07	574.00	4.47	280.09	61.30
2008-06-08	172.00	2.58	173.06	95.00
2008-06-09	88.00	2.05	112.46	44.20

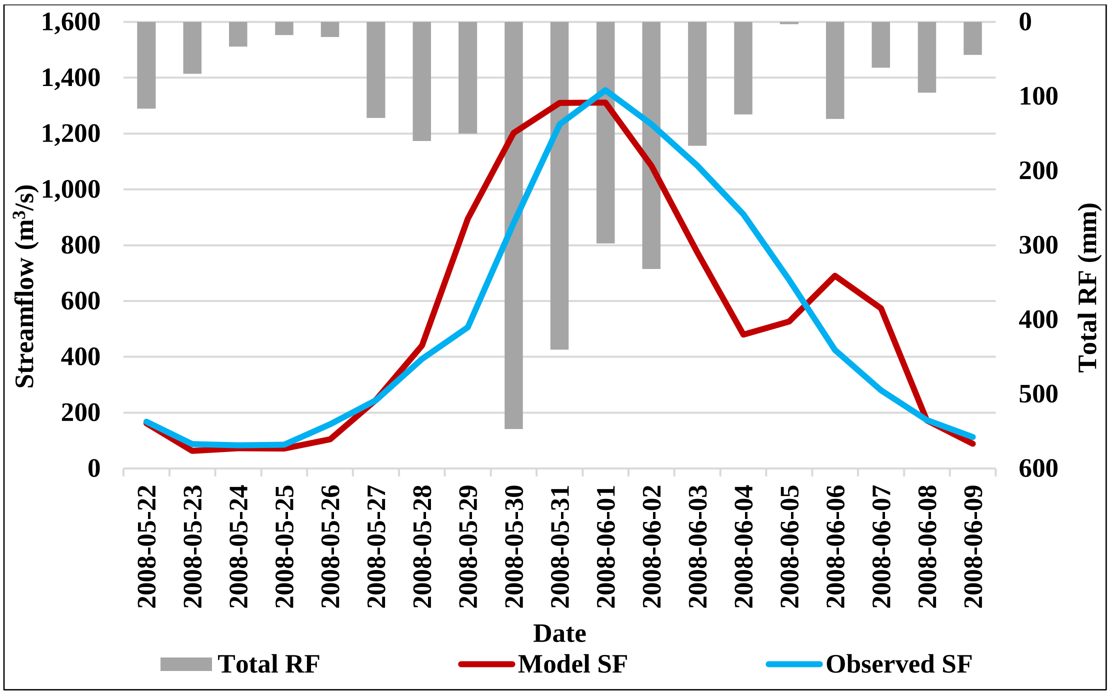

Figure 5-1: Simulated discharge and observed discharge with total rainfall for calibration of 2008 flood event

Table 5-3: Objective function values for calibration of 2008 flood event

Objective Function	**Values**
Root Mean Square Error (RMSE)	0.44
Mean Squared Error (MSE)	0.19
R Square (RSQ)	0.80
NSE	0.79

Figure 5-1 shows the model peak discharge of 1,311 m^3/s and a maximum water level of about 7.28 m which were obtained for the 2008 flood event. The objective function was calculated using Equations [2-1], [2-2], and [2-3] for the 2008 flood event shows an R^2 value of 0.80, RMSE of 0.44, MSE of 0.19, and NSE of 0.79 which shows good performance of the model shown in Table 5-3.

The flood event of 2014 was moreover calibrated using the same parameter values and the output is shown in Table 5-4.

Table 5-4: Calibration results for 2014 flood event

Date	Model SF (m^3/s)	Water Level (m)	Observed SF (m^3/s)	Total RF (mm)
2014-05-28	178.63	2.32	85.65	54.04
2014-05-29	62.74	1.68	250.04	58.23
2014-05-30	170.82	2.45	570.60	84.64
2014-05-31	410.69	4.17	747.03	90.92
2014-06-01	998.03	6.24	949.09	354.16
2014-06-02	1,137.56	6.82	1,003.48	326.38
2014-06-03	1,020.56	6.74	906.04	221.19
2014-06-04	693.00	5.94	788.22	119.97
2014-06-05	592.73	5.17	499.37	82.26
2014-06-06	455.91	4.06	257.89	15.97
2014-06-07	227.28	3.34	192.60	30.65
2014-06-08	255.14	3.39	125.40	80.07
2014-06-09	253.48	3.43	151.11	48.52
2014-06-10	437.93	4.38	334.53	127.90
2014-06-11	528.45	4.85	401.32	134.26

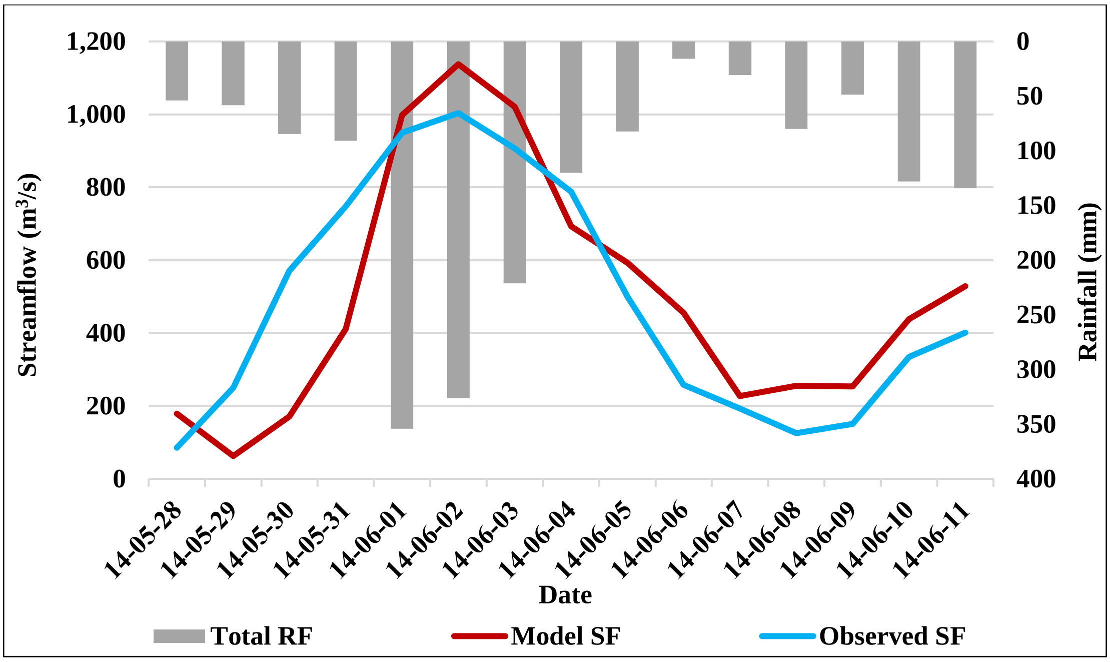

Figure 5-2: Simulated discharge and observed discharge with total rainfall for calibration of 2014 flood event

Figure 5-3 shows the model peak discharge of 1,137.56 m^3/s and a maximum water level of about 6.82 m which were obtained for the 2014 flood event. The objective function for the 2014 flood event in Table 5-5 shows an R^2 value of 0.72, RMSE of

0.39, MSE of 0.15, and NSE value of 0.68 which shows good performance of the model.

Table 5-5: Objective function values for calibration of 2014 flood event

Objective Function	**Values**
Root Mean Square Error (RMSE)	0.39
Mean Squared Error (MSE)	0.15
R Square (RSQ)	0.72
NSE	0.68

5.2 Model Validation

The validation of the RRI model was performed for 2016 and 2017 flood events with the same parameters that were used for calibration for 2008 and 2014 flood events. Table 5-6 shows the validated results of the 2016 flood event.

Table 5-6: Validation results for 2016 flood event

Date	**Model SF (m^3/s)**	**Water Level (m)**	**Observed SF (m^3/s)**	**Total RF (mm)**
2016-05-08	213.92	2.41	154.70	27.50
2016-05-09	65.94	1.75	189.84	70.00
2016-05-10	57.31	1.69	188.11	26.20
2016-05-11	171.19	2.60	228.01	95.70
2016-05-12	195.81	2.89	191.30	77.10
2016-05-13	211.59	3.09	624.61	63.80
2016-05-14	307.29	3.65	859.52	142.90
2016-05-15	523.14	4.57	975.95	194.00
2016-05-16	895.19	4.93	996.77	171.30
2016-05-17	681.41	4.92	969.37	155.70
2016-05-18	622.94	4.84	901.39	121.80
2016-05-19	486.68	4.57	809.61	113.70
2016-05-20	366.68	4.04	623.15	57.80
2016-05-21	253.35	3.40	324.51	67.50
2016-05-22	218.18	3.11	227.73	36.00
2016-05-23	192.38	3.01	253.37	49.70
2016-05-24	186.27	2.94	246.06	36.00

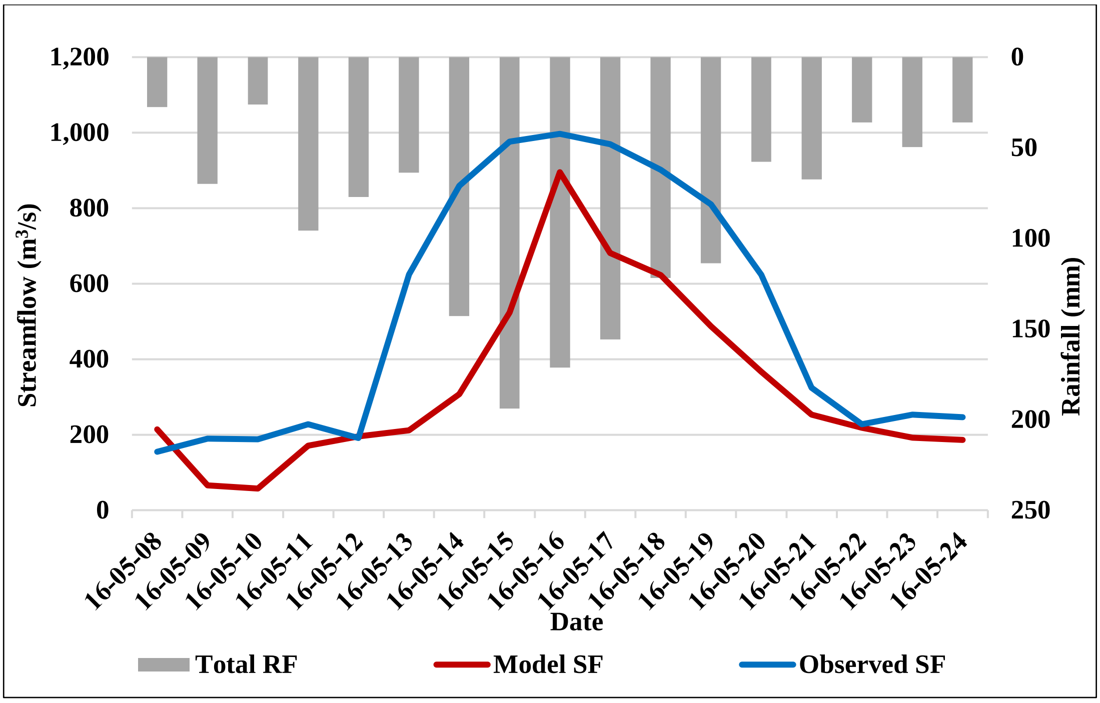

Figure 5-3: Simulated discharge and observed discharge with total rainfall for validation of 2016 flood event

Table 5-7: Objective function values for validation of 2016 flood event

Objective Function	**Values**
Root Mean Square Error (RMSE)	0.56
Mean Squared Error (MSE)	0.31
R Square (RSQ)	0.75
NSE	0.50

Figure 5-3 shows the model peak discharge of about 895.19 m^3/s and the maximum water level of about 4.93 m which were obtained for the 2016 flood event. The objective function in Table 5-7 for the 2016 flood event shows an R^2 value of 0.75, RMSE of 0.56, MSE of 0.31, and NSE value of 0.50 which shows overall satisfactory performance of the model. The validated results for the 2017 flood event, where model streamflow and water level are shown below in Table 5-8.

Table 5-8: Validation results for 2017 flood event

Date	Model SF (m^3/s)	Water Level (m)	Observed SF (m^3/s)	Total RF (mm)
2017-05-09	244.56	1.47	75.05	35.84
2017-05-10	66.05	1.75	79.13	64.79
2017-05-11	82.43	1.72	85.26	24.59
2017-05-12	64.22	1.67	76.73	49.78
2017-05-13	61.28	1.84	86.37	3.41
2017-05-14	69.12	2.30	198.31	245.96
2017-05-15	146.63	4.71	188.68	133.13
2017-05-16	509.36	4.81	89.46	14.80
2017-05-17	506.15	3.66	106.03	17.08
2017-05-18	274.78	3.31	156.67	117.32
2017-05-19	253.20	3.72	75.54	30.88
2017-05-20	330.34	3.27	61.04	16.14
2017-05-21	225.78	3.01	59.99	36.38
2017-05-22	184.97	3.03	58.44	49.91
2017-05-23	202.26	3.79	103.99	101.77
2017-05-24	354.45	5.43	365.76	301.71
2017-05-25	848.94	7.70	1,096.13	1,178.65
2017-05-26	1,658.98	9.21	2,005.57	267.41
2017-05-27	2,398.28	9.38	2,316.37	144.92
2017-05-28	2,208.44	8.72	2,129.33	93.60
2017-05-29	1,717.90	8.07	1,797.83	169.71
2017-05-30	1,656.97	7.71	1,459.02	111.82
2017-05-31	1,184.26	6.76	533.82	49.38
2017-06-01	800.86	5.64	427.54	110.10
2017-06-02	544.17	5.31	319.45	49.30
2017-06-03	643.72	4.78	225.01	38.50
2017-06-04	569.25	3.80	174.54	51.60
2017-06-05	333.61	3.38	155.71	53.60
2017-06-06	230.64	3.22	133.84	58.10
2017-06-07	219.82	3.18	163.15	26.40
2017-06-08	229.49	2.95	130.81	24.00

Figure 5-4 shows the model peak discharge of about 2,398.28 m^3/s and the maximum water level of about 9.38 m which were obtained for the 2017 flood event. The objective function for the 2017 flood event in Table 5-9 shows an R^2 value of 0.90, RMSE of 0.53, MSE of 0.28, and NSE value of 0.87 which shows good performance of the model.

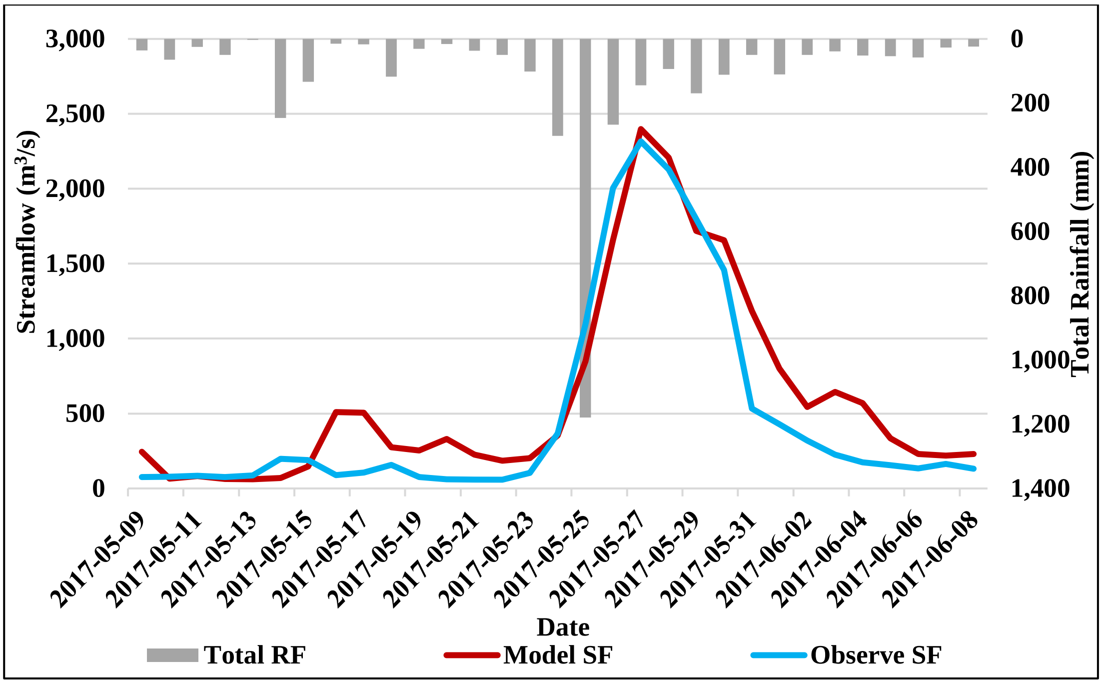

Figure 5-4: Simulated discharge and observed discharge with total rainfall for validation of 2017 flood event

Table 5-9: Objective function values for validation of 2017 flood event

Objective Function	Values
Root Mean Square Error (RMSE)	0.53
Mean Squared Error (MSE)	0.28
R Square (RSQ)	0.90
NSE	0.87

5.3 Inundation Analysis

For the verification of inundation areas from the RRI model, satellite-based flood event maps were generated in the Kalu Ganga basin. Sentinel 1A SAR data was used for the generation of the inundation areas. Since Sentinel 1A satellite was launched in October 2014, hence, the calibrated events of 2008 and 2014 were not taken into consideration for comparison of inundation analysis. The total flooded areas from the RRI model for the 2008 event are estimated to be 383.1 km^2, which is 25.1 % of the total area selected for the model. Both in Ratnapura and Kalutara part of the area is heavily flooded with a maximum inundation level of about 2.2 m to 7.1 m. The inundation area from the RRI model for the 2008 event is shown in Figure 5-5.

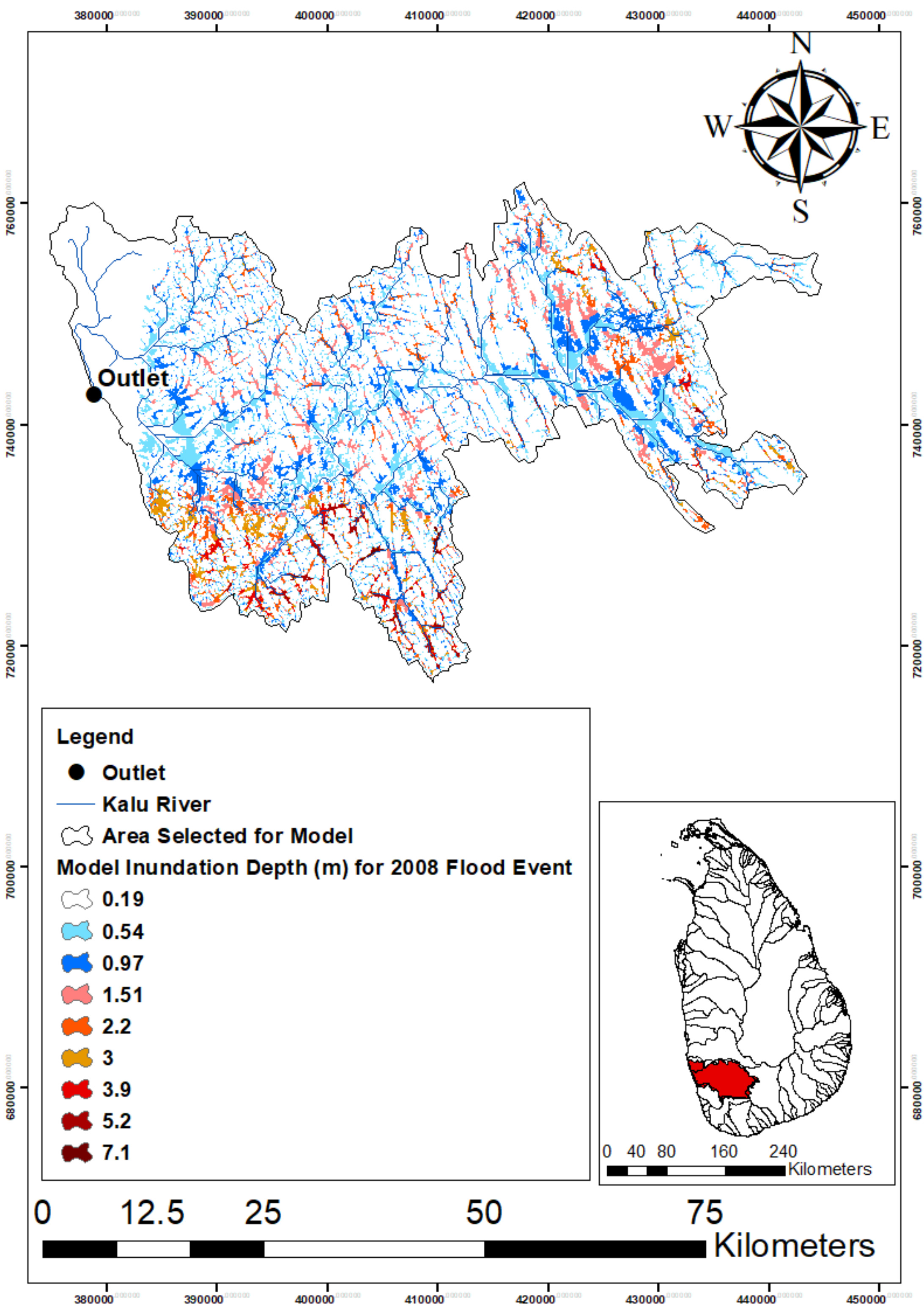

Figure 5-5: Inundation areas from RRI model for 2008 flood event

For the 2014 flood event, the total flooded areas from the RRI model were estimated to be 332.7 km^2, which is 21.8 % of the total area selected for the model. Mostly

Kalutara part of the area is heavily flooded and is followed in the Ratnapura part, with a maximum inundation level of about 1.3 m to 3.6 m. The inundation area from the RRI model for the 2014 event is shown in Figure 5-6.

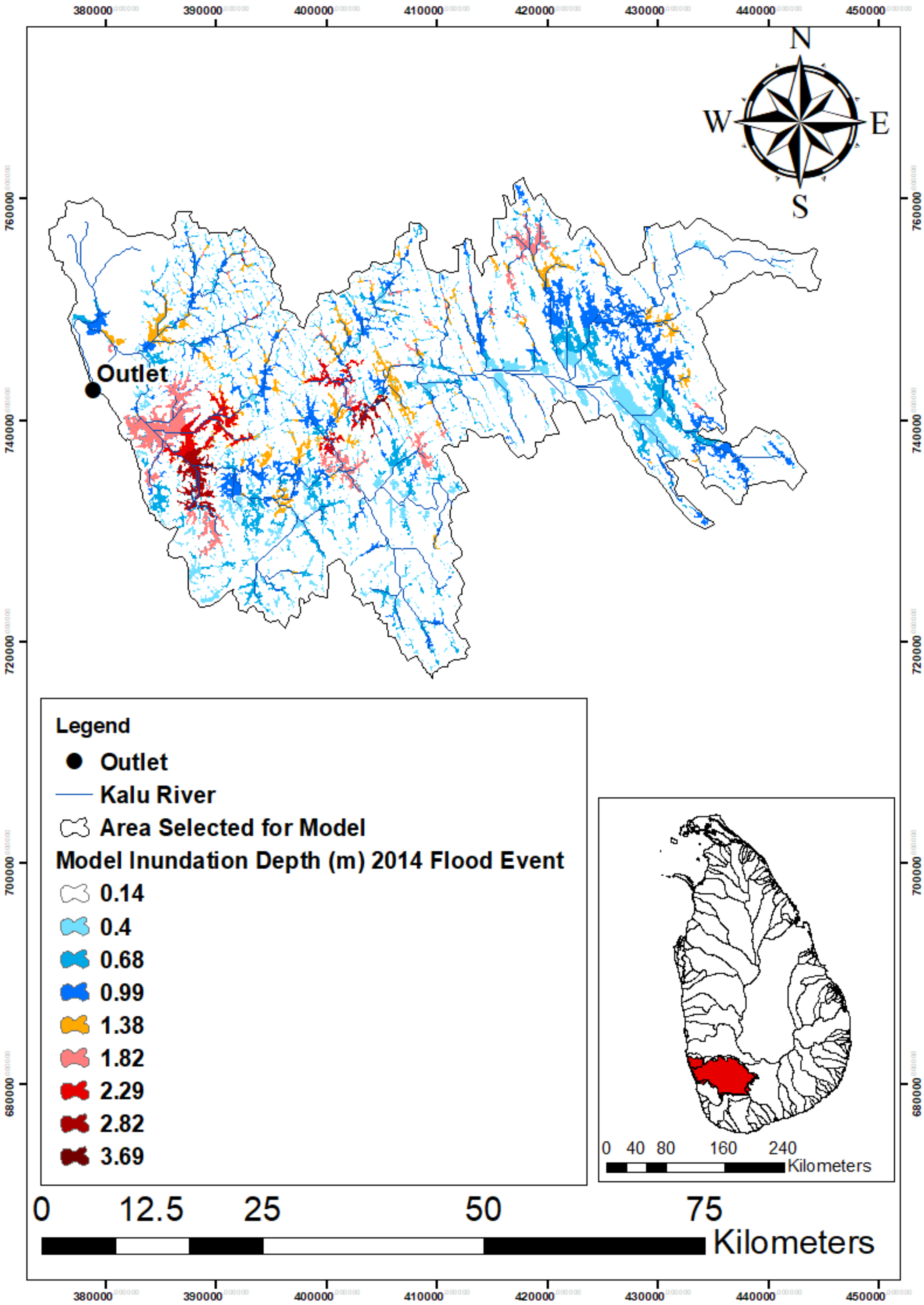

Figure 5-6: Inundation areas from RRI model for 2014 flood event

For the 2016 flood event, the inundation area from the RRI model was converted from ASCII format to raster format in ArcGIS and flooded areas were calculated, which is shown in Figure 5-7. The total flooded area from the RRI model was estimated to be 330 km^2, which is 21.62 % of the total area selected for the model. Mostly in Ratnapura part of the area is heavily flooded with a maximum inundation level of about 2.08 m to 3.32 m.

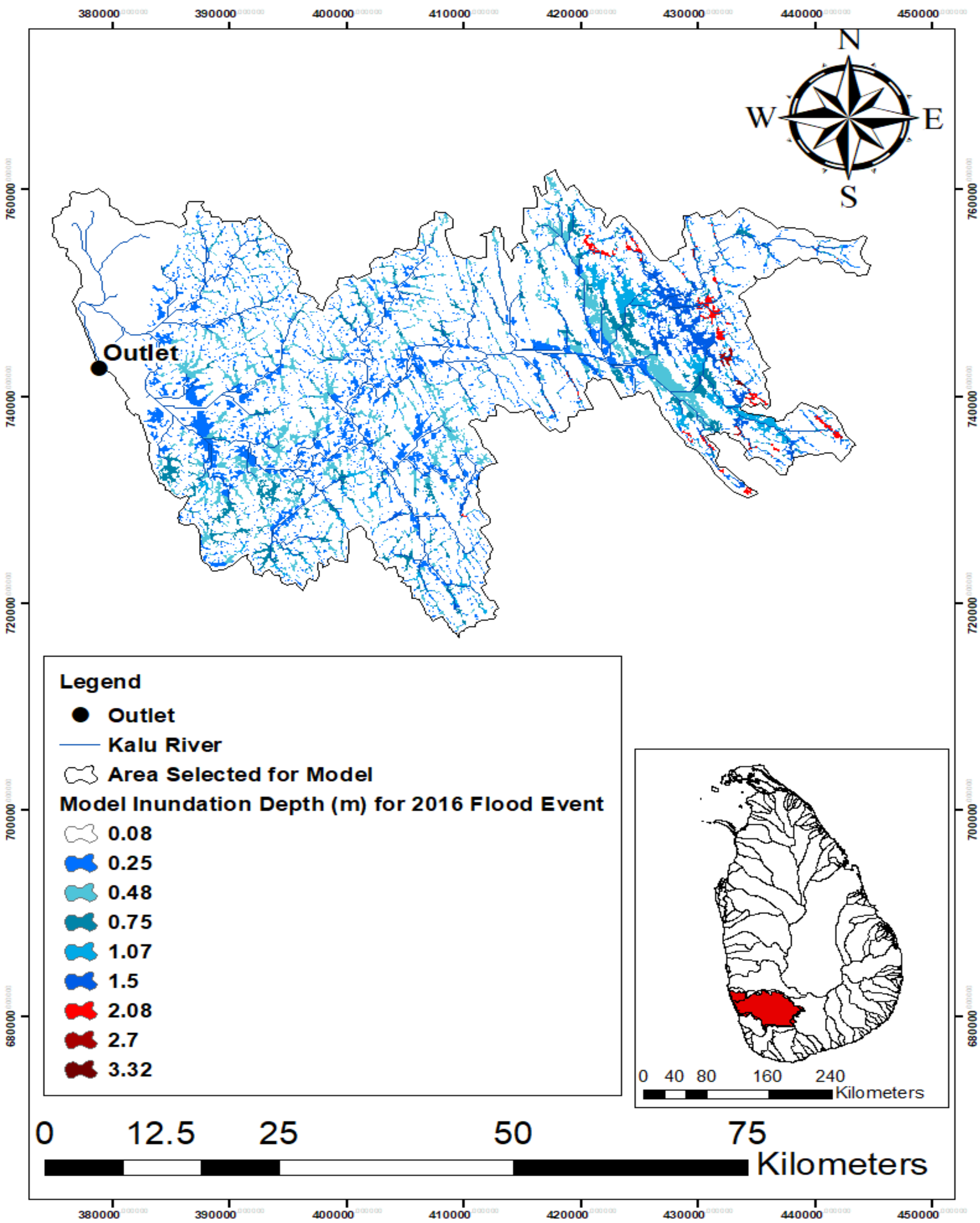

Figure 5-7: Inundation areas from RRI model for 2016 flood event

The Sentinel 1A images were pre-processed using SNAP software as described in the methodology flowchart shown in Figure 3-2. For 2016 and 2017 flood events, the SAR data is pre-processed and maximum likelihood classification was performed where the flooded areas of each two validated events were estimated. The following Table 5-10 shows the specifications of SAR data used for inundation analysis.

Table 5-10: Basic specifications of the Sentinel-1 datasets used in the study

Date of Acquisition	Satellite and Sensor	Format-Mode	Polarization
2016/05/22	Sentinel 1A- SAR (C Band)	GRD- IW	VV
2017/05/24	Sentinel 1A- SAR (C Band)	GRD- IW	VV

Figure 5-8 represents the Sentinel image of the 2016 flood event before pre-processing, and Figure 5-9 represents the Sentinel image after pre-processing. The difference in the two images can be seen and after pre-processing the river is visible in the dark colour due to the low backscattering coefficient (σ_0) compared to other features of the image. The Sentinel 1A image for 2016 was available for 5-days after the peak flood period. Hence, it was downloaded and pre-processed for flood mapping in the study area.

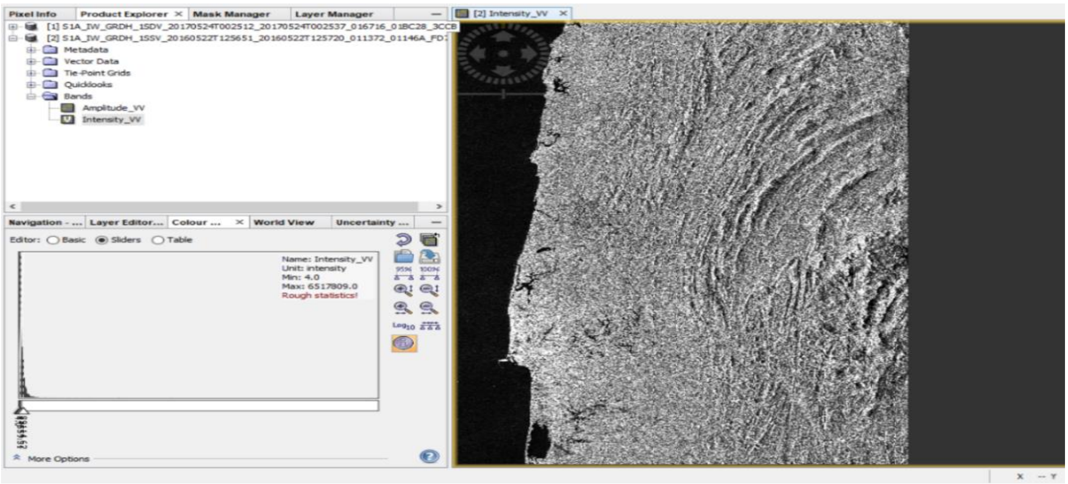

Figure 5-8: Sentinel 1A 2016 flood event before pre-processing *[Source: ESA- https://scihub.copernicus.eu/]*

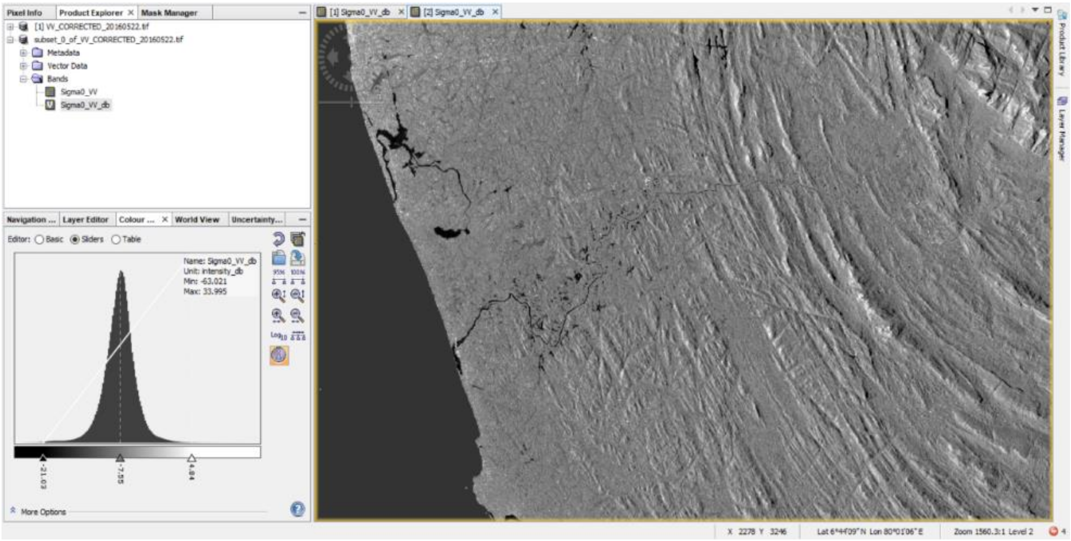

Figure 5-9: Sentinel 1A 2016 flood event after pre-processing

To enhance the pre-processed image further, threshold values were determined. Histogram thresholding is a simple and easy technique to segment an image. From a grayscale image, thresholding can be used to create binary images. The threshold method is used to distinguish between water and non-water features. The threshold values were found from the backscatter arithmetic histogram (Tavus, 2018). Low values in the backscatter (σ_0) histogram represent water and high values represent non-water classes. Visual examination of the arithmetic mean of the image determined the pixel value of the water surface. The pixel values of the water areas were found to be between -25.1 dB and -7.4 dB.

Figure 5-10 represents the histogram analysis of the arithmetic mean after correction for the 2016 flood event. The x-axis represents the intensity of the VV polarized image in decibel units (dB). The y-axis represents the frequency of the pixels determining the different classes using logical operators to binarize the image for the required area of interest.

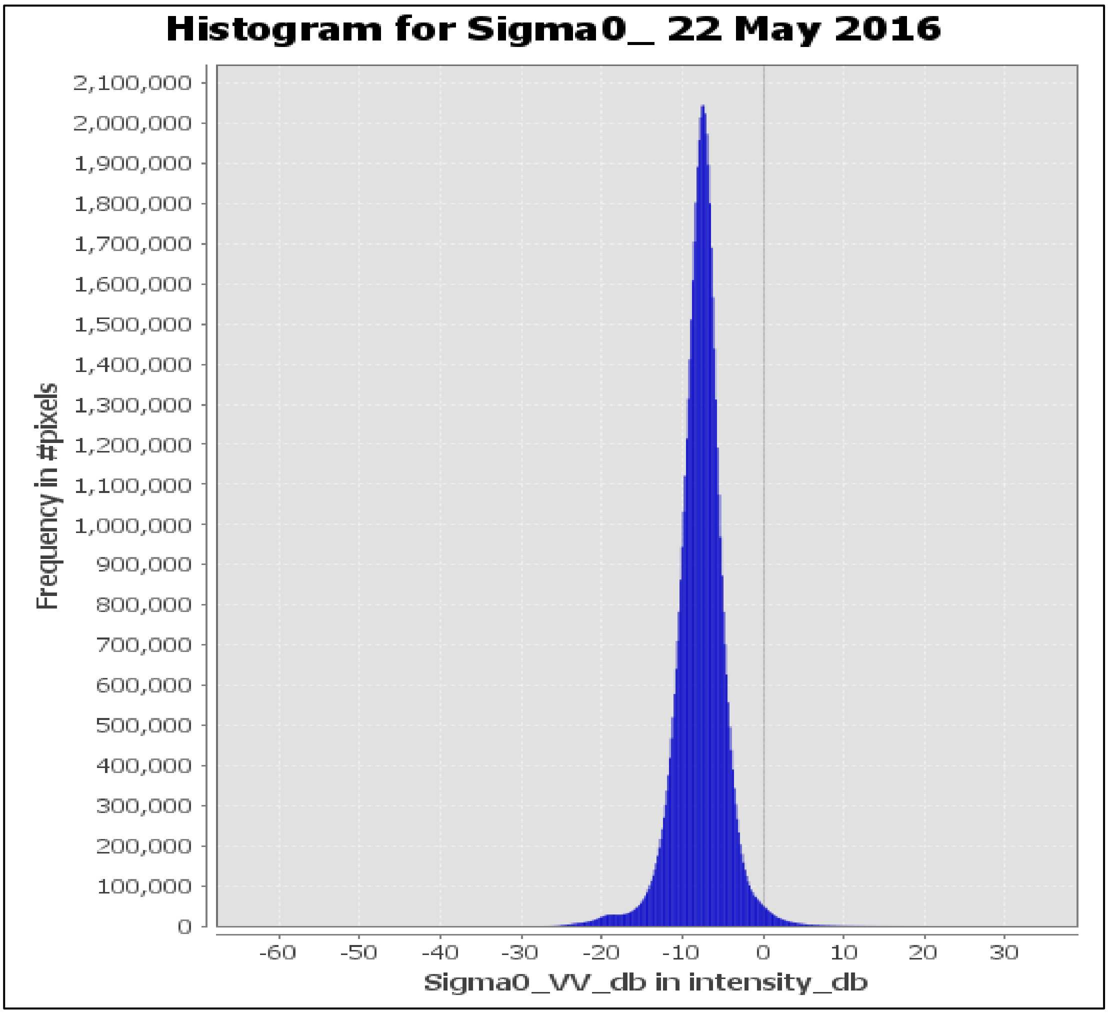

Figure 5-10: Histograms of arithmetic mean after correction for 2016 flood event

From the SAR image for the 2016 flood event, the classification of flood and non-flood was achieved by classifying the image as water and other class. This process is obtained by using maximum likelihood classification where the vector layers were drawn in the corrected SAR image. The total flooded area was estimated to be 239.7 km^2, which is 15.7 % of the total area selected for the model. The difference between the flooded areas from the RRI model and SAR image is about 90.2 km^2, which was 35.5 % of area difference from the total area selected for the model. Figure 5-11 shows the inundation areas of the 2016 event from the Sentinel 1A image.

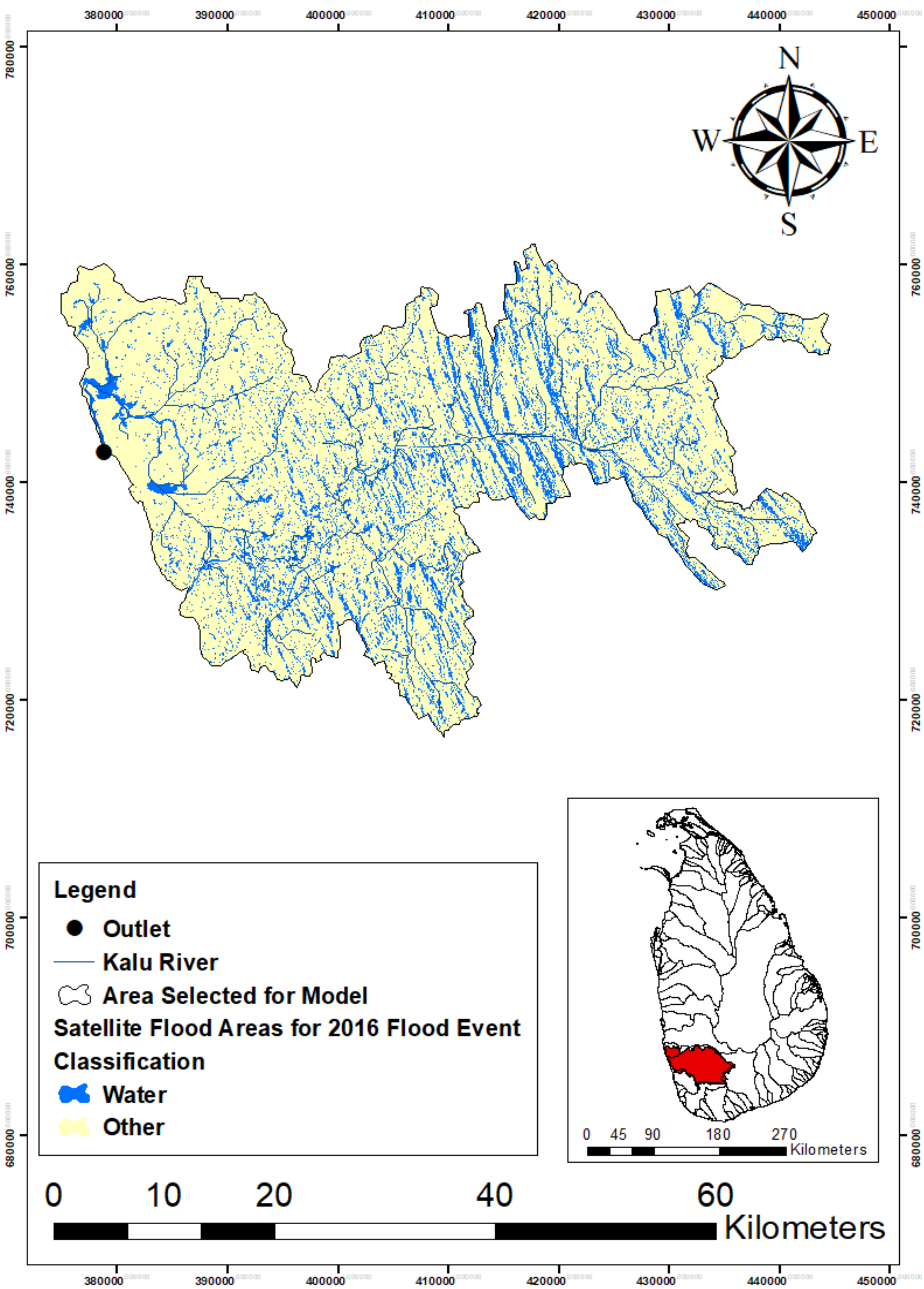

Figure 5-11: Inundation areas from Sentinel 1A image for 2016 flood event

For the 2017 flood event, the inundation area from the RRI model is converted from ASCII format to raster format in ArcGIS and flooded areas were calculated, which is shown in Figure 5-12. The total flooded area from the RRI model is estimated to be

409.1 km^2, which is 26.8 % of the total area selected for the model. Mostly in Kalutara, part of the area is heavily flooded with a maximum inundation level of about 2.6 m to 4.9 m. Some parts of Ratnapura are moreover flooded where the inundation is about 1.5 m to 2.0 m.

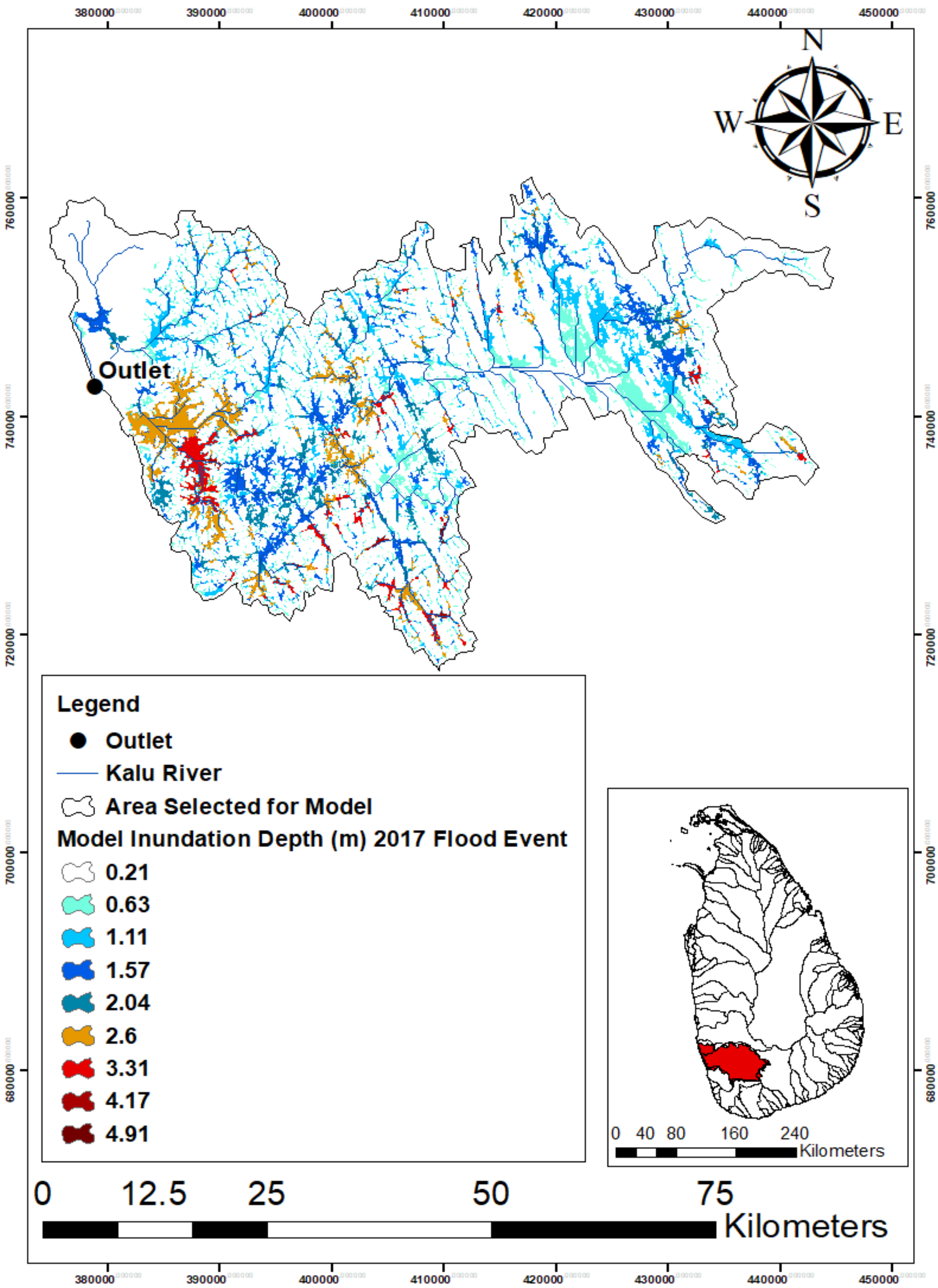

Figure 5-12: Inundation areas from RRI model for 2017 flood event

Similarly, Figure 5-13 represents the Sentinel image of the 2017 flood event before pre-processing, and Figure 5-14 represents the Sentinel image after pre-processing. For the 2017 flood event, the same methodology was applied as described in Figure 3-2. The Sentinel 1A image for 2017 was available for 3-days before the peak flood period. Hence, it was downloaded and pre-processed for flood mapping in the study area.

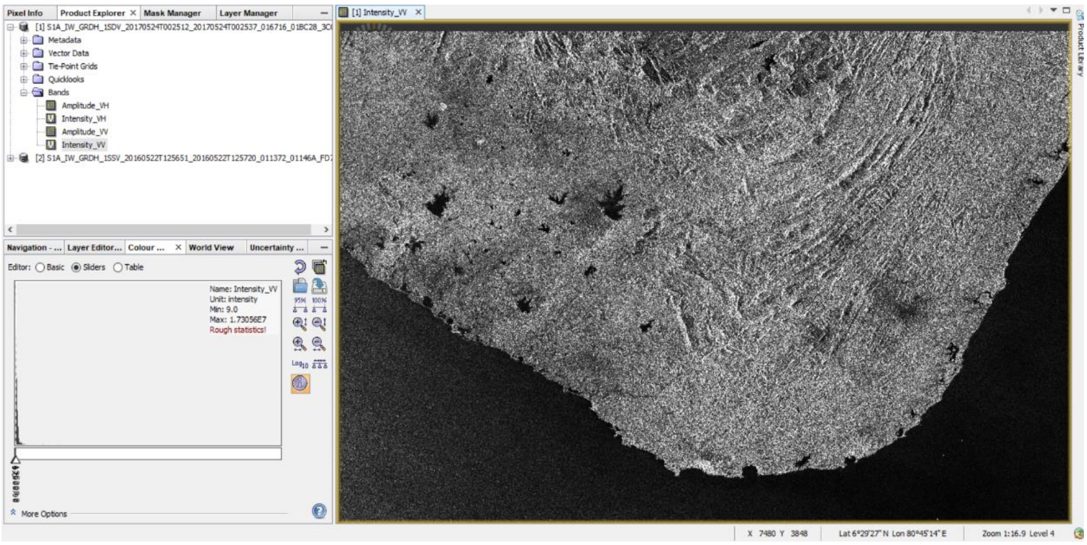

Figure 5-13: Sentinel 1A 2017 flood event before pre-processing *[Source: ESA-https://scihub.copernicus.eu/]*

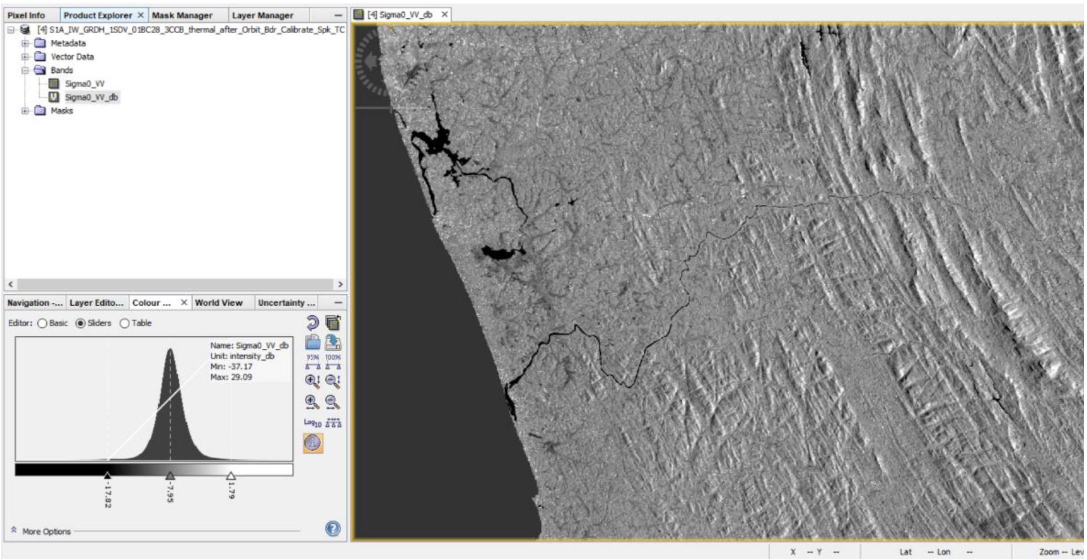

Figure 5-14: Sentinel 1A 2017 flood event after pre-processing

Similarly, to enhance the pre-processed image further, histogram thresholding values were determined. In the graphical representation for the arithmetic mean of the 2017 image, the pixel values of the water areas were found to be between -23.97 dB and -7.29 dB.

Figure 5-15 represents the histogram analysis of the arithmetic mean after correction for the 2017 flood event. The x-axis represents the intensity of the VV polarized image in decibel units (dB). The y-axis represents the frequency of the pixels determining the different classes using logical operators to binarize the image for the required area of interest.

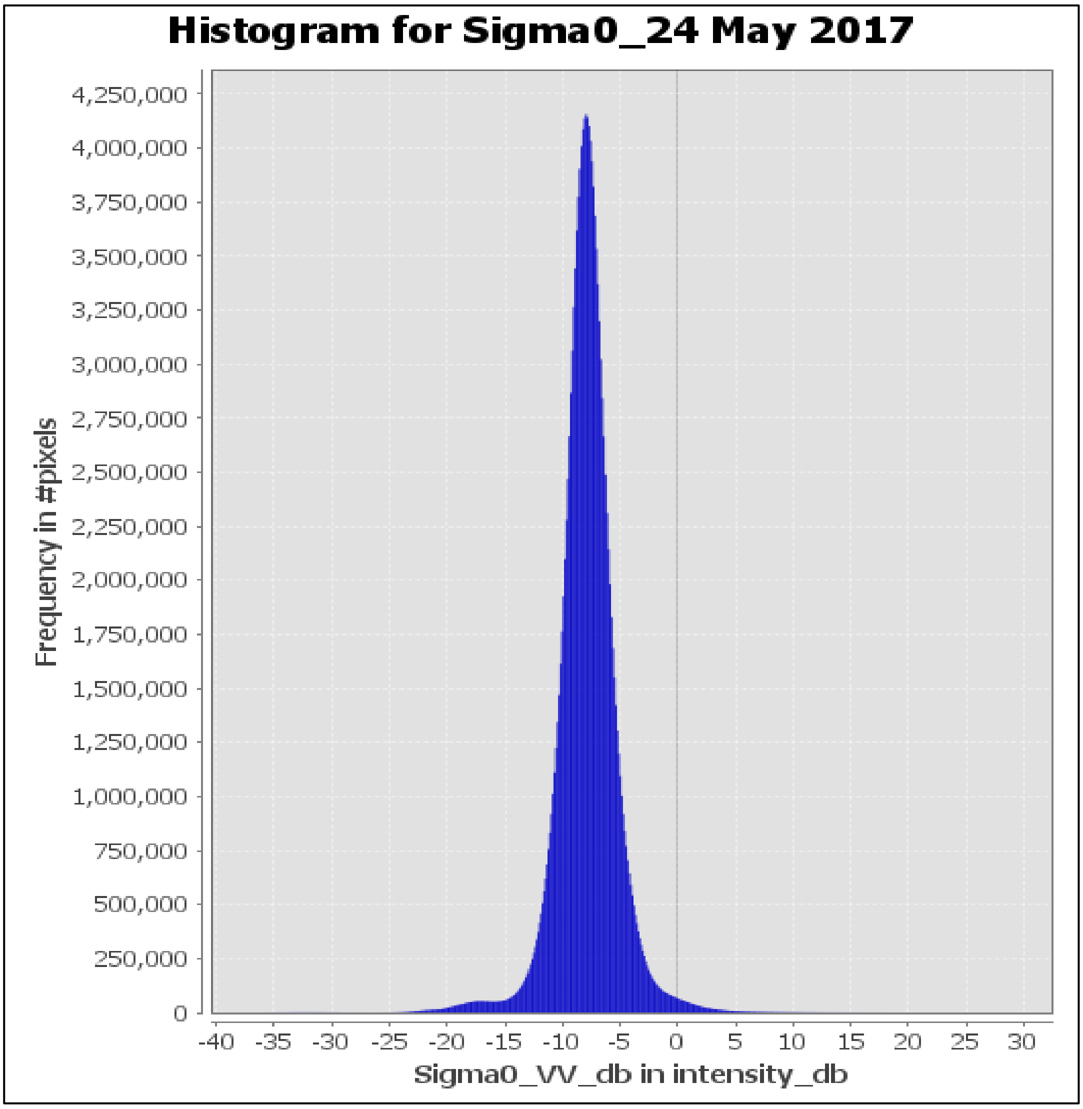

Figure 5-15: Histograms of arithmetic mean after correction for 2017 flood event

From the SAR data for the 2017 flood event, the classification of flood and non-flood was achieved by using maximum likelihood classification where the vector layers were drawn in the corrected SAR image. The total flooded area was estimated to be 335.4 km^2, which was 22.0 % of the total area selected for the model. The difference between the flooded areas from the RRI model and SAR image was about 73.7 km^2, which was 22.1 % of area difference from the total area selected for the model. Figure 5-16 shows the inundation areas of the 2017 event from the Sentinel 1A image.

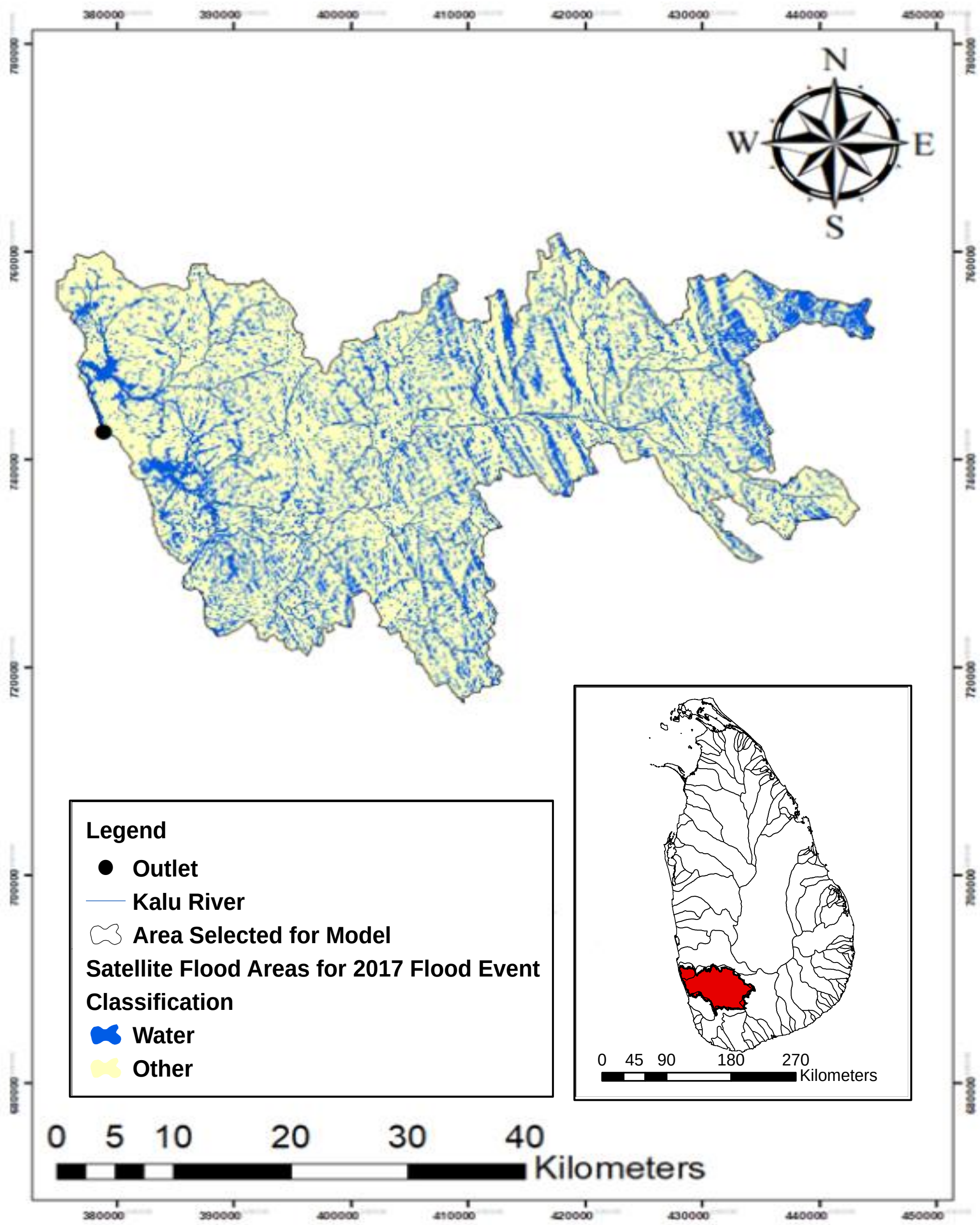

Figure 5-16: Inundation areas from Sentinel 1A image for 2017 flood event

CHAPTER 6

6 DISCUSSION

6.1 Data Analysis

Precipitation and streamflow data for the Kalu Ganga basin were analyzed from 1994 to 2017 to determine the consistency and accuracy to apply in the hydrological model. Four meteorological stations were selected using the Thiessen Polygon method, namely: Ratnapura, Halwatura, Galatura Estate, and USK Valley station as shown in Figure 3-6:. There were missing values in the precipitation data which was filled using the linear regression method shown in Figure 3-7. Ratnapura rainfall gauging station data had the maximum number of missing values of about 5.30 %, after that Halwatura station of about 3.50 %, followed by USK Valley station of about 2.16 % and Galatura Estate of about 1.33 %. Galatura Estate rainfall station experiences more annual rainfall compared to other stations as shown in Figure 3-11. The annual rainfall was observed to be about 3,500 to 5,000 mm but USK Valley station showed some inconsistent behaviour during the year 1989/90 and 1991/92. Annexure 1, shows the general arrangement of rainfall data in chronological order in Microsoft Excel.

According to Ampitiyawatta and Guo (2010) annual and monthly precipitation were identified and all analyzed precipitation stations showed negative annual precipitation trends. On average, there was a trend of -0.98 with annual precipitation decreasing by 12.03 mm/year. Putupaula and Ratnapura streamflow stations were selected for the development of the RRI model. From the streamflow analysis, the yearly variation of Putupaula and Ratnapura streamflow stations showed a decreasing trend over the years from 1994 to 2017 and 1981 to 2020, respectively as shown in Figure 3-18 and Figure 3-22. The maximum streamflow recorded was about 800 m^3/s in 1987/88 in Ratnapura station and about 2,500 m^3/s in the year 1994/95 in Putupaula station.

6.2 Selection of Events

In selecting the data period, the first data availability of Putupaula and Ratnapura river gauging stations was considered. Putupaula station has data from 1994 to 2017 and Ratnapura station had not functioned from 1996 to 2006. Hence, flood events were selected after the year 2006. Ratnapura streamflow data was considered as an inflow in the RRI model and Putupaula streamflow data was considered as the outflow, to compare with the simulated discharge obtained from the RRI model. Gumbel distribution for extreme events was plotted using the Putupaula station, where peak discharge is checked with the estimated return period (Subramanya, 2013). Therefore, 2008, 2014, 2016, and 2017 flood events were selected for this study area. The flood events were moreover considered by checking with some literature review to match with the calculated return period. Flood events for the 20-year and 50-year return period were selected for the RRI model which is described in Table 3-4.

6.3 Evaluation of Discharge from RRI Model

In this research project, the evaluation of discharge is computed by the RRI model considering four flood events. The 2008 and 2014 flood events were considered for calibration and the 2016 and 2017 flood events for validation. The river width and river depth parameters were obtained from Rasmy et al., (2019), where, C_W = 6.5, S_W = 0.35, C_D = 0.8 and S_D = 0.25. During the sensitivity analysis of the model, Manning's roughness coefficient for river channel (n_r) and hillslope coefficient (n_s) is found to be the most sensitive among the other parameters as shown in Figure 4-11. The parameter Manning's roughness coefficient for the river channel is inversely proportional to peak discharge. As the value of n_r decreases the peak discharge increases and vice-versa. The parameter hillslope coefficient (n_s) is directly proportional to peak discharge. As the value of n_s increases peak discharge moreover increases and vice-versa. Subsequently, when the parameter value soil depth (d) increases then the peak discharge decreases and for lateral saturated hydraulic conductivity (Ka), the parameter value is directly related to the peak discharge.

Considering the optimised parameter values of n_r = 0.015, n_s = 0.8, d = 0.1 and Ka = 0.3; the model shows good performance in all the four events. The n_r was taken considerably low value in the RRI model as the objective function was not showing good performance even after repeated runs of the model. Similarly, the value of n_s was considered slightly higher than the default range, to match the objective function in the model. However, all the parameter values lie within the range specified by the RRI manual. The model streamflow showed a comparatively similar trend and similar magnitude with the observed streamflow of each flood event. Out of the four flood events, the 2017 flood event showed a maximum amount of discharge of 2,398.28 m^3/s, a maximum water level of about 9.38 m, and maximum inundation of about 4.91 m in the Kalu Ganga basin as shown in Table 5-8. Detailed estimation of the calibration and validation of the RRI model for all flood events is shown in Annexure 2. Table 6-1 represents the evaluation of simulated peak discharge compared to the observed peak discharge along with the objective functions. All the flood events showed overall good performance with the RRI model.

Table 6-1: Evaluation of discharge along with the objective functions

Event	**Simulated Peak Discharge (m^3/s)**	**Observe Peak Discharge (m^3/s)**	**R^2**	**RMSE**	**MSE**	**NSE**
2008	1,311.00	1,355.63	0.801	0.444	0.198	0.796
2014	1,137.56	1,003.48	0.721	0.391	0.153	0.680
2016	895.19	996.77	0.756	0.56	0.314	0.509
2017	2,398.28	2,316.37	0.909	0.536	0.287	0.875

6.4 Evaluation of Inundation Areas

The inundation analysis was carried out by comparison of flooded areas from RRI and flooded areas from Sentinel 1A image. SAR is an active remote sensing data that has its source of illumination and can penetrate even through dense clouds. SAR can acquire data during day/night and in any weather conditions. SAR provides valuable information on all stages of the disaster life-cycle including prevention, mitigation, and recovery (Anusha, 2019).

Other satellite data like ALOS PALSAR, RADARSAT were not available for some of the flood events and MODIS satellite data has more than 90 % cloud cover during the peak flood periods. Removal of this 100 % cloud cover will not be accurate enough to process the image, hence, it was not considered the best option for flood mapping in the study area. However, for the 2008 flood event, ALOS PALSAR satellite image was used for flood risk analysis in the Kalu Ganga basin to calibrate and validate the HEC-RAS model (Samarasinghe, 2010). The authors have found that the ALOS PALSAR image was available 2-days after the flood peak. Therefore, it has given less flood extent than their HEC-RAS output. Hence, the 2008 flood event was not considered for inundation analysis in this study. Sentinel 1A SAR data was launched in October 2014, therefore, only 2016 and 2017 flood events are considered for comparison with the RRI model. The pre-processing of a SAR image is necessary to obtain the high accuracy details in the application of mapping. For the processing of images, it is performed using the SNAP toolbox, as the Sentinel data is very huge and becomes extremely difficult to process using regular database management tools (Gomathi, 2018). The pre-processing steps may vary with the recent demands on the levels of data. Waterbodies are mapped in the SAR data by making use of the difference in backscatter between the waterbody and the land surface. The flooded areas are clear as the spots with low backscatter return. The dark areas of the image are due to specular reflections from the smooth water surface, so the signal gets reflected from the sensor. The clear transition from smooth water to rough land surfaces translates into a corresponding transition from low to high backscatter. This enables the clear delineation of water surfaces in the image. However, in the SAR image, some of the valleys or hilly areas in the upper catchment were misclassified as flood-prone areas, as the pixel value of that part of the image is the same as that of water. Hence, during the maximum likelihood supervised classification, some of the upper parts of the catchment are moreover classified as water. This misclassification of the hilly areas as water has additionally occurred in the RRI model, which can be rectified using a fine resolution of the DEM of the study area.

According to various studies, Sentinel 1A SAR data allows us to easily differentiate between land surfaces and water surfaces, which enables rapid mapping of water body boundaries (Anusha & Bharathi, 2019). As the temporal resolution (i.e., revisit time) of the satellite is the main disadvantage, therefore, the flood extent was less in previous literature, furthermore, which agrees with my result as well.

However, to get accurate results, the selection of reference images is crucial to match the classified flooded areas in the satellite image. Due to the lack of reference data, it was not possible in this study. But still, the results are reliable and can be used which many authors have used in many parts of the world (Anusha & Bharathi, 2019; Tavus et al., 2019; Ezzine et al., 2018).

Therefore, to find the actual flood-prone areas in the study, the area of the permanent water bodies is calculated using the landuse map of the study area and it is subtracted from the respective flood map. The landuse map of the Kalu Ganga basin was collected from the Survey Department of Sri Lanka (1999) shown in Figure 3-5. Considering that the permanent waterbody areas do not change rapidly over time thus, it was calculated and subtracted from it.

Table 6-2 represents the actual flooded area from the RRI model and satellite image for both 2016 and 2017 flood events. The actual flooded area from RRI is found to be 291.97 km^2 and from satellite image is found to be 201.70 km^2 for the 2016 flood event. The area difference was found to be 35.54 % from the total area selected for the model. For the 2017 flood event, the actual flooded area from RRI is found to be 371.14 km^2 and from satellite image is found to be 297.42 km^2. Hence, the area difference was found to be 22.13 % from the total area selected for the model.

Table 6-2: Comparison of flooded areas from RRI model and satellite image

Flood Event	Flood Areas from RRI Model (km^2)	Flood Areas from Satellite image (km^2)	Area of Permanent Waterbody (km^2)	Actual Flooded Areas from RRI Model (km^2)	Actual Flooded Areas from Satellite image (km^2)	Difference of Percentage in Flooded Area
2016	330.00	239.73	38.03	291.97	201.70	35.54 %
2017	409.17	335.45	38.03	371.14	297.42	22.13 %

CHAPTER 7

7 CONCLUSIONS

From this study, the following points can be concluded:

- In this study, the hydrological model response of the watershed is studied with the use of remote sensing data. From the data analysis, the annual rainfall was found to be about 3,500-5,000 mm. The rainfall data showed a decreasing trend over the years from 1969 to 2020. From the streamflow analysis, the yearly variation of Putupaula and Ratnapura streamflow stations showed a decreasing trend over the years from 1994 to 2017 and 1981 to 2020, respectively.
- Selection of the extreme events was obtained by using Gumbel's distribution, where, 2008, 2014, 2016, and 2017 flood events were selected for this study area. A 20-year and 50-year return period is taken into consideration for the hydrological modeling and the 2017 flood event is found to have maximum streamflow and maximum inundation areas compared to the other events.
- During the sensitivity analysis of the model, Manning's roughness coefficient for river channel (n_r) and hillslope roughness coefficient (n_s) were found to be the most sensitive among the other parameters.
- Most of the inundation area from the RRI model and satellite images was located along the main river course that includes the Ratnapura town (upstream area), the Kalutara town (downstream area), and the in-between areas. However, the RRI model produced flooded areas in some of the most upstream hilly areas and its remote tributaries of the river.
- The flood extents derived from the satellite image and the RRI model match with an accuracy level of ~25 % - 30 % are deemed to be within an acceptable range for emergency evacuation and rapid flood damage assessment purposes. Although the extent was less in the satellite image, as the satellite image was not available during the peak time of the event. Therefore, inundation from the

RRI model and satellite image matches most of the part in the study area, however, some area of the upper part of the catchment has been misclassified as water pixel.

- The actual flooded area from RRI is found to be 291.97 km^2 and from satellite image is found to be 201.7 km^2 for the 2016 flood event. For the 2017 flood event, the actual flooded area from RRI is found to be 371.14 km^2 and from satellite image is found to be 297.42 km^2. Hence, the area difference was found to be 35.54 % for the 2016 flood event and 22.13 % for the 2017 flood event from the total area selected for the model.
- Sentinel-1 SAR data has great benefits and is useful in flood mapping, especially during rainy weather, as it can penetrate through clouds and no atmospheric correction is required. However, it should be noted that Sentinel-1 data involves additional pre-processing steps and that each of these steps has an impact on the output bands.

CHAPTER 8

8 RECOMMENDATIONS

From this study, the following points can be recommended:

- Satellite image data should be verified through ground-based DEM or Lidar data for flat terrain near the shoreline and river mouth cross-section data to accurately determine the extent of flooded areas.
- More accurate results can be obtained from the RRI model by using a finer resolution of DEM, however, the run time and the memory requirements increase tremendously.
- Changes in landuse play a critical in flood events and must be detected using remote sensing data for accurate flood monitoring.
- The RRI model has many advantages for pre-and post-flood disaster relief, early warning systems, rescue operations, and mitigation procedures, as it provides us with inundation information, inundation depth information, and water level.
- This study reveals that satellite imagery can be one of the most cost-effective methods to capture the flood disaster footprints, identify flood-prone areas, and understand the flooding problem in a better way. This simple procedure can be effectively used for disaster risk management, where the time factor is very critical.
- Future studies should further investigate and validate the flood inundation mapping ability of Sentinel 1A SAR using valid ground-based flood-inundation maps or other satellite data.

BIBLIOGRAPHY

Ampitiyawatta, S. (2009). Precipitation trends in the Kalu Ganga Basin in Sri Lanka. Journal of Agricultural Science, Volume 4, Number 1.

Anusha, N. (2019). Change detection and flood water mapping using Sentinel-1A Synthetic Aperture Radar images. Computational and Theoretical Nanoscience, Vol. 16, 3544–3549, 2019.

Arvinda C. S, A. V. (2016). Flood assessment using multi-temporal MODIS satellite images. Elsevier B.V, Procedia Computer Science 89 (2016) 575 – 586.

Bhagabati, S. S., & Kawasaki, A. (2017). Consideration of the rainfall-runoff-inundation (RRI) model for flood mapping in a deltaic area of Myanmar. Hydrological Research Letters, 11(3), 155–160.

Brakenridge, G. R., Nghiem, S. V., Anderson, E., & Mic, R. (2007). Orbital microwave measurement of river discharge and ice status. Water Resources Research, 43(4). https://doi.org/10.1029/2006WR005238

Brakenridge, R., & Anderson, E. (2006). MODIS-based flood detection, mapping, and measurement: the potential for operational hydrological applications. transboundary floods: Reducing Risks Through Flood Management, 1–12. https://doi.org/10.1007/1-4020-4902-1_1

Chow, V. Te, Maidment, D. R., & Mays, L. W. (1988). Applied Hydrology. McGraw-Hill, Inc.

Dabrowska-Zielinska, K., Budzynska, M., Tomaszewska, M., Bartold, M., Gatkowska, M., Malek, I., Turlej, K., & Napiorkowska, M. (2014). Monitoring wetlands ecosystems using ALOS PALSAR (L-Band, HV) supplemented by optical data: a case study of Biebrza Wetlands in northeast Poland. Remote Sensing, 6(2), 1605–1633. https://doi.org/10.3390/rs6021605

Dharmasena, G. T. (2006). Integrated Water Resources Management and Sound Information. 32nd WEDC International Conference, Colombo, Sri Lanka.

Edirisooriya, K. E. (2018). Understanding Disaster Risk and Mitigation Special Reference To Ratnapura District. Elsevier, Procedia Engineering 212 (2018) 1034–1039.

Ezzine, A., Darragi, F., Rajhi, H., & Ghatassi, A. (2018). Evaluation of Sentinel-1 data for flood mapping in the upstream of Sidi Salem dam (Northern Tunisia). Arabian Journal of Geosciences, 11(8), 1–9. https://doi.org/10.1007/s12517-018-3505-7

Fattah, K. S. (2018). Rainfall-runoff modeling for extreme flash floods in Wadi Samail, Oman. Japan: Journal of Japan Society of Civil Engineers, Ser. B1 (Hydraulic Engineering), Vol. 74, No. 5, I_691-I_696, 2018.

Frappart, F., Bourrel, L., Brodu, N., Salazar, X. R., Baup, F., Darrozes, J., & Pombosa, R. (2017). Monitoring of the Spatio-temporal dynamics of the floods in the Guayas watershed (Ecuadorian pacific coast) using global monitoring ENVISAT ASAR images and rainfall data. Water (Switzerland), 9(1). https://doi.org/10.3390/w9010012

Gomathi, M. (2018). Supervised classification for flood extent identification using Sentinel-1 radar data. 39th Asian Conference on Remote Sensing 2018.

Gupta, H. V. (1999). Status of Automatic Calibration for hydrologic models: comparison with multilevel expert calibration. Journal of Hydrologic Engineering, 4(2), 135–143.

Hanasaki et al., (2014). A quasi-real-time hydrological simulation of the Chao Phraya River using meteorological data from the Thai Meteorological Department. Hydrological Research Letters.

Hunter. (2005). An adaptive time step solution for raster-based storage cell modeling of floodplain inundation. Advances in Water Research, 28, 975–991.

Ibrahim, & Nasser. (2015). Comparison between inverse distance weighted (IDW) and kriging. International Journal of Science and Research (IJSR) ISSN (Online): 2319-7064, Volume 6 Issue 11, November 2017.

Irrigation Department, S. L. (2017). Hydrological Annual Report. Hydrology Division, Irrigation Department, Colombo 07 Sri Lanka.

Jackson, B., Mcintyre, N., Pechlivanidis, I. G., Jackson, B. M., Mcintyre, N. R., & Wheater, H. S. (2011). Catchment scale hydrological modeling: a review of model types, calibration approaches, and uncertainty analysis methods in the context of recent developments in technology and app Catchment Scale Hydrological Modelling: a Review of Model Types, Calibrate. Article in GlobalNEST International Journal, 13(3), 193–214.

Javier, J., & Alboreca, A. (2015). Use of Gumbel and Weibull functions to model extreme values of diameter distributions in forest stands. Animals of Forest Science, Springer Nature (since 2011)/EDP Science (until 2010), 2014, 71 (7), pp.741-750.10.1007/s13595-014-0369-1 01102773.

Kumar, & Tilak. (2018). Comparison of rainfall interpolation method for Delhi. Journal of Emerging Technologies and Innovative Research (JETIR), September 2018, Volume 5, Issue 9.

Kwak, Y., Park, J., & Fukami, K. (2014). Estimating floodwater from MODIS time series and SRTM DEM data. Artificial Life and Robotics, 19(1), 95–102. https://doi.org/10.1007/s10015-013-0140.

Lee, J. P. (2009). Polarimetric radar imaging from basics to applications in optical science and engineering. CRC Press: Boca Raton, FL, USA, Volume 142.

Liang, J. &. (2019). A local thresholding approach to flood water delineation using Sentinel-1 SAR imagery. ISPRS Journal of Photogrammetry and Remote Sensing,

Matgen, P., Hostache, R., Schumann, G., Pfister, L. & Hoffmann, L. (2011). Towards an automated SAR-based flood monitoring system. Physics and Chemistry of the

Earth, 36(7–8), 241–252. https://doi.org/10.1016/j.pce.2010.12.009

Modeling, F., Sensing, R., & Images, S. (2010). Application of remote sensing and GIS for flood risk analysis : a case study at Kalu Ganga River, Sri Lanka. International Archives of the Photogrammetry, Remote Sensing and Spatial Information Science, XXXVIII(8), 110–115.

Moriasi, J. G. (2007). Model evaluation guidelines for systematic quantification of accuracy in watershed simulations. 2007 American Society of Agricultural and Biological Engineers ISSN 0001−2351.

Nandalal, K. D. W. (2009). Use of a hydrodynamic model to forecast floods of Kalu River in Sri Lanka. Journal of Flood Risk Management, 2(3), 151–158. https://doi.org/10.1111/j.1753-318X.2009.01032.x

Nastiti, K. D., Kim, Y., Jung, K., & An, H. (2015). The application of Rainfall-Runoff-Inundation (RRI) model for inundation case in upper Citarum Watershed, West Java-Indonesia. Procedia Engineering, 125, 166–172. https://doi.org/10.1016/j.proeng.2015.11.024

Priority Index Sri Lanka Floods. (2017, May). Retrieved from Priority Index Sri Lanka Floods: Https://Data.Humdata.Org/Dataset/Priority-Index-Sri-Lanka-Floods-May-2017

Ramsy, M. (2019). Development of Water and Energy Budget-based Rainfall-Runoff-Inundation model and its verification in the Kalu and Mundeni River Basins, Sri Lanka. Japan: Journal Of Hydrology 579 (2019) 124163.

Rawls, W. E. (1992). Infiltration and soil water movement. Handbook Of Hydrology. New York: Mcgrow-Hill Inc., 5.1–5.51.

Samarasinghe, S. (2010). Application of remote sensing and GIS for flood risk analysis: a case study at Kalu Ganga River, Sri Lanka. Japan: International Archives of the Photogrammetry, Remote Sensing and Spatial Information Science, Volume XXXVIII, Part 8, Kyoto Japan 2010.

Sayama. (2012). Rainfall-Runoff–Inundation analysis of the 2010 Pakistan flood in the Kabul River. Japan: Hydrological Sciences Journal, International Centre for Water Hazard and Risk Management, Public Works Research Institute.

Sayama, T., Myo Lin, N., Fukami, K., Tanaka, S., & Takeuchi, K. (2011). Storm surge inundation simulation of cyclone Nargis with a Rainfall-Runoff-Inundation model. Journal of Japan Society of Civil Engineers, Ser. B1 (Hydraulic Engineering), 67(4), I_529-I_534. https://doi.org/10.2208/jscejhe.67.i_529

Sayama, T., (2015). An emergency response-type rainfall-runoff-inundation simulation for 2011 Thailand floods. Japan: Journal of Flood Risk Management.

Schaffenberg, W., & Fleming, M. (2013). Hydrologic modeling system HEC-HMS, user manual: version 4.0. US Army Corps of Engineers, Hydrologic Engineering Center HEC, 609.

Schlaffer, S., Chini, M., Giustarini, L., & Matgen, P. (2017). Probabilistic mapping of flood-induced backscatter changes in SAR time series. International Journal of Applied Earth Observation and Geoinformation, 56, 77–87. https://doi.org/10.1016/j.jag.2016.12.003

Senel, G., Eroglu, M., Balcik, F. B., Goksel, C., & Cand, P. D. (2020). Analyzing flood-affected regions in Meriç River using Sentinel-1 and Sentinel-2 data. 1(June), 710–716.

Subramanya, K. (2013). Engineering Hydrology. New Delhi: Mcgraw Hill Education (India) Pvt Ltd.

Tarpanelli, L. B. (2015). River discharge estimation through MODIS data. Remote Sensing for Agriculture, Ecosystems, and Hydrology XIII.

Tavus, B. (2018). Considerations on the use of Sentinel-1 data in flood mapping in urban areas: Ankara (Turkey) 2018 floods. International Archives of the Photogrammetry, Remote Sensing and Spatial Information Sciences, Volume XLII-5, 2018.

Tavus, B. (2019). Flood mapping using Sentinel-1 SAR data: a case study of Ordu 8 August 2018 flood. International Journal of Environment and Geoinformatics.

Tekleab, S., Uhlenbrook, S., Mohamed, Y., & Savenije, H. H. (2011). Water balance modeling of upper Blue Nile catchments using a top-down approach. Hydrol. Earth Syst. Sci., 15, 2179-2193. Doi:10.5194/Hess-15-2179-2011

Thomas, H. A. (1981). Improved methods for national Tvater assessment. Harvard University, Harvard Water Resources Group. Cambridge, MA 02138: Water Resources Contract: WR15249270.

Try, S., Tanaka, S., Tanaka, K., Sayama, T., Oeurng, C., Uk, S., Takara, K., Hu, M., & Han, D. (2020). Comparison of gridded precipitation datasets for rainfall-runoff and inundation modeling in the Mekong River Basin. PLoS ONE, 15(1), 1–13. https://doi.org/10.1371/journal.pone.0226814

Uyanıka, G. K. (2013). A study on multiple linear regression analysis. Procedia: Social and Behavioral Sciences, Volume 106, 10 December 2013, Pages 234-240.

Vogel, R. M., & Sankarasubramanian, A. (2003). Validation of a watershed model without calibration. Water Resources Research, 39(10), P. 1292. Doi:10.1029/2002WR001940

Wheater, H., Sorooshian, S., & Sharma, K. D. (2008). Hydrological modeling in arid and semi-arid areas. Hydrological Modelling in Arid and Semi-Arid Areas.

Yulianto, F., Sofan, P., Zubaidah, A., Sukowati, K. A. D., Pasaribu, J. M., & Khomarudin, M. R. (2015). Detecting areas affected by flood using multi-temporal ALOS PALSAR remotely sensed data in Karawang, West Java, Indonesia. Natural Hazards, 77(2), 959–985. https://doi.org/10.1007/s11069-015-1633-x

Yoshimoto, A. (2017). Applications of satellite-based rainfall estimates in flood inundation modeling- Mundeni Aru River Basin, Sri Lanka. International Water Management Institute (IWMI), Battaramulla 10120, Sri Lanka.

Zeinivand. (2015). Comparison of interpolation methods for precipitation fields using the physically based and spatially distributed model of river runoff for Gharesou Basin, Iran. ISSN 1068-3739, Russian Meteorology and Hydrology, 2015, Vol. 40, No. 7, Pp. 480–488. Ó Allerton Press, Inc., 2015.

ANNEXURE 1

DATA CHECKING FOR MISSING VALUES

Table A1- 1: General arrangement of rainfall data in chronological order in excel

Date	Ratnapura Station	Galatura Estate Station	USK Valley Station	Halwatura Station
01-01-2013	4	0	0	0
02-01-2013	10	0	0	0
03-01-2013		12	28	0
04-01-2013		10	0	22
05-01-2013		0	0	0
06-01-2013		1	0	0
07-01-2013		30	15	0
08-01-2013		0	15	65
09-01-2013	2	0	30	0
10-01-2013	5	7	39	0
11-01-2013	20	0.5	29	58
12-01-2013	60	0	0	0
13-01-2013	12	0	56	0
14-01-2013	2	0	46	0
15-01-2013		0	22	0
16-01-2013		0	0	0
17-01-2013	15	0	0	0
18-01-2013	28	0	7	0
19-01-2013	35	0	15	0
20-01-2013	32	0	107	0
21-01-2013	27	0	0	0
22-01-2013	32	0	0	0

ANNEXURE 2

CALIBRATION OF RRI MODEL

Table A2- 1: Calibration of 2008 flood event

Year	Month	Day	Date	Flow Observed (m^3/s)	Flow Observed (inches/day)	Stream Flow Simulated (m^3/s)	Stream Flow Simulated (inches/day)	$(SF_{Obs}-SF_{Sim})^2$	$(SF_{Obs}-SF_{Mean})^2$
2008	5	22	2008-05-22	167.67	0.374	162	0.361	0.000	0.140
2008	5	23	2008-05-23	87.65	0.195	63	0.140	0.003	0.038
2008	5	24	2008-05-24	82.95	0.185	72	0.160	0.001	0.034
2008	5	25	2008-05-25	85.29	0.190	71	0.158	0.001	0.036
2008	5	26	2008-05-26	158.88	0.354	105	0.234	0.014	0.125
2008	5	27	2008-05-27	244.51	0.545	246	0.548	0.000	0.297
2008	5	28	2008-05-28	392.19	0.874	441	0.983	0.012	0.764
2008	5	29	2008-05-29	505.39	1.127	895	1.995	0.754	1.269
2008	5	30	2008-05-30	878.39	1.958	1202	2.679	0.520	3.834
2008	5	31	2008-05-31	1233.60	2.750	1310	2.920	0.029	7.561
2008	6	1	2008-06-01	1355.63	3.022	1311	2.922	0.010	9.131
2008	6	2	2008-06-02	1232.56	2.747	1084	2.416	0.110	7.549

Year	Month	Day	Date	Flow Observed (m^3/s)	Flow Observed (inches/day)	Stream Flow Simulated (m^3/s)	Stream Flow Simulated (inches/day)	$(SF_{Obs}-SF_{Sim})^2$	$(SF_{Obs}-SF_{Mean})^2$
2008	6	3	2008-06-03	1085.06	2.419	774	1.725	0.481	5.850
2008	6	4	2008-06-04	911.04	2.031	480	1.070	0.923	4.124
2008	6	5	2008-06-05	675.33	1.505	527	1.175	0.109	2.266
2008	6	6	2008-06-06	424.45	0.946	691	1.540	0.353	0.895
2008	6	7	2008-06-07	280.09	0.624	574	1.279	0.429	0.390
2008	6	8	2008-06-08	173.06	0.386	172	0.383	0.000	0.149
2008	6	9	2008-06-09	112.46	0.251	88	0.196	0.003	0.063
	Total							**3.753**	**44.516**

Table A2- 2: Calibration of 2014 flood event

Year	Month	Day	Date	Flow Observed (m^3/s)	Flow Observed (inches/day)	Stream Flow Simulated (m^3/s)	Stream Flow Simulated (inches/day)	$(SF_{Obs}-SF_{Sim})^2$	$(SF_{Obs}-SF_{Mean})^2$
2014	5	28	2014-05-28	85.65	0.191	178.63	0.398	0.043	0.036
2014	5	29	2014-05-29	250.04	0.557	62.74	0.140	0.174	0.311
2014	5	30	2014-05-30	570.60	1.272	170.82	0.381	0.794	1.618
2014	5	31	2014-05-31	747.03	1.665	410.69	0.915	0.562	2.773
2014	6	1	2014-06-01	949.09	2.116	998.03	2.225	0.012	4.476
2014	6	2	2014-06-02	1003.48	2.237	1137.56	2.536	0.089	5.003

Year	Month	Day	Date	Flow Observed (m^3/s)	Flow Observed (inches/day)	Stream Flow Simulated (m^3/s)	Stream Flow Simulated (inches/day)	$(SF_{Obs}-SF_{Sim})^2$	$(SF_{Obs}-SF_{Mean})^2$
2014	6	3	2014-06-03	906.04	2.020	1020.56	2.275	0.065	4.079
2014	6	4	2014-06-04	788.22	1.757	693.00	1.545	0.045	3.087
2014	6	5	2014-06-05	499.37	1.113	592.73	1.321	0.043	1.239
2014	6	6	2014-06-06	257.89	0.575	455.91	1.016	0.195	0.330
2014	6	7	2014-06-07	192.60	0.429	227.28	0.507	0.006	0.184
2014	6	8	2014-06-08	125.40	0.280	255.14	0.569	0.084	0.078
2014	6	9	2014-06-09	151.11	0.337	253.48	0.565	0.052	0.113
2014	6	10	2014-06-10	334.53	0.746	437.93	0.976	0.053	0.556
2014	6	11	2014-06-11	401.32	0.895	528.45	1.178	0.080	0.800
		Total						**2.298**	**24.685**

VALIDATION OF RRI MODEL

Table A2- 3: Validation of 2016 flood event

Year	Month	Day	Date	Flow Observed (m^3/s)	Flow Observed (inches/day)	Stream Flow Simulated (m^3/s)	Stream Flow Simulated (inches/day)	$(SF_{Obs}-SF_{Sim})^2$	$(SF_{Obs}-SF_{Mean})^2$
2016	5	8	2016-05-08	213.925	0.477	154.7	0.345	0.017	0.227
2016	5	9	2016-05-09	65.948	0.147	189.84	0.423	0.076	0.022
2016	5	10	2016-05-10	57.318	0.128	188.11	0.419	0.085	0.016
2016	5	11	2016-05-11	171.198	0.382	228.01	0.508	0.016	0.146
2016	5	12	2016-05-12	195.813	0.436	191.3	0.426	0.000	0.191
2016	5	13	2016-05-13	211.59	0.472	624.61	1.392	0.848	0.222
2016	5	14	2016-05-14	307.29	0.685	859.52	1.916	1.515	0.469
2016	5	15	2016-05-15	523.14	1.166	975.95	2.175	1.019	1.360
2016	5	16	2016-05-16	895.19	1.995	996.77	2.222	0.051	3.982
2016	5	17	2016-05-17	681.415	1.519	969.37	2.161	0.412	2.307
2016	5	18	2016-05-18	622.94	1.389	901.39	2.009	0.385	1.928
2016	5	19	2016-05-19	486.685	1.085	809.61	1.805	0.518	1.177
2016	5	20	2016-05-20	366.688	0.817	623.15	1.389	0.327	0.668
2016	5	21	2016-05-21	253.355	0.565	324.51	0.723	0.025	0.319
2016	5	22	2016-05-22	218.183	0.486	227.73	0.508	0.000	0.237
2016	5	23	2016-05-23	192.385	0.429	253.37	0.565	0.018	0.184
2016	5	24	2016-05-24	186.27	0.415	246.06	0.548	0.018	0.172
		Total						**5.332**	**13.627**

Table A2- 4: Validation of 2017 flood event

Year	Month	Day	Date	Flow Observed (m^3/s)	Flow Observed (inches/day)	Stream Flow Simulated (m^3/s)	Stream Flow Simulated (inches/day)	$(SF_{Obs}-SF_{Sim})^2$	$(SF_{Obs}-SF_{Mean})^2$
2017	5	9	2017-05-09	75.05	0.167	244.56	0.545	0.143	0.028
2017	5	10	2017-05-10	79.13	0.176	66.05	0.147	0.001	0.031
2017	5	11	2017-05-11	85.26	0.190	82.43	0.184	0.000	0.036
2017	5	12	2017-05-12	76.73	0.171	64.22	0.143	0.001	0.029
2017	5	13	2017-05-13	86.37	0.193	61.28	0.137	0.003	0.037
2017	5	14	2017-05-14	198.31	0.442	69.12	0.154	0.083	0.195
2017	5	15	2017-05-15	188.68	0.421	146.63	0.327	0.009	0.177
2017	5	16	2017-05-16	89.46	0.199	509.36	1.135	0.876	0.040
2017	5	17	2017-05-17	106.03	0.236	506.15	1.128	0.795	0.056
2017	5	18	2017-05-18	156.67	0.349	274.78	0.613	0.069	0.122
2017	5	19	2017-05-19	75.54	0.168	253.20	0.564	0.157	0.028
2017	5	20	2017-05-20	61.04	0.136	330.34	0.736	0.360	0.019
2017	5	21	2017-05-21	59.99	0.134	225.78	0.503	0.137	0.018
2017	5	22	2017-05-22	58.44	0.130	184.97	0.412	0.080	0.017
2017	5	23	2017-05-23	103.99	0.232	202.26	0.451	0.048	0.054
2017	5	24	2017-05-24	365.76	0.815	354.45	0.790	0.001	0.665
2017	5	25	2017-05-25	1096.13	2.443	848.94	1.892	0.304	5.970
2017	5	26	2017-05-26	2005.57	4.471	1658.98	3.698	0.597	19.986
2017	5	27	2017-05-27	2316.37	5.163	2398.28	5.346	0.033	26.660
2017	5	28	2017-05-28	2129.33	4.746	2208.44	4.923	0.031	22.529

Year	Month	Day	Date	Flow Observed (m^3/s)	Flow Observed (inches/day)	Stream Flow Simulated (m^3/s)	Stream Flow Simulated (inches/day)	$(SF_{Obs}-SF_{Sim})^2$	$(SF_{Obs}-SF_{Mean})^2$
2017	5	29	2017-05-29	1797.83	4.008	1717.90	3.829	0.032	16.060
2017	5	30	2017-05-30	1459.02	3.252	1656.97	3.694	0.195	10.577
2017	5	31	2017-05-31	533.82	1.190	1184.26	2.640	2.102	1.416
2017	6	1	2017-06-01	427.54	0.953	800.86	1.785	0.692	0.908
2017	6	2	2017-06-02	319.45	0.712	544.17	1.213	0.251	0.507
2017	6	3	2017-06-03	225.01	0.502	643.72	1.435	0.871	0.252
2017	6	4	2017-06-04	174.54	0.389	569.25	1.269	0.774	0.151
2017	6	5	2017-06-05	155.71	0.347	333.61	0.744	0.157	0.120
2017	6	6	2017-06-06	133.84	0.298	230.64	0.514	0.047	0.089
2017	6	7	2017-06-07	163.15	0.364	219.82	0.490	0.016	0.132
2017	6	8	2017-06-08	130.81	0.292	229.49	0.512	0.048	0.085
		Total						**8.912**	**106.995**